UNIVERSITÉ DU LUXEMBOURG

PhD-FSTC-2019-26
The Faculty of Sciences, Technology and Communication

# DISSERTATION

Defence held on 29/04/2019 in Esch-sur-Alzette

to obtain the degree of

## DOCTEUR DE L'UNIVERSITÉ DU LUXEMBOURG

## EN PHYSIQUE

by

Carlos ESCORIHUELA SAYALERO
Born on 2nd of February 1989 in Barcelona (Spain)

# SECOND-PRINCIPLES METHODS FOR LARGE-SCALE SIMULATIONS OF REALISTIC FUNCTIONAL OXIDES

## Dissertation defence committee

Dr Jorge Íñiguez González, dissertation supervisor
*Professor, Université du Luxembourg*

Dr Thomas Schmidt, Chairman
*Associate Professor, Université du Luxembourg*

Dr Jens Kreisel, Vice Chairman
*Vice-Rector for Research*
*Professor, Université du Luxembourg*

Dr Anna Grünebohm
*Doctor, Universität Duisburg-Essen*

Dr María José Calderón
*Doctor, Instituto de Ciencia de Materiales de Madrid*

# Acknowledgements

I have chosen to write my acknowledgements in my language, Catalan.

Escriure una tesi doctoral és un esdeveniment important en la vida acadèmica. Com a experiència personal, estic extremadament satisfet. No només pel que he pogut aprendre de mi mateix i de la meva carrera com a científic en el procés de desenvolupament del projecte, i per l'àrdua (però gratificant) tasca d'escriure el Manuscrit. Tot i que es dóna per suposat, vull remarcar que és cert: escriure una tesi, es gaudeix. Però he de dir que el camí hauria sigut infinitament més difícil sense les persones que han fet possible que jo, en aquest moment, finalitzi l'escriptura d'aquest document.

Si hagués de marcar un origen en aquest camí, diria que l'empenta inicial la vaig rebre de l'equip escolar de l'escola on vaig créixer, a la meva ciutat, Olot. Mai t'estaré prou agraït per fer-me mirar el diccionari, David. Per ensenyar-me el que és l'amor i la paciència, Rosa. Per donar-me canya i fer-me creure en mi mateix, Coral. Per reptar-me, Marc.

Gràcies a ells, vaig poder conèixer els que serien els meus amics, la gent amb qui m'identifico a nivell familiar. Ells m'han donat aire cada cop que ens hem vist, m'han aportat el que he necessitat. Les tardes a la Fageda amb l'Adrià. Els experiments i muntatges fantàstics d'en Pau. Les bogeries músico-culinàries d'en Xicu. Ferran, Pau, Andreu, Joel, Albert... la llista és tan llarga! Gràcies per l'esforç de cadascuna de les persones del Bones Festes!, que han mogut cel i terra per trobar un moment per mi quan tornava a casa. Gràcies per donar-me el sopar de comiat més galàctic i inoblidable de la meva vida.

Vull agraïr també l'Oscar per ensenyar-me a passar-ho bé amb la guitarra. Perquè així vaig conèixer Zigot, el grup de rock experimental que ha sacrificat quatre anys de progrés per mantenir a un guitarrista en plantilla que només podia composar a distància. La paciència d'en Jordi i en Titi, i el seu amor, els seus assajos per Skype perquè tingués bona música per escriure el manuscrit, són de les coses més boniques que he viscut mai. Gràcies. Podríem dir, suposo, que això és el que passa quan poses l'Escalopendra per escrit :).

No perdo de vista als qui aguanten les meves reflexions sense sentit, i que me les tornen arreglades. A l'Alba, de qui sempre admiraré la seva capacitat de fer-me connectar i de treure el millor de mi. A Pablo, el individuo que no te puedes acabar nunca, que siempre aporta un ángulo humano inesperado, a quién conocí de la manera más improbable, y al que es más improbable que quiera tener lejos. A la Judit i a la Carme. A l'Agnès i el cel que porta al cor. A en Dani, per no rendir-se mai i ensenyar-me què vol dir estar convençut del què es vol. A en David i en Josep: domo arigatou.

Quan vaig marxar de casa vaig aprendre que marxar no és tant senzill com un s'imagina. Però és més senzill si en Gerard i l'Àurea (i l'Ayla!) són a una trucada de veu de distància. Us agraeixo

com m'heu cuidat tant en la distància a casa vostra! Al final del trajecte, només puc pensar en compartir un cop més una 13 amb vosaltres.

Naturalment, en l'àmbit professional he tingut recolzament que m'ha permès avançar en el meu projecte i sense el qual aquesta tesi no s'hauria pogut realitzar.

Quiero empezar por agradecer, de la manera más sincera, la infinita paciencia, la comprensión, la firmeza, los conocimientos y la experiencia de escribir y defender mi tesis a mi director, Jorge Íñiguez. Él ha sido mi mentor durante estos años, ha sido quién me ofreció la oportunidad (junto a Oswaldo Diéguez) de conocer qué es la ciencia, y quién ha creído que yo podía escribir éste texto. Gracias de corazón por invitarme a esta aventura. Jamás olvidaré el café en la Facultat d'Enginyeria.

I am also thankful of having collaborated with Jacek C. Wojdeł. He was the one who wrote the fantastic SPLD code and who helped me in my first steps in this endeavour. I'm really grateful of having had the opportunity of working with you!

Also, I want to thank the people with which I have collaborated scientifically these years. I want to thank Riccardo Rurali, Pol Torres, Miquel Royo, Juan Antonio Seijas and Hugo Aramberri for taking me with them in their thermodynamical adventures. Eskerrik asko, Hugo! Espero que sigamos colaborando en el futuro, eres una auténtica bocanada de aire fresco y me alegro un montón de que te hayas unido al equipo; ojalá pudiera disfrutar de tu presencia más tiempo.

Gracias también por la fantástica interacción científica mantenida con Pablo García y Javier Junquera, co-desarrolladores del proyecto SCALE-UP. I'd like to thank as well Laurent Bellaiche, Massimiliano Stengel and Andrea Schiaffino for the insightful discussions held. Finally, thanks to Nicholas Bristowe for his inspiring scientific mindset and his unique sense of humor.

Durant els primers anys vaig estar fent la meva carrera científica a l'Institut de Ciència de Materials de Barcelona. D'aquell temps, agraeixo a la Pietat la seva paciència i les converses hilarants, la companyia del meravellós Blai Casals. Agraeixo al Ferran, la Laia, la Maria, la Birra dels Dijous, i en Juan Carlos les fantàstiques estones que hem passat junts, però sobretot, a la Júlia, pel seu amor, per la seva brillantesa i fortalesa, per inspirar-me més vegades de les que es pensa. Us trobo a faltar!

Gracias a los Muñones por darle una salida a mi dolor y frustración, por acompañarme y acogerme. A David y Bojana, Tato, el Señor Gillmanícias y sus pogos, y a Micha. Y por supuesto, gracias infinitas, Harry. Tu forma de ser encendió en mí la llama competitiva, me enseñó a esforzarme hasta puntos absurdos. A sentirme acompañado, dejar la soledad a un lado. Y gracias a Orhy, porque sin tí jamás sabría qué es castear.

Adapting to the new location was not as easy as it looked. I guess it's hard when you move for the first time outside your home. However, the team I joined made everything easier. I want to thank Alex, because it wasn't easy, but you gave me a rope to hold by being who you are. I want to thank Shankari for the hours of conversation. Mauro, I'm sorry, but Porto can't play like Barça, even in the PS4. I want to thank Cosme, he is the real reason I could make it here (no jokes, your patience, warmth and listening skills are gold - and the fuet!). No m'oblido de tu, Àlvar. Em fascina el què fas i com ets. Thank you, Corinne and Alexis, for all the help, for the mood, for the jokes, for the laughs. I would like to express my deep gratitude as well to Mael, for I truly like how you are, how you interact with me, and I admire the depth to which your mind can go. Thanks for

the patience with me, Emmanuel, and for joining me on stage. That was unexpected. Charlotte, Mads, Javier; and of course, the unique, brilliant, pure soul of Chen Peng.

I'm immensely grateful of meeting Constance in Luxembourg. For supporting me. For sticking a rope in my belt and asking me to climb. For inspiring me, for kicking my ass and making me use my head. You've been light pushing me into evolution. Merci beaucoup.

Finalment, vull agraïr a la família el suport i la força rebuda. A mi padre, por acer aquello que creía imposible, por ser un pilar y no fallar **jamás**. A mi madre, por su sabiduría, el amor que me da, su apoyo. A mi hermana, con la que nos decimos las cosas de la peor manera posible, y a la que quiero con locura. A Laly y Agus, por iluminarme con su luz. A mi tío José, por querer enseñarme a programar cuando era un crío, por saber estimular mi mente. A mi abuela, que ha tenido el valor de querer subirse a un avión para verme defender. A Jose por sus visitas, y a mis geniales primas y sus aciertos en el calendario. A la misteriosa Andrea. A l'Elvira i l'Albert, per acollir-me com un fill, per ser les meravelloses persones que són.

Finalment, vull donar les gràcies la Sílvia. L'aventura en què ens hem embarcat no ha sigut senzilla. La seguretat i el recolzament que m'has aportat quan ho he necessitat no tenen preu. L'amor i la bondat amb la que vius és única. L'empenta quan les coses no van tan bé, inspiradora. M'has ajudat a poder arribar aquí com ningú ho podria haver fet. Aquesta tesi també és teva.

Per això, i per tot allò que no he dit: gràcies a tots. Rebeu l'abraçada més forta, la més sentida, la més profunda. Us estimo.

# Contents

# Chapter 1

# Introduction

This Thesis develops itself within the Materials Science domain. I present in this Chapter an overview of the field, focusing primarily on the context that has motivated my research. In Section 1.1 I overview the family of materials known as Perovskites. The set of compounds belonging to this cathegory represent a portion of Materials Science field that has extreme relevence, not only in the scientific scope but also for device engineering due of the extraordinary fundamental (and functionalizable) properties they can exhibit. In Section 1.2 I introduce the computational approach to this field of study. It is precisely here, within the theoretical and simulation perspective, where the core of this Thesis is established. Finally, in Section 1.3 I describe and discuss the main objectives of my project and the general structure of this Manuscript.

## 1.1 $AB\mathbf{O}_3$ perovskite oxides

As described in C. Kittel's book "*Introduction to solid state physics*"[1], a perovskite structure is a structure that is equivalent to that of the prototype perovskite, $CaTiO_3$. Generically, perovskites have the chemical formula $ABO_3$. As with the structure of calcium titanate, $A$ cations are located at the vertices of a cube, the $B$ cation occupies the center of the structure and is caged by a regular octahedra of oxygens, which are positioned at the center of the faces of the cube. The standard cubic structure of perovskites is represented in panel (a) of Figure 1.1.

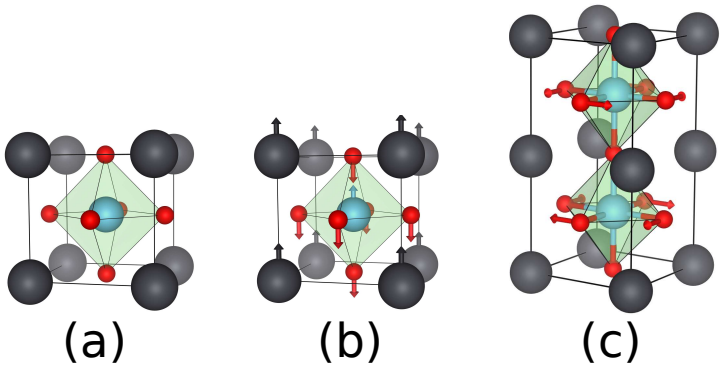


**Figure 1.1: Sketch of the 5-atom unit cell of the Perovskite structure**. **(a)** Structure of the so-called cubic phase (with associated space group $Pm\bar{3}m$). For a generic perovskite of chemical formula $ABO_3$, the $A$ cations are shown in black, the $B$ cation is represented by the blue atom in the center of the cube and the oxygens are sketched in red. The oxygens form an octahedra, which has been highlighted in pale green. **(b)** Ferroelectric distortion of the cubic cell. **(c)** Antiferrodistortive distortion of the cubic cell.

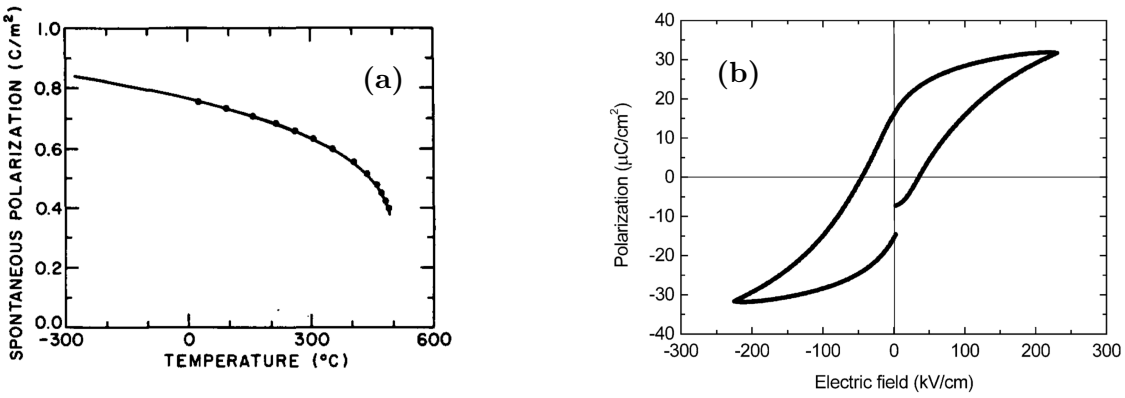


**Figure 1.2: Experimental evidence of ferroelectricity from literature for $PbTiO_3$ and $PbZr_xTi_{1-x}O_3$.** **(a)** Experimental study of the structural phase transition of $PbTiO_3$, characterized by the appearance of a spontaneous polarization as order parameter (from Ref. [2]). **(b)** P-E hysteresis loop of a $PbZr_{0.53}Ti_{0.47}O_3$ thick film (from Ref. [3]), showing the switcheable character of the polarization by applying an external electric field.

Perovskite materials can display a variety of different properties. Some of these can be understood from a structural perspective. Within this scope, the deformations of the cubic cell presented in Figure 1.1 are linked to the rise of highly functionalizable properties such as ferroelectricity or piezoelectricity, which will be defined in the following sections. Perovskites nonetheless can exhibit a variety of other properties of high interest - ferromagnetism, multiferroic couplings, electrocaloric or magnetooptic effects are but an example of the richness of applicability of these compounds. These latter properties, however very relevant, are not discussed in this text.

The emphasis in this Thesis is set around two perovskite compounds: lead titanate ($PbTiO_3$), a ferroelectric material, and strontium titanate ($SrTiO_3$), well known for being a paraelectric material with ferroelastic properties.

### 1.1.1 Ferroelectricity, ferroelasticity and piezoelectricity

**Ferroelectricity** is the property of materials that display a spontaneous polarization (panel (a) of Figure 1.2), which is zero above $T_c$ (paraelectric phase) and non-zero for $T < T_c$. The polarization in perovskites is originated by a polar distortion of the cell, leading to a ferroelectric phase as depicted in panel (b) of Figure 1.1. In a ferroelectric material the polarization can be reversed by the application of an external electric field, typically exhibiting a hysteresis loop (see panel (b) in Figure 1.2). The display of the spontaneous polarization is accompanied by an increase of the dielectric susceptibility $\chi_{ij}$, which is defined as

$$\chi_{ij} = \frac{\partial P_i}{\partial E_j} = -\frac{\partial F}{\partial E_i \partial E_j}, \tag{1.1.1}$$

where $\mathbf{P}$ is the electric polarization, $\mathbf{E}$ is the external electric field, $F$ is the free energy and $i, j$ label the cartesian directions of space. The larger the dielectric susceptibility, the larger the polarization induced by the electric field, since $\mathbf{P} = \boldsymbol{\chi}\epsilon_0\mathbf{E} + \mathbf{P}_0$, where $\mathbf{P}_0$ is the spontaneous part of the polarization.

Similarly to ferroelectricity, **ferroelasticity** is the property of materials that exhibit a spontaneous change in strain $\boldsymbol{\eta}$ in absence of external stress $\boldsymbol{\sigma}$ or external applied electric field. For

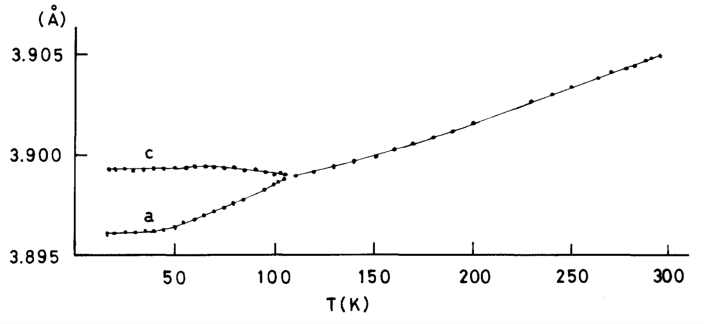


**Figure 1.3:** Change of the strain as a function of temperature in $SrTiO_3$. This result is extracted from Ref. [4].

example, the ground state of $SrTiO_3$ consists in the display of an oxygen octahedra rotation (depicted in panel (c) of Figure 1.1). The oxygen octahedra rotation is related to an elongation of the crystal unit cell along one axis. This change in strain, evidenced experimentally in Figure 1.3 as a function of temperature, is the signature of a ferroelastic material.

A material is **piezoelectric** if an applied stress leads to a change in the polarization of the material. Also, in a piezoelectric material an applied external electric field implies a strain variation (known as the reverse piezoelectric effect). The change in strain is linear with the electric field, in contrast with the electrostictive effect, in which the relationship is quadratic [5]. All ferroelectric materials are piezoelectric, although the opposite statement is not true. The key quantity in a piezoelectric material is its piezoelectric coefficient $d_{ik}$, defined as

$$d_{ik} = \left(\frac{\partial \eta_k}{\partial E_i}\right)\Big|_{\boldsymbol{\sigma}}, \tag{1.1.2}$$

where $i, j = 1, 2, 3$ are the cartesian directions, $k = 1, .., 6$ is the so-called Voigt notation and $\mathbf{E}$ is the electric field. In the Voigt notation, $(1, 2, 3, 4, 5, 6) \leftrightarrow (xx, yy, zz, yz, zx, xy)$. The larger the piezoelectric coefficient, the larger the response of the material to an applied stress or to an applied external electric field.

### 1.1.2 Structural phase transitions

Ferroelectricity and ferroelasticity are characterized by the spontaneous display of a physical property when undergoing a structural phase transition. This type of phase transitions are characterized by a distortion of the cell under certain thermodynamic conditions. It is customary to understand and study them by defining an adequate *order parameter*. This is usually a quantity that is zero above the transition point, and attains a certain value when the transition occurs. As an example, in proper ferroelectric phase transitions the order parameter is the electric polarization of a material (see panel (a) in Figure 1.2).

The analysis of the order parameter in structural phase transitions is critical to understand the

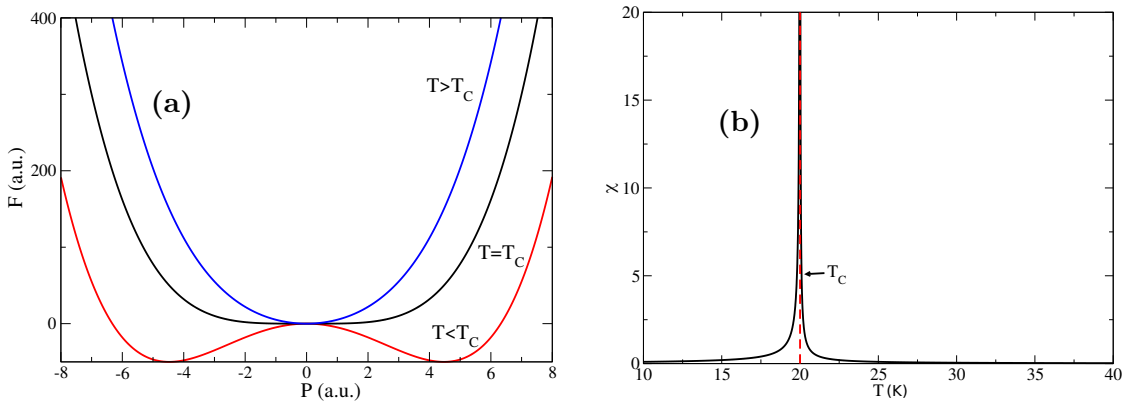


**Figure 1.4: Analysis of a second order phase transition as described by the Landau theory. (a)** Different free energy curves for temperatures above, below and $T_0$ as described by the Landau theory. **(b)** Value of the dielectric susceptibility as a function of the temperature.

character of the transition, and can be studied using the Landau theory of phase transitions. In this theory the free energy is expanded as a function of the order parameter, while the temperature is included as a parameter of the coefficients of the expansion. For a ferroelectric material $F(P;T) = F(-P;T)$, and *second-order* phase transition theory can be written as

$$F(P;T) = -\frac{1}{2}\gamma(T_c - T)P^2 + \frac{1}{4}A_4P^4 - EP, \tag{1.1.3}$$

where $T_c$ is the transition temperature and $E$ the external electric field. The minima of the free energy for a given $T$ correspond to the equillibrium phases of the material.

In the panels of the Figure 1.4 I show how this expression of the free energy represents the phase transition. As displayed, the parametrization through the temperature allows for the functional of the free energy to evolve. In particular, as the temperature crosses the $T_c$ the free energy develops a double-well energy potential (panel (a) of Figure 1.4), indicating the occurrence at a non-zero polarization.

The transition temperature in a second-order phase transition is characterized by a divergence of the dielectric suspceptibility, as seen in panel (b) of Figure 1.4. From Eq. 1.1.1 follows that this quantity is related to the inverse of the curvature of the potential energy surface. Hence, large dielectric susceptibilities indicate flat energy landscapes in which the material can undergo structural distortions without high energy costs.

### 1.1.3 Main structural distortions

The properties discussed in the previous section have their origin in the atomic structure of the material. When undergoing a structural phase transition, the atomic structure is *distorted* giving rise to the different effects described. In this work I focus on two types of occurring distortions in the perovskite structure: the antiferrodistortive (AFD) and the ferroelectric (FE) distortions. As discussed in [6], the distortions occurring in $ABO_3$ perovskites can be understood through the Goldschmidt tolerance factor [7]. It is defined as

$$t = \frac{R_A + R_O}{\sqrt{2}(R_B + R_O)}, \tag{1.1.4}$$

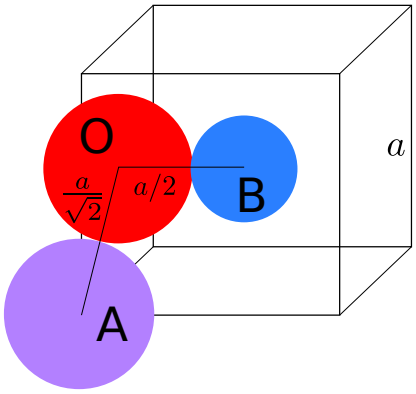


**Figure 1.5:** Depiction of the cubic perovskite structure, where the atoms have been depicted according to their ionic radii. The side of the cube is of length $a$.

where $R_i$ is the nominal ionic radii of the atom type $i$. In the ideal cubic perovskite structure the distance $\mathrm{A}-\mathrm{O}$ is $\sqrt{2}$ times bigger than the distance $\mathrm{B}-\mathrm{O}$ (see Figure 1.5). If one considers the ionic radii of the atoms, the structure is such that the atoms are "in contact". Hence, the distances between the atoms coincide with the sum of their ionic radii. The tolerance factor is a ratio of these distances, properly weighted by the factor $\sqrt{2}$. If $t = 1$ the distances $\mathrm{A}-\mathrm{O}$ and $\mathrm{B}-\mathrm{O}$ are compensated, and so the structure would tend to be stable in the cubic phase.

For $t < 1$, there is more space between $A$ and O than between $B$ and O. The perovskite cell will tend then to compensate the empty space by adjusting the structure, usually leading to a rotation of the regular oxygen octahedron. An example of this is calcium titanate, for which the ground state involves three rotations. Rotations are the type of distortions known as antiferrodistortive (AFD), in which the oxygen octahedra is rotated along one or more axis, either in phase or in anti-phase fashion. Panel (c) of Figure 1.1 is a sketch of an anti-phase rotation occurring along one axis as an example. Note that the atoms that are involved in the rotation are connected to the adjacent cells, and so the rotation of the adjacent cells in the plane perpendicular to that of the rotation axis occurs necessarily in anti-phase. Additionally, in some cases $t < 1$ leads to a displacement of the A cations towards the oxygens, as is the case of lead titanate, which develops a polarization parallel to the [001] crystallographic axis in its ground state.

Contrarily, the tolerance factor can be $t > 1$. This means that the distance $B - \mathrm{O}$ may be optimized, since the $B$ cation will have affinity to move towards the oxygens and the space to do so. The type of distortion that then occurs is the ferroelectric (FE) distortion of the perovskite cubic cell. This distortion is characterized by a cooperative displacement of the center of positive charges opposed to the displacement of the center of negative charges, as depicted in panel (b) of Figure 1.1. Since the center of positive and negative charge are separated, a dipolar momentum appears in the cell. The consequence of this structural distortion is the spontaneous polarization that appears in ferroelectric materials. The FE distortion is usually accompanied by an elongation of the cell in the direction of the dipolar moment, and can occur along different crystallographic axes at the same time - an example is the ground state of barium titanate ($BaTiO_3$) at low temperatures, which is characterized by a polarization parallel to the [111] axis and a rhombohedral unit cell [8].

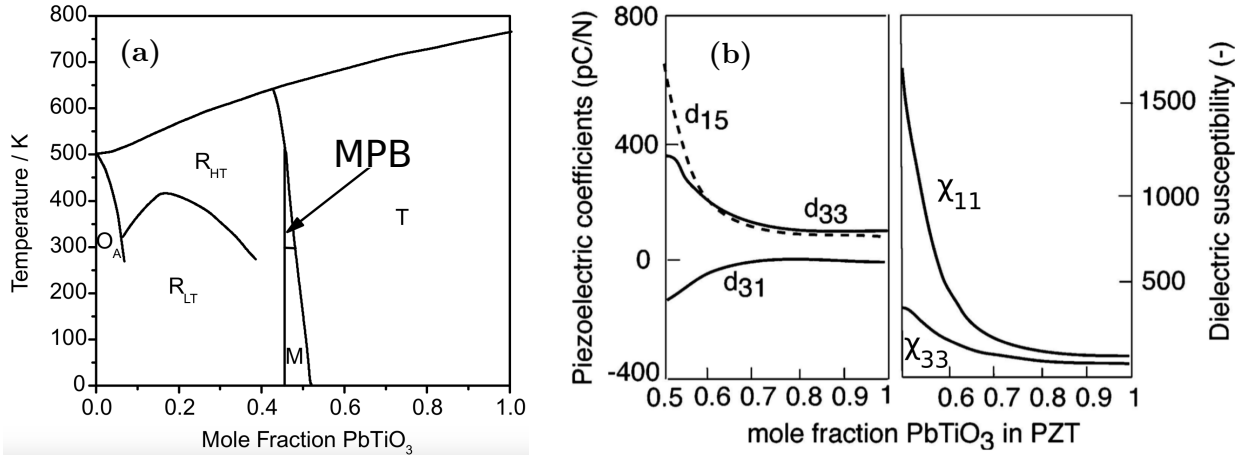


**Figure 1.6: Experimental and theoretical results for the study of the MPB in PZT. (a)** Experimental phase diagram of PZT from Ref. [9], showing the narrow MPB. The diagram is displayed both as a function of the mole composition of $PbTiO_3$ and the temperature. **(b)** Theoretical study of the piezoelectric coefficients and the dielectric susceptibility of PZT for varying mole fraction of $PbTiO_3$ from Ref. [10]. The model used for the study is a Landau-Ginzburg-Devonshire developed in Ref. [11].

### 1.1.4 Application and optimization of functional perovskite oxides

One of the most studied properties of perovskites over the last decades is piezoelectricity due to its potential functionalization and application for device design. The perovskite solid solution lead zirconate titanate (PZT or $PbZr_{1-x}Ti_xO_3$, where the $B$ crystallographic site can either be Zr or Ti and $x$ represents the mole fraction) is an example of a material for which optimization provided outstanding piezoelectric properties.

Panel (a) of Figure 1.6 shows the phase diagram as described in Ref. [9]. In the Figure, $R_{LT}$ and $R_{HT}$ are rhombohedral phases displaying a polarization parallel to the [111] crystallographic axis. As the concentration of Ti increases, the phase diagram crosses the so-called morphotropic phase boundary (MPB) and the ground state becomes a tetragonal phase with polarization parallel to the [001] crystallographic axis. It is precisely within the MPB that the susceptibility and the piezoelectric coefficient of the material is maximized (see panel (b) in Figure 1.6).

The origin of the large values for the susceptibility and the piezoelectric coefficients achieved at the MPB are two-fold. First, as discussed in Section 1.1.1, large values of the dielectric susceptibility indicate low energy cost to develop a structural distortion. As a consequence, the polarization of the material can rotate from [111] to [001] without huge energetic costs. Second, the works in Ref. [12] and Ref. [13] show the existence of a monoclinic phase at the MPB, allowing for a continuous rotation of the polarization. The explanation proposed in these works is that, instead of different phases coexisting within the MPB, the monoclinic phase acts as a bridging phase that allows the material to transit from the rhombohedral phase to the tetragonal phase in a continuous way.

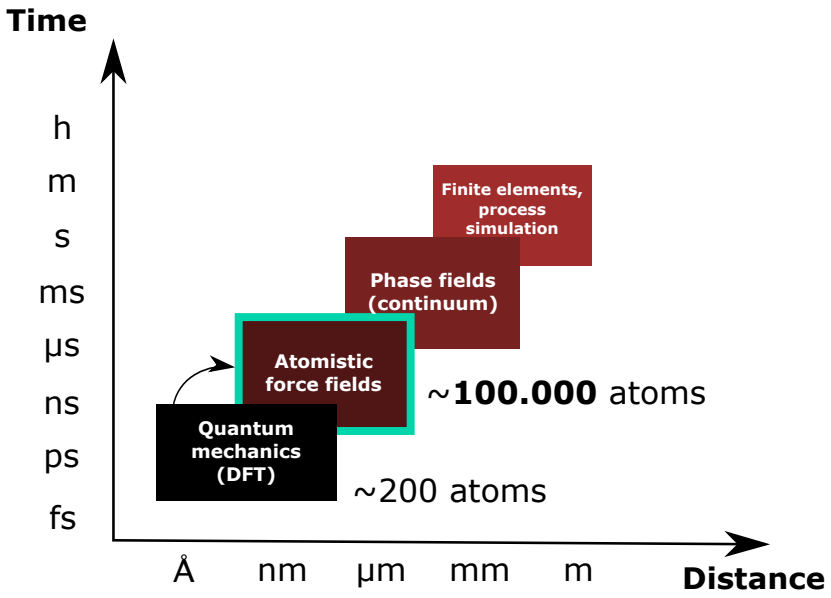


**Figure 1.7:** Comparative diagram of different simulation techniques, focusing on their accessible simulation box size.

## 1.2 Predictive simulations in Materials Science

Traditionally simulations have been widely used to understand (and predict) the properties of materials, although the field is wide enough to include applications to Biology [14] or Chemistry [15]. In the context of this Thesis the simulation domain is within Condensed Matter theory, and in particular, the study of the Perovskite materials.

The scientific community in Materials Science has a applied a substantial effort to study materials from a theoretical point of view. A way of achieving this is through computational simulations that allow to study the behavior of materials under simulated conditions. The level of detail of the theory used to perform the simulations depends on the nature of the problem of interest, ranging from continuum models of matter [16] to first-principles theory in which the most fundamental quantum-mechanical description is applied [17]. In Figure 1.7 I show a schematic of the time and spatial scales that the different simulation approaches typically have access to.

### 1.2.1 Quantum mechanical simulations and DFT

The most accurate known theory to study condensed matter at the atomic scale is Quantum Mechanics. The theory provides a complete description of the system through the Schrödinger equation, which consists on the eigenvalue problem of the Hamiltonian associated to it. The solution of the equation provides the information necessary to understand all the processes that occur in the crystal lattice.

Let us consider a set of atoms with $N_e$ electrons, organized in a crystal lattice. In the Born-Oppenheimer approximation one considers that the nucleus of the atoms can be represented by a potential acting on the electrons, as the relaxation time of the electrons is much faster than the

nuclei due to the difference of masses. Let us call this potential

$$v_{\text{ionic}}(\mathbf{r}_i) = \sum_k \frac{qQ_k}{|\mathbf{r}_i - \mathbf{R}_k|}, \tag{1.2.1}$$

where $\mathbf{R}_k$ stands for the coordinates of the atom nuclei, $\mathbf{r}_i$ are the coordinates of the electrons, $q$ is the electron charge and $Q_k$ is the charge of the nucleus $k$. The Born-Oppenheimer approximation allows to write the Schrödinger equation in terms of a wavefunction $\varphi = \varphi(\mathbf{r}_1, \ldots, \mathbf{r}_{N_e})$ which depends only on the electronic coordinates. The non-relativistic Schrödinger equation associated to the problem is then [18]

$$\sum_i \left( -\frac{\hbar \nabla_i^2}{2m_e} + v_{ext}(\mathbf{r}_i) + \sum_{i<j} U(\mathbf{r_i}, \mathbf{r_j}) \right) \varphi(\mathbf{r}_i, \ldots, \mathbf{r}_{N_e}) = E\varphi(\mathbf{r}_i, \ldots, \mathbf{r}_{N_e}) \tag{1.2.2}$$

where the term $\frac{\hbar \nabla_i^2}{2m_e}$ is the kinetic energy operator of the electrons (with mass $m_e$), $U(\mathbf{r}_i, \mathbf{r}_j)$ is the electrostatic electron-electron Coulombic interaction, $v_{ext} = v_{\text{ionic}} + v_{\text{fields}}$ and $E$ is the energy associated to the eigenstate $\varphi$. The term $v_{fields}$ accounts for additional external applied fields.

The computational solution of this $N$-body problem is extremely complex. An illustration of this can be shown by assuming the integration of the problem using a mesh of M points. Since there are $N_e$ electrons and three cartesian directions in the 3D space, there are $M^{3N_e}$ values to be computed. For a simple mesh of 10 points and a problem involving 10 electrons, the problem requires the calculation of $10^{30}$ values for the description of the wavefunction.

A different approach to tackle the $N$-body problem is the Density Functional Theory. Formally, the electronic density is given by

$$n(\mathbf{r}) = N_e \int d^3 r_2 \cdots \int d^3 r_{N_e} \varphi^*(\mathbf{r}, \mathbf{r}_2, \ldots, \mathbf{r}_{N_e}) \varphi(\mathbf{r}, \mathbf{r}_2, \ldots, \mathbf{r}_{N_e}). \tag{1.2.3}$$

One of the most relevant and surprising results in the DFT is that this relationship can be reversed [19]: if the density function of the ground state $n_0(\mathbf{r})$ is found, then the wavefunction of the ground state $\varphi_0(\mathbf{r}_1, \ldots, \mathbf{r}_{N_e})$ can be found as it can be written as a functional of the density. That is to say, the information contained in the wavefunction of the ground state is the same information available in the electron density function.

This result, presented by Hohenberg and Kohn in Ref. [19] and known as the HK theorem, has several implications. Since the ground state wavefunction is a functional of the density, the observables can be written as a functional of the density - and particularily, the energy of the ground state can be written as a functional of the density. This energy, which depends on the definition of $v_{\text{ionic}}(\mathbf{r}_i)$, is usually then written as

$$E[n] = T[n] + U[n] + V_{\text{ext}}[n] = T_s[n] + T_c[n] + U_H[n] + U_x[n] + V_{ext}[n] \tag{1.2.4}$$

where $T$ and $U$ are called universal functionals of the density (independent of $v_{\text{ionic}}(\mathbf{r}_i)$) and $V_{\text{ext}}$ is the potential energy due to the atomic nuclei and additional external fields. In the last expression, $T = T_s + T_c$; here, $T_s$ is the sum of the single particle kinetic energies, which is the main contribution to $T$; $T_c$ is the correlation energy, defined as $T_c = T - T_s$. On the other hand, $U = U_H + U_x$, where $U_H$ is the Hartree energy that accounts for the simple electrostatic interaction between electrons, and the main contribution to $U$; while $U_x$ is the exchange energy. The exchange

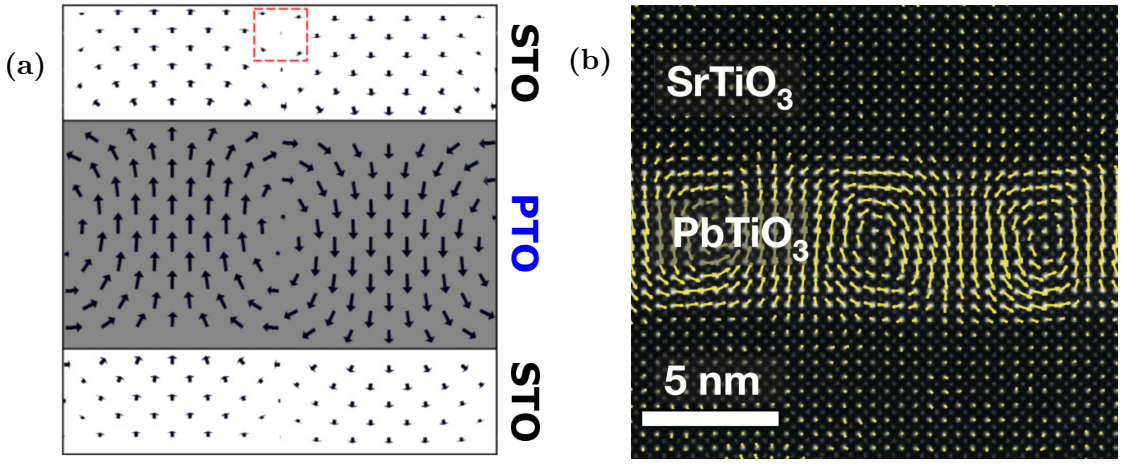


**Figure 1.8:** Comparative of the experimental observation of polarization vortices in PTO/STO superlattices and theoretical relaxation of the same phase using DFT. **(a)** Theoretical calculation of the metastable phase displaying vortices of electric dipoles in the PTO layers of PTO/STO superlattices, from Ref. [20]. **(b)** Experimental observation of local dipoles arranged in vortices in the PTO layers of PTO/STO superlattices, from Ref. [21].

and correlation energy contributions are usually written as the exchange-correlation energy contribution, $E_{xc} = T_c + U_x$. This energy term is ensured by the Hohenberg-Kohn theorem to be a functional of the density. It is important to note that the theory formulated thus far is formally exact.

Additionally to the dramatic simplification that the HK theorem implies for the solution of the $N$-body problem, Kohn and Sham proposed an efficient iterative scheme to solve the Schrödinger equation [22]. This method proposes a way of calculating the exchange-correlation energy through an approximative expression for the exchange-correlation potential $v_{xc}[n]$, in which an associated problem of non-interacting electrons is solved. The key in the process is the self-consistent cycle that leads to the convergence of the exchange-correlation energy, in which the interaction of the electrons is recovered, leading to an electron density that coincides with that of the original problem. The solution to the problem is found by calculating the variation of the energy over the density,

$$H_{KS} = \frac{\delta E}{\delta n} = \frac{\delta T_s}{\delta n} + v_{xc} + v_H + v_{ext}. \tag{1.2.5}$$

The non-interacting electron Schrödinger equation is then

$$\left( \frac{-\hbar \nabla^2}{2m_e} + v_{xc} + v_H + v_{ext} \right) \varphi_l(\mathbf{r}) = E_l \varphi_l(\mathbf{r}) \tag{1.2.6}$$

where $l$ labels the orbital of the electron. The density is then calculated as

$$n(\mathbf{r}) = \sum_l f_l |\varphi_l(\mathbf{r})|^2, \tag{1.2.7}$$

where $f_l$ is the occupation of the $l$-th orbital.

The DFT approach to solve the quantum-mechanical problem is an efficient strategy. This allowed to conduct investigations on crystalline materials with a great level of accuracy and agreement with experimental results. An example of this is the work in Ref. [20] on $(SrTiO_3)_n/(PbTiO_3)_n$

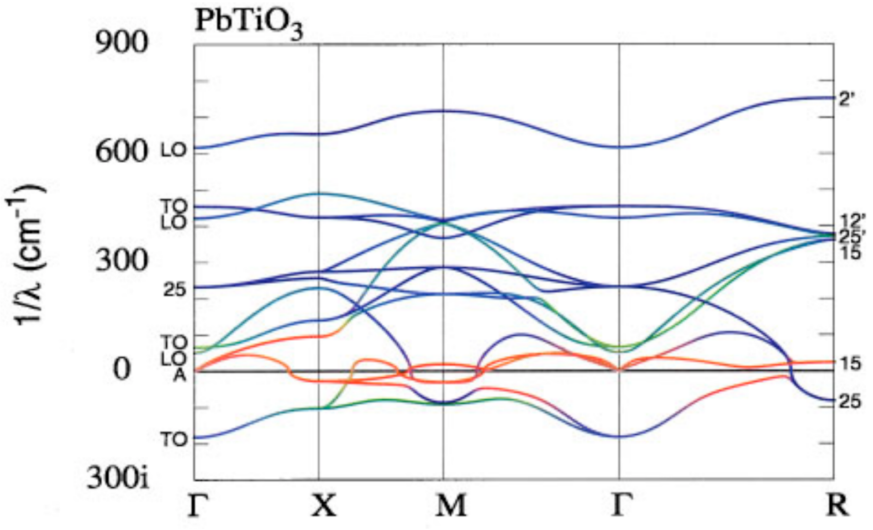


**Figure 1.9:** Phonon dispersion of the cubic phase of lead titanate as computed using DFT, from Ref. [23]. The colors indicate the contribution to the eigenvectors of the different atoms: red is used for the A cations, green for the B cations and green for the oxygen contribution.

superlattices, in which they were able to predict the energetics of a phase displaying polarization vortices (panel (b) of Figure 1.8) that was later observed experimentally [21] in the $PbTiO_3$ layers (see panel (a) of Figure 1.8).

Another example of the advantage of using DFT is the work presented in Ref. [23]. Here, the authors used DFT to study the phonon dispersion of the cubic phase of $BaTiO_3$, $PbTiO_3$ and $PbZrO_3$. Notably, they were also able to characterize the vibrations by analyzing the contribution of the different atomic species to the eigenvectors. The analysis of the vibrations provides information on the structural instabilities of the materials.

Other important examples of the application of Density Functional Theory in the context of ferroic materials are the study in Ref. [24] analyzing the limit thickness at which the ferroelectric instability of barium titanate thin films disappears, or the research performed in Ref. [25] of multiferroic thin films of bismuth ferrite, in which the origin of the enhancement of its intrinsic polarization is studied.

### 1.2.2 First-principles based models

Although the DFT greatly eases the calculation of the solution of the quantum-mechanical problem it is still a challenge to compute simulation boxes of more than 200 of atoms. In particular, it is all but impossible to access large-scale simulations using DFT.

This limitation has motivated the development of several approaches to access larger scale simulation boxes (see Figure 1.7). This is usually achieved by reducing the detail level, and force fields methods are a fantastic example of this. This modelization family is typically characterized as an all-atom approach in which the energy of the crystal or the molecules is parametrized by describing the atomic interactions of the system in a simplified form. It is also relatively customary to use DFT to compute the parameters of the model. The name of this family of models arises from the utility they provide at performing large-scale molecular dynamics, for which one solves the

equations of motion using a defined potential. Although it is true that such simulations can be run using first-principles calculations, force fields models allow to simulate much larger simulation boxes.

In the literature there are several examples of force fields model potentials that are fitted using DFT data. It is a particularily strong field of development in computational chemistry, with outstanding examples as the Reactive Force Fields (ReaxFF) amongst many others (I particularily recommend Table I in Ref. [26] for an updated summary of the different potentials and their capabilites). Also, effective model potentials have been used in the past to perform simulations of large simulation boxes with coarse-grained description of the systems. I review in Section 2.1 some of the examples aforementioned.

This Thesis is developed around a recent formulation of force fields models: the SCALE-UP model potentials [27], presented in 2013. The formulation of the models, which is described in Section 2.2, is based on a Taylor expansion of the energy, and hence it is very flexible and general. As such, the models are well suited to be fit to first-principles data, providing an outstanding approximation of the energetics of the crystalline materials.

The extense applicability of this formulation has lead many works to arise recently, allowing the characterization of PTO 180º domain walls with in-plane polarization [28], providing insight on thermal transport across $PbTiO_3$ 180º domain walls[29, 30], or the first theoretical study of electric skyrmions in homogeneous systems [31].

In the original methodology presented in Ref. [27] the authors propose a numerical scheme to fit the coefficients of a selected set of terms representing atomic interactions of particular physical importance to describe the systems. This method to obtain models is, however, a priori not flexible and relies on the manual identification of the most important interactions in the system. Also, the numerical optimizations performed in the process slow significantly the model production.

The original formulation of the models is well adapted to describe single perovskite systems. One of the perspectives of the SCALE-UP model potentials is the deveolpment of a methodology to model complex systems, as chemically inhomogeneous or nanostructured materials. This, however, was not explored by the authors and requires a further formulation development.

## 1.3 Objectives

Based on the general topic overview presented in this Thesis I defined main objectives to achieve in this work, that I believe constitute an important scientific development and have a very positive contribution to research, and which development is expressed in this Manuscript.

The first objective was to design an automatic methodology to generate models. As I discuss in the paragraphs above the SCALE-UP model potentials have a strong potential applicability. The development of a general approach for the model construction process was the natural continuation of the work in Ref. [27], as it would allow to easily produce models for the scientific problems of interest and reduce the time devoted in the model construction itself.

The second objective of this Thesis arose from the high scientific interest of studying chemically inhomogeneous systems. The simulation box size that this kind of simulation requires is, in general,

beyond the capabilities of DFT simulations due to the high computational cost involved. Instead, the idea of exploring the applicability of SCALE-UP model potentials to study this family of systems is an enticing approach, as it is a much lighter framework to approach the problem from the computational point of view. Potentially, this would allow to study a very wide variety of systems, as could be nanostructured crystals or property-engineering through material design [32, 33].

Finally, I also wanted to explore the applicability of the models that I could generate by achieving the first objective. Since the test system for the demonstration of the process was $SrTiO_3$ it was natural to use a produced model potential to study an open problem. The study of the domain walls in strontium titanate has been extense in the literature, although the structure and properties they may exhibit are still subject of discussion. Consequently I decided to study the structure and properties of the 180º anti-phase domain walls of this material.

The Manuscript is organized as follows. In Chapter 2 I review some modelization approaches that have been widely used in the field. Also, I introduce the SCALE-UP model potentials, which are the model potentials I use on the development of this research. In Chapter 3 I present and discuss the methodology developed for the construction of SCALE-UP models. This methodology is applied to construct a model for $SrTiO_3$, with which I studied the transition temperature of the material as an example of application. In Chapter 4 I develop the formulation of model potentials suitable for studying chemically inhomogeneous systems, with a brief application to $SrTiO_3/PbTiO_3$ superlattices. Finally, in Chapter 5 I present a discussion on the applications of SCALE-UP model potentials. In particular, I use the model potential developed in Chapter 3 to study the 180º anti-phase domain walls in $SrTiO_3$. In Chapter 5 I also summarize briefly two collaboratinos in which I have participated and which involve SCALE-UP simulations.

# Chapter 2

# Atomistic model potentials

I review in this Chapter different approaches when it comes to modeling the potential energy of a material without explicitely solving the electronic problem at the quantum-mechanical level. First, in Section 2.1.1 I describe examples of model potentials that have been widely used in Materials Science research. These model potentials have the characteristic of being computationally much more efficient than DFT calculations, with their parameters obtained either using first-principles calculations or experimental data. In Section 2.2 I describe in detail the formulation for the SCALE-UP model potentials, in which one can see reflected some of the ideas of the different methods introduced in the first Section of this Chapter. This family of models will be then used throughout this Thesis.

## 2.1 Examples of model potentials

I contextualize the SCALE-UP model potentials by discussing a collection of model potentials that are present nowadays in research. The ideas behind the motivation and the formulation of these model potentials are in a way recovered by the second-principles model potentials.

The core of defining models for materials consists in formulating with physical relevance the energy of the material through approximations. Techniques for very accurate material studies such as DFT have been succesfully developed. However, they are not well suited for the study of large-scale phenomena. Typically these calculations require large simulation boxes, and the computational cost of solving the electronic problem limits the simulation boxes that can be accessed. For this reason, several examples of modelization without explicit treatment of electrons at a quantum-mechanical level have been extensively developed and used in material science, providing new insights and better understanding of the driving physical or chemical mechanisms related to the macroscopic phenomena of interest.

### 2.1.1 All-atoms effective models

I describe here two families of models developed using atomistic perspectives. The all-atoms effective models (or force fields) usually define a set of atomic interactions that describe the lattice-dynamical properties of the system. Here I review two methods, namely the Lennard-Jones potentials and the Reactive Force Fields (ReaxFF), that describe the interaction between atoms in a simplified form.

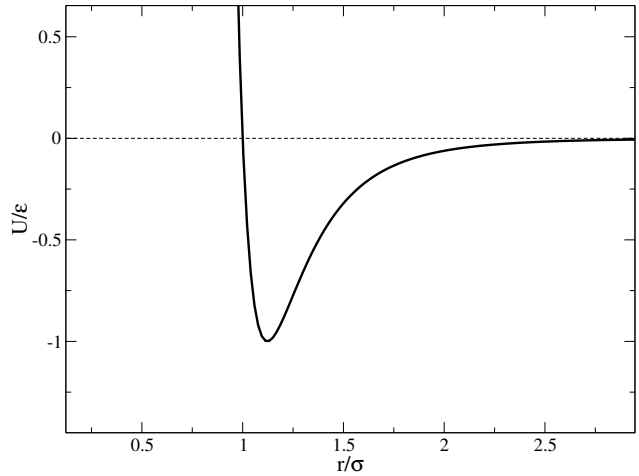


**Figure 2.1:** Potential energy for the diluted Neon gas as a function of distance between particles, computed used the Lennard-Jones potential in a desktop machine. I used the tabulated values for the Neon gas from [1].

### The Lennard-Jones potential

One of the canonical examples of model potentials in materials science are the Lennard-Jones potentials [34]. This potential has its origin in the equation of states of gases and models the interaction between pairs of atoms, and more precisely, in the second coefficient of the empirical equation

$$pv = A + \frac{B}{v} + \frac{C}{v^2} \cdots + \frac{F}{v^8}, \tag{2.1.1}$$

where $p, v$ are the values of pressure and volume and the coefficients $A$ to $F$ correspond to empirical coefficients. The coefficients are typically extracted through experimental observations in temperature. In the derivation of the potential the focus of the work in Ref. [34] starts at approximating the equation of state of a gas that is strongly diluted,

$$pv = k\mathrm{NT}\left(1 + \frac{B}{v}\right). \tag{2.1.2}$$

This equation of state can be integrated if one considers molecules with spherical symmetry to obtain the second coefficient $B$. In the derivation, the authors assume that a central force exists between the molecules which is inversely proportional to the distance between them. With this it is possible to recover the potential energy through integration, leading to the usual form of the Lennard-Jones potential energy,

$$U(r) = 4\epsilon\left[\left(\frac{\sigma}{r}\right)^m - \left(\frac{\sigma}{r}\right)^n\right]. \tag{2.1.3}$$

where $\epsilon$ represents the depth of the potential well, $\sigma$ is the zero force interaction distance and $r$ is the distance between the pair of particles. Normally the exponents used for studying noble gases are $n = 6$ and $m = 12$, where the constraint on the $m$ exponent is to be greater than $n$; however, the determination of the exponents depends on the material of study [35]. The term $r^{-12}$ is intimately related to the description of the atomic repulsion due to the Pauli exclusion principle [1, 5]. The sixth-order term of the power law is related to the Van der Waals attractive interaction.

The potential typically takes the form depicted in Figure 2.1. As can be seen, it describes a minimum corresponding to the equillibrium interaction distance. Before the minimum, the derivative of the potential indicates that the interatomic forces are strongly repulsive, indicating the dominance of the $r^{-12}$ term. After the minimum, the forces begin to be attractive, suggested by the positive slope of the curve. The interaction is, as expected, converging to zero as the distance goes to infinity. Because of the simplicity of the energy expression it is possible to analytically study the optimal bond distance:

$$f(r) = \frac{dU(r)}{dr} = -4\epsilon \left[ 12 \left( \frac{\sigma^{12}}{r^{13}} \right) - 6 \left( \frac{\sigma^{6}}{r^{7}} \right) \right], \tag{2.1.4}$$

$$f(r) = 0 \Leftrightarrow 12 \left( \frac{\sigma^{12}}{r^{13}} \right) - 6 \left( \frac{\sigma^{6}}{r^{7}} \right) = 0 \Leftrightarrow r = 2^{1/6}\sigma, \tag{2.1.5}$$

showing the point at which the interaction reaches its equillibrium point. Also, it is clear that for $r < 2^{1/6}\sigma$ the forces become repulsive, and for $r$ beyond that value, the forces are attractive.

This power law expression for the interaction of atoms in a molecule is extremely flexible and computationally efficient. For example, one can use tabulated values in temperature of noble gases to fit the coefficients of the Lennard-Jones potential (for the conditions in which the approximation holds). Then, one can extend the equation for $N$ particles in a crystal [1]

$$U_{tot} = \frac{4\epsilon}{2} N \left[ \sum_{ij} \left( \frac{\sigma}{p_{ij}R} \right)^{12} - \left( \frac{\sigma}{p_{ij}R} \right)^{6} \right] \tag{2.1.6}$$

where $p_{ij}R$ represents the distance between atoms $i$ and $j$, and $R$ is the nearest neighbor distance. Since this energy expression is analytically very simple it allows to perform statistical simulations to study materials in large simulation boxes. For example, the calculation of the force on the atoms or molecules is a simple task, opening the possibility to perform Molecular Dynamics simulations at large-scale. It is for this reason that the Lennard-Jones has been widely used for many applications, from modeling of metals [35] to studying phase diagrams of fluids [36], amongst many other examples of application.

### Reactive force fields

The ReaxFF (Reactive Force Fields) is a more recent approach for modeling, presented in Ref. [37]. The peculiarity of this force field model is that it is focused on describing accurately the reactivity of the bonds. The effective potential is formulated in a way that allows for explicit treatment (in an effective way) of the electrons, so that the model can simulate bond deformation, bond breaking/formation and electron hoping without having to solve the problem at a quantum-mechanical level. The model retains a great level of accuracy, as the functional parameters are fitted to DFT.

The main motivation for the formulation of this model potentials is that, even though existing force fields models for quantum chemistry simulation reproduce well the geometries and properties of chemical compounds [38–40] they fail to describe properly the chemical reactivity. In their formulation, van Duin et al. describe the energy of the system as a combination of several contributions related to the description of the bonds:

$$E = E_{\text{bond}} + E_{\text{over}} + E_{\text{under}} + E_{\text{val}} + E_{\text{pen}} + E_{\text{tors}} + E_{\text{conj}} + E_{\text{vdWaals}} + E_{\text{Coulomb}} \tag{2.1.7}$$

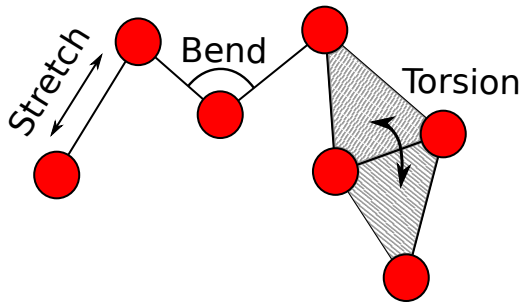


**Figure 2.2:** Sketch of the main degrees of freedom considered for the bonds by the ReaxFF models.

The first contribution, $E_{\text{bond}}$, is the energy related to the bond. It is characterized by a functional that defines the bond order as a function of the bond length and depends on the available bonds in the compound. For example, in Ref. [37] the authors consider the different bonds that may occur between the atoms of hydrocarbon compounds (for carbon-carbon, for example, they consider the sigma bond and the two pi bonds possible by studying the different orbitals involved in bond). This allows to construct a functional that accounts for the correct coordination of the atoms by studying their valences.

This leads to the second and third energy contributions, $E_{\text{over}}$ and $E_{\text{under}}$, related to the over and undercoordination of the atoms. In this way it is possible to model the bond formation or creation: an overcoordinated atom will introduce a penalty to the energy so that the atom will be prone to change its coordination. Analogously, undercoordination will translate into favoring electron transition to create additional bonds or modifying the order of the bond in the uncoordinated atoms. The penalties are accounted through the $E_{\text{pen}}$ energy term.

They describe the $E_{\text{val}}$ as the energy related to the angle of the bond (depicted by the bend described in Sketch 2.2), which is sensitive to the bond order. In this way, the atoms are allowed to move while the energy of the bond is accounting for the bond angles. This term is relevant to predict the geometries of the modeled system, which is a key factor in studies of organic molecules. Similarily, $E_{\text{tors}}$ accounts for the torsion of the angles, which has an impact on how the bonds between atoms can rotate, leading to rotations of parts of the molecule.

The model accounts also for the energy contribution of conjugated systems, described in the energy contribution term $E_{\text{conj}}$. This energy is descriptive of how the bonds of $p$ orbitals in molecules help in stabilization by delocalizing the electrons, typically by alternating single and double/triple bonds. The electrons delocalize accross the subsequent $p$ orbitals, for which the ReaxFF models the energetics through the bond order parameters.

Finally, the model potential takes into account the Van der Waals interactions and Coulombic forces in the system ($E_{\text{vdWaals}}$ and $E_{\text{Coulomb}}$ terms). The effect of this is relatively similar to that of the Lennard-Jones potential, effectively modeling the repulsion/attraction forces appearing between atoms due to these sources. This interactions are essential to describe how the bonds can stretch.

The parameters included in the different terms of the energy are computed using DFT. Because of the detailed description of the energetics, the models achieve a high accuracy when compared to the results of first principles calculations. They focused on optimizing the force fields model through fitting the target interaction distances, so that the model is effectively reproducing ab-initio predicted forces in the region of interest while being much lighter in the calculation of the energy.

To demonstrate the usefulness of the model, the authors studied the bond dissociation of a variety of compounds, from single to multimolecular aromatic systems. They compared the obtained results for heat of formation with experimental values, obtaining differences of the order of 10 kcal/mol for either radicals or conjugated systems. Also, they compared the geometries of the molecules as calculated using ReaxFF compared to experimental results, obtaining angles that are deviated by usually less than 0.1 degrees.

Nowadays the ReaxFF approach has been applied to study a wide variety of systems. In computational chemistry it has been extensively used to study organic compounds reactivity [41]. The method has been applied to study ferroelectric perovskite crystals as well [42, 43]. It has also been used to analyze how sodium wears graphite cathodes for battery applications [44] and to simulate the combustion of char in different atmospheric conditions [45], using simulation boxes of tens of thousands of atoms. Recently, it has been also used to understand the proton transfer of $H_3O^+$ and $OH^-$ in water, proving that ReaxFF is also adequate to study acid/base reactions in aqueous solutions [46].

### 2.1.2 Coarse-grained modeling. The Effective Hamiltonians.

A common approach to modeling is the definition of coarse-graining approximations. The idea behind is to define new simplified entities representing a collection of atoms. This reduces the degrees of freedom of the system and allows for much simpler calculations. As a consequence, much larger simulation boxes can be computed. This approach has been used widely in fields like biology, in which one can think of different degrees of *grains*: aminoacids, proteins, or glucids can be modeled as single entities that interact with their environment, overlooking the detail of the atomic interactions and focusing on the properties that the whole structure exhibits [47]. In materials science, an example of coarse-graining are the Effective Hamiltonians proposed by W. Zhong, D. Vanderbilt and K. Rabe in their modeling of Barium Titanate [8], the formulation for which is discussed in Ref. [48].

#### Effective Hamiltonians

The Effective Hamiltonians are non-atomistic models of the potential energy of materials. The coarse-graining step consists on defining a new set of variables in which the system is modeled. Here, instead of treating explicitely all the atoms in the system, the authors introduce a new entity that they call *local modes*. In the case of the ferroelectric materials, the local mode proposed by the authors consists on a 3D vector for which the components are the amplitude of the ferroelectric polar distortion (FE) of the perovskite 5-atom cubic unit cell. The coarse-graining is sketched in Figure 2.3.

In order to obtain the FE distortion characteristic of Barium Titanate the authors use the eigenvector associated to the FE instability of the force-constant matrix (also known as the Hes-

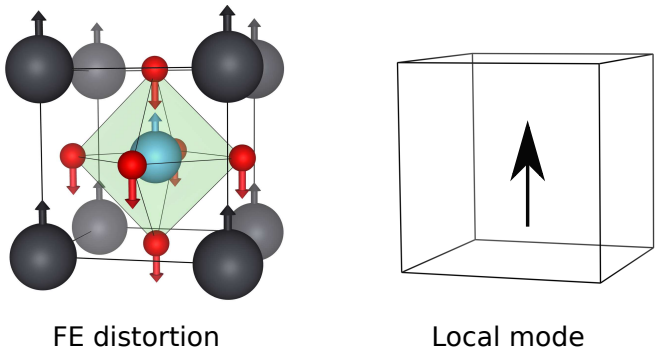


**Figure 2.3:** Sketch of the coarse-graining step. At the left, the FE distortion of the cubic cell. At the right, the quantity that substitutes it in the model, the local mode.

sian Matrix). The new system is then constructed by assigning a local mode to each cell contained in the simulation, as sketched in Figure 2.4.

The energy functional proposed by W. Zhong and collaborators is

$$E(\{\mathbf{u}_i\},\boldsymbol{\eta}) = E^{\text{self}}(\{\mathbf{u}_i\}) + E^{\text{dpl}}(\{\mathbf{u}_i\}) + E^{\text{short}}(\{\mathbf{u}_i\}) + E^{\text{elas}}(\boldsymbol{\eta}) + E^{\text{int}}(\{\mathbf{u}_i\},\boldsymbol{\eta}). \tag{2.1.8}$$

Here, $\mathbf{u}_i$ is the local mode related to the $i$-th cell and $\boldsymbol{\eta}$ are the homogeneous strains of the system. In the following paragraphs I describe the different contributions of the energy.

The first term is the energy related to the local mode itself. It is modeled using a fourth-order polynomial that is compliant with the symmetry of the local mode. The energy contribution is

$$E^{\text{self}}(\{\mathbf{u}_i\}) = \sum_i \left[\kappa_2 u_i^2 + \alpha u_i^4 + \gamma(u_{ix}^2 u_{iy}^2 + u_{iy}^2 u_{iz}^2 + u_{iz}^2 u_{ix}^2)\right]. \tag{2.1.9}$$

where $i$ labels the cells of the system. The different parameters $\kappa$, $\alpha$ and $\gamma$ are determined using DFT. This can be usually done by considering structures related with the mode for which the energy or its derivatives are calculated using first-principles.

The second term of the energy corresponds to the long-range dipole-dipole interaction that is present in semiconductors or insulator materials, in which there is no free charge distribution preventing for the Coulomb interactions to appear. These interactions are in nature of infinite range. For its description the Born effective-charge tensor ($Z^*$) and the high-frequency dielectric permitivity tensor ($\epsilon_\infty$) are used. Since the atoms have not an explicit description in the model it is required to calculate the Born effective charge of the local mode itself. This is done by projecting the Born effective charges of the atoms by the local mode. The Coulomb energy interaction is

$$E^{\text{dpl}}(\{\mathbf{u}_i\}) = \frac{Z^{*2}}{\epsilon_\infty} \sum_{i<j} \frac{\mathbf{u}_i \cdot \mathbf{u}_j - 3(\mathbf{R}_{ij} \cdot \mathbf{u}_i)(\mathbf{R}_{ij} \cdot \mathbf{u}_j)}{R_{ij}^3} \tag{2.1.10}$$

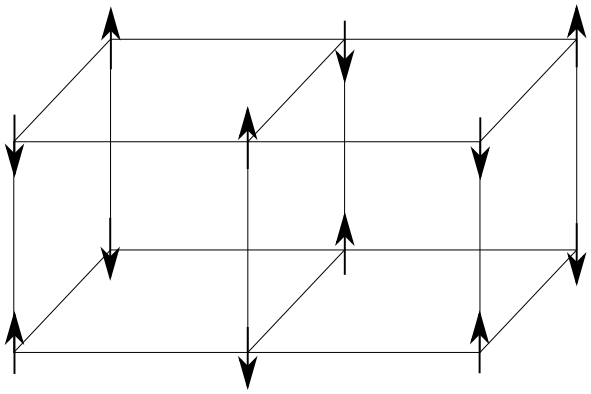

**Figure 2.4:** Sketch of the coarse-grained system with a certain arrangement of local modes. Each vertex in the sketch corresponds to the center of a cell, and the arrows represent the local mode associated to the cells.

where $\mathbf{R}_{ij}$ is the vector from the center of cell $i$ to the center of cell $j$. This expression is then adapted to ease the computation by performing an Ewald summation. This is also an example of how calculations can be performed faster, as the result can be written in a compact way of the type

$$E^{\text{dpl}}(\{\mathbf{u}_i\}) = \sum_{i\alpha j\beta} Q_{i\alpha j\beta} u_{i\alpha} u_{j\beta} \tag{2.1.11}$$

where $Q_{i\alpha j\beta}$ is a matrix that can be calculated beforehand containing the results of the Ewald sum.

The third term of the model is the short-range interaction between modes. This can be written as

$$E^{\text{short}}(\{\mathbf{u}_i\}) = \frac{1}{2} \sum_{i\neq j} \sum_{\alpha\beta} J_{i\alpha j\beta} u_{i\alpha} u_{j\beta} \tag{2.1.12}$$

where $J_{i\alpha j\beta}$ represents the interaction matrix. This interaction matrix has a strong decay in interaction distance, and similarily to the local mode self energy contribution, symmetry considerations can greatly simplify the calculation of its components by analyzing the interaction between neighbors. In Ref. [48], they consider interactions up to third nearest-neighbors for the insulator perovskite barium titanate.

The elastic energy is the next contribution to the energy in the model. It is split between the homogeneous strain and the inhomogeneous strain contributions (the latter will not be discussed in this Manuscript). The symmmetry of the cubic perovskite cell eases the form of the former, which can be written as

$$E_H^{\text{elas}}(\boldsymbol{\eta}) = \frac{N}{2} \sum_{l=1\ldots6} B_{ll} \eta_l^2 + \frac{N}{2} \sum_{\substack{l=1\ldots3 \\ m=1\ldots3 \\ l\neq m}} B_{lm} \eta_l \eta_m \tag{2.1.13}$$

where $\eta_l$ are the homogeneous strains written in Voigt notation, and $B_{lm}$ are the components of the bare (also called *undressed*) elastic tensor. The final contribution to the energy considered

in the model is related to the coupling between the strains and the local modes,

$$E^{\text{int}}(\{\mathbf{u}_i\}, \boldsymbol{\eta}) = \frac{1}{2} \sum_i \sum_{l\alpha\beta} B_{l\alpha\beta} \eta_l u_{i\alpha} u_{i\beta} \tag{2.1.14}$$

This model is a good example of how coarse-graining can help in improving the efficiency of simulations of materials properties. The model is fitted to DFT data, which means that it consists on an approximation to the DFT energy having a complete description of the physics of the system. A polynomial-like energy is naturally much faster to compute than solving the Schrödinger equation in DFT, and hence simulation boxes of 10.000 to 20.000 atoms could be computed. This enabled the authors to study the phase diagram of Barium Titanate using Monte Carlo simulations to compute the transition temperatures of the different phases of the material, a calculation that remains inaccessible nowadays using DFT. Further, the model potentials where applied to a wide variety of perovskite compounds, such as Strontium Titanate, proving that the methodology is flexible. In Ref. [13] an example of application for $PbZr_{1-x}Ti_xO_3$ can be found, combining the Effective Hamiltonians with the Virtual Crystal Approximation to study the morphotropic phase boundary of the material, key in the remarkable piezoelectric response of the material.

Nowadays the model potentials presented are extensively used for materials science research. For example, it has been intensively used to study electrocaloric and inverse electrocaloric effects of barium titanate and its potential tunability [49–51], predictive phase discovery on bismuth ferrite [52], studies on the relaxor ferroelectric lead manganate niobate [53, 54] or on the analysis of the origin of the ground state of $NaNbO_3$ [55], a material particularily challenging to study from a theoretical point of view due to the extreme complexity of its potential energy surface.

## 2.2 SCALE-UP: second-principles model potentials

The methods for model construction developed during this Thesis project focus on a particular flavor of Force Fields model potentials introduced in Ref. [27], which coined the name for the family of models of this kind as Second Principles. In particular, the models have been implemented for computer simulations in the `SCALE-UP` package (**S**econd-principles **C**omputational **A**pproach for **L**attice and **E**lectrons). In this Section I introduce the general notation and describe the formulation of this family of methods, focusing on the *lattice* part of the model.

### 2.2.1 Introduction: polynomial model potentials for crystals

As it has been discussed previously many approaches have been used in the past to overcome the practical limitations of DFT. This case is no exception of a general rule: the goal is to transform the difficulty of computing the energy via solving the many-body Schrödinger equation into a polynomial expression of the energy that allows for faster calculations, hence increasing the accessible simulation box and simulation time and accessing scientific research that is, in practice, out of the reach of first-principles calculations. As in the previous examples, the model does not involve explicit treatment for the electrons.

The formulation of the second-principles model potentials within `SCALE-UP` is developed in the form of a Taylor expansion of the energy. This approach is very practical for several reasons: it is flexible, in the sense that interactions are described in the form of polynomial entities that cover all

the possible interactions; it is fast, as evaluating polynomials in a computer is an extremely efficient process since it only involves sum and product operations; and it *approximates* remarkably well the function that is being Taylor-expanded. Further, the expansion is performed at the chemical bond region, and so the model captures the interatomic couplings close to this distance with great accuracy. As a consequence, the approximation is not valid for the description of bond creation or destruction. It should be underlined also that the model does not account for the electrons of the atoms; instead, the atom-atom interaction is modelled, and in the case of insulators, atoms are considered to hold a constant tensorial electrical charge that accounts for anisotropy. I assume throughout this Thesis that the function that is being Taylor-expanded is the energy as computed using DFT, ultimately allowing us to approximate first-principles calculations using polynomials (and for this reason they are called *second-principles*).

### 2.2.2 Description of the expansion point: the Reference Structure

These model potentials describe the energy of a crystal. The material is characterized by a periodically repeated cell containing atoms at specific locations - usually known as the unit cell. The choice of unit cell is arbitrary, but is always defined by the cell lattice parameters (corresponding to the cell basis vectors) and the coordinates of the atoms in the cell. I define in the following the Reference Structure (RS), which corresponds to point at which the energy is Taylor-expanded.

Assuming the crystal is embedded in a 3D space, one can generically describe the cell basis as the set of three vectors, that I will refer to as $(\mathbf{a}, \mathbf{b}, \mathbf{c})$. Let us define also $\boldsymbol{\tau}_\kappa$ as the coordinates of atom $\kappa$ within the cell, where the subindex runs for all the atoms in the cell. Since the cell is repeated periodically one can use integers $(l_1, l_2, l_3)$ to locate any cell in the space,

$$\mathbf{R}_{l_1 l_2 l_3} = l_1\mathbf{a} + l_2\mathbf{b} + l_3\mathbf{c} \tag{2.2.1}$$

In order to ease the notation, let us assume a particular ordering of the cells in space through a bijective mapping $l_1 l_2 l_3 \leftrightarrow l$, so that one can refer to the $l$th cell of the crystal as $\mathbf{R}_l$. It is now trivial to describe the coordinates of the atoms on any cell:

$$\mathbf{r}_{l\kappa} = \mathbf{R}_l + \boldsymbol{\tau}_\kappa. \tag{2.2.2}$$

Equation 2.2.2 defines the Reference Structure.

#### The variables of the model potential

The `SCALE-UP` model potentials use as variables the displacements of the atoms and the strains of the cell. They are a natural choice of variables since, if the RS is known, by using these variables it is possible describe any deformation of it in the following way:

$$\mathbf{r}_{l\kappa} = (\mathbf{Id}_3 + \mathbf{S}(\boldsymbol{\eta}))\,(\mathbf{R}_l + \boldsymbol{\tau}_\kappa) + \mathbf{u}_{l\kappa}, \tag{2.2.3}$$

where $u_{l\kappa\alpha}$ represents the displacement of atom $\kappa$ in cell $l$ along the direction $\alpha$ and $\mathbf{Id}_3$ is the $3\times 3$ identity matrix. Also, $\mathbf{S}$ represents the strain matrix,

$$\mathbf{S}(\boldsymbol{\eta}) = \begin{pmatrix} \eta_{11} & \eta_{12} & \eta_{13} \\ \eta_{21} & \eta_{22} & \eta_{23} \\ \eta_{31} & \eta_{32} & \eta_{33} \end{pmatrix}, \tag{2.2.4}$$

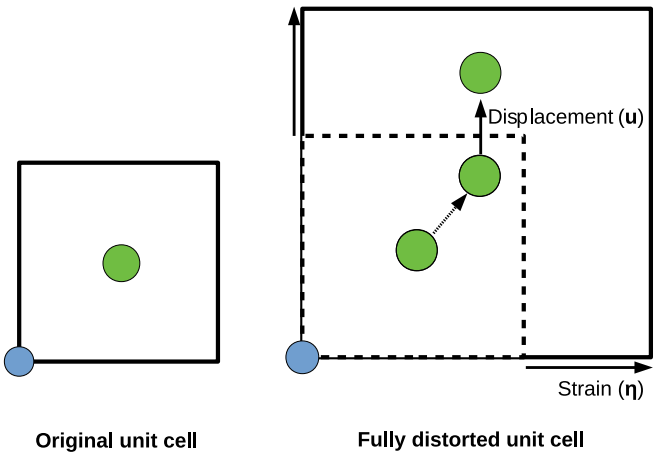


**Figure 2.5:** Sketch of how the variables describe a distortion of the cell. At the left, the original undistorted unit cell, with two atoms (blue and green). At the right the distortion is applied over the original cell (now grayed and depicted with a dashed cage). The central atom position (grayed-green atoms) is updated by the strain on the cell (dashed arrow), and a total displacement is applied to the atomic coordinates (solid-line arrow) to its final position. The blue atom position does not change in the example.

where $\eta_{ab}$ are the strain components.

In the scope of the model potentials I consider that the strain matrix is symmetrical, and so it is possible to use the standard Voigt notation defined through

$$\begin{aligned} \eta_1 &:= \eta_{11} \quad ; \quad \eta_4 := 2\eta_{23} = 2\eta_{32} \\ \eta_2 &:= \eta_{22} \quad ; \quad \eta_5 := 2\eta_{13} = 2\eta_{31} \\ \eta_3 &:= \eta_{33} \quad ; \quad \eta_6 := 2\eta_{12} = 2\eta_{21}. \end{aligned} \tag{2.2.5}$$

The description of the atomic position $\mathbf{r}_{l\kappa}$ in Eq. 2.2.3 is given in the following way (see Sketch 2.5 for more details). First, the cell deformation *with respect* the RS cell is accounted for via the strain variables. As the strain is applied both over the cell basis and the RS atomic positions, the fractional coordinates of the atoms are not affected in the process. Then, the atomic displacements are applied over the transformed cell basis and on the updated atomic positions, and hence they are absolute displacements of the atoms. It is clear that any form of periodic structure can be expressed in this way. Note that the expression in Eq. 2.2.3 introduces *independently* the variables of the distortion, namely, the strains and the displacements.

In the following I alleviate further the notation by also considering a bijective mapping $l\kappa \leftrightarrow i$, that for example, allows us to rewrite Eq. 2.2.3 into

$$\mathbf{r}_i = (\mathrm{Id}_3 + \mathbf{S}(\eta))(\mathbf{R}_i + \boldsymbol{\tau}_i) + \mathbf{u}_i. \tag{2.2.6}$$

### 2.2.3 The model potentials as a Taylor expansion of the energy

I describe in the following paragraphs how the energy is Taylor-expanded from the RS in terms of the displacements $\mathbf{u}_i$ and strains $\boldsymbol{\eta}$. The contributions can be generally written as

$$E(\mathbf{u},\boldsymbol{\eta}) = E_{\text{RS}} + E_{\text{p}}(\mathbf{u}) + E_{\text{s}}(\boldsymbol{\eta}) + E_{\text{sp}}(\mathbf{u},\boldsymbol{\eta}). \tag{2.2.7}$$

In this expression $E_{\text{RS}}$ the value RS potential energy (as computed using DFT, for example); $E_{\text{p}}$ (where "p" stands for "phonon") corresponds to the energy due to atomic displacements from the RS; $E_{\text{s}}$ (where "s" stands for "strain") is the elastic energy, the contribution of homogeneous cell deformations; and $E_{\text{sp}}$ (where "sp" stands for "strain-phonon") describes how the strains and displacements cooperate to define the Potential Energy Surface (PES).

Following several previous works[8, 56] the phonon part of the energy is treated so that it takes into account both the short-range interactions and the long-range electrostatic interactions of the material, and thus one can write

$$E_{\text{p}}(\mathbf{u}) = E_{\text{p}}^{sr}(\mathbf{u}) + E_{\text{p}}^{lr}(\mathbf{u}) \tag{2.2.8}$$

where "sr" stands for *short-range* and "lr" stands for *long-range*, referring to the Coulombic long-range electrostatic interactions. The electrostatic interaction is analogous to the formulation used in the Effective Hamiltonians described previously in this Chapter.

#### The atomic displacement contribution, $E_{\text{p}}$

For the $E_{\text{p}}$ short-range interactions the usual multivariate Taylor expression is used,

$$E_{\text{p}}^{\text{sr}}(\mathbf{u}) = \frac{1}{2!}\sum_{i\alpha j\beta} K^{(2)}_{i\alpha j\beta} u_{i\alpha} u_{j\beta} + \frac{1}{3!}\sum_{i\alpha j\beta k\gamma} K^{(3)}_{i\alpha j\beta k\gamma} u_{i\alpha} u_{j\beta} u_{k\gamma} + \dots. \tag{2.2.9}$$

Here, $K$ stands for the coefficient of the polynomial term of the expansion and the superindex indicates the order of the term. The coefficients of the terms correspond to the $n$th derivatives of the energy with respect the displacements at the RS (i.e., $\mathbf{u} = 0$, $\boldsymbol{\eta} = 0$), and hence

$$K^{(n)} = \left.\frac{\partial^n E_{\text{eff}}}{\partial u_{i\alpha}\partial u_{j\beta}\dots}\right|_{\text{RS}}. \tag{2.2.10}$$

The expansion starts at second order in the derivatives. The reason is that the RS will be usually a configuration that is a critical point of the PES, and thus the first derivatives are necessarily zero. This also affects in the same way the elastic part of the energy, which as I show below in the text, also has the first terms at the harmonic order. It is also worth mentioning that, unless the RS is a stable point of the PES with strong harmonic character, it will always be necessary to expand the energy up to at least fourth order in order to get models in which the energy is bounded from below and displays an absolute minimum of the energy, corresponding to the ground state of the material.

#### The Acoustic Sum Rule

The coefficients of Eq. 2.2.9 have to satisfy, at all orders, the so-called *acoustic sum rules* (ASRs). These rules preserves translational symmetry, which means that rigid translation of the material

does not have an impact on the energy. Due to the spatial truncation on the short-range interactions a formulation presented as in Eq. 2.2.9 would not fulfill this rule (truncations of the model will be discussed further in the text).

The derivation of the rule is quite simple if one considers a rigid displacement $u_{i\alpha} = \delta_\alpha$, for all $i$. Then, the energy at the RS and at the rigid displacement should be equal, which means

$$E_0 = E_0 + \frac{1}{2!}\sum_{i\alpha j\beta} K^{(2)}_{i\alpha j\beta}\delta_\alpha\delta_\beta \Rightarrow \sum_{i\alpha j\beta} K^{(2)}_{i\alpha j\beta}\delta_\alpha\delta_\beta = 0 \tag{2.2.11}$$

This sum can be rewritten now

$$0 = \sum_{i\alpha j\beta} K^{(2)}_{i\alpha j\beta}\delta_\alpha\delta_\beta = \sum_{\alpha l\beta} K^{(2)}_{0\alpha l\beta}\delta_\alpha\delta_\beta = \sum_{\alpha\beta}\left(\sum_l K^{(2)}_{0\alpha l\beta}\right)\delta_\alpha\delta_\beta \Rightarrow \sum_l K^{(2)}_{0\alpha l\beta} = 0 \tag{2.2.12}$$

Only the harmonic part of the energy is written as an example; however, the equation holds individually for every order in the expansion. Note that such a condition over the coefficients means, in fact, that there are dependencies between them. For example, one could consider from Eq. 2.2.11 the solution

$$K^{(2)}_{i\alpha j\beta} = -\sum_{k\neq i} K^{(2)}_{k\alpha j\beta}, \tag{2.2.13}$$

and introduce this into Eq. 2.2.9 (at the harmonic order). The resulting polynomial has then coefficients associated to the terms expressed in *differences* of displacements. This rule is however extremely challenging to express in higher orders of the energy derivatives. Instead of doing so, in SCALE-UP model potentials the formulation of the short-range interactions is written as

$$E^{\mathrm{sr}}_{\mathrm{p}}(\mathbf{u}) = E_0 + \frac{1}{2!}\sum_{\substack{ijkh\\ \alpha\beta}} \tilde{K}^{(2)}_{ij\alpha kh\beta}\left(u_{i\alpha} - u_{j\alpha}\right)\left(u_{k\beta} - u_{h\beta}\right) + \dots. \tag{2.2.14}$$

It is clear that any rigid displacement will be automatically canceled due to the formulation in terms of displacement differences. However, in doing so one has to address several considerations as on how it is related to the original Taylor expansion.

First, obtaining Eq. 2.2.14 from Eq. 2.2.9 requires transformations of the form described in Eq. 2.2.13 (to all orders), as well as the identities that may arise from the fact that polynomial's partial derivatives are commutative - thus additional conditions arise. As it is clear, this is an arbitrary choice, and hence it is not unique. In contrast, the reverse path is trivial. One needs only to expand the terms in Eq. 2.2.14 to recover Eq. 2.2.9.

Second, the original expression Eq. 2.2.9 is a polynomial in terms of the displacements $\{\mathbf{u}_i\}$, which are a complete basis. It is clear that the set of variables $\{(u_{i\alpha} - u_{j\alpha})\}$ is a linear combination of the original basis. In that sense, a model expressed in terms of differences of displacements can have redundancy of terms; however, although not being basis, it is a complete set of interactions.

Finally, writing the Taylor expansion in form of displacement differences allows to interpret the individual terms as spring-like interactions. Even though the new form of the coefficients is different from that of the force-constants of the material (i.e., the derivatives of the energy), it is in fact an interesting way of treating the atoms in the crystal lattice, allowing us to interpret the

interaction between the individual atoms on the system. Hence a term like $\tilde{K}^{(2)}_{ij\alpha kh\beta}\,(u_{i\alpha}-u_{j\alpha})^2$ provides information on whether the atoms are prone to move or not from their reference position by just looking at the sign of the coefficient, how unstable it is; adding anharmonic terms allows also to interpret if the atoms would tend to have a displaced stable distance, etc.

### The cell strain contribution, $E_{\mathrm{s}}$

Similarily to the initial development of $E_{\mathrm{p}}$, the energy can be expanded in terms of the strain as a usual Taylor expansion:

$$E_{\mathrm{s}}(\boldsymbol{\eta}) = \frac{N}{2!}\sum_{ab} C^{(2)}_{ab}\eta_a\eta_b + \frac{N}{3!}\sum_{abc} C^{(3)}_{abc}\eta_a\eta_b\eta_c\ldots, \tag{2.2.15}$$

where the coefficients $C^{(n)}$ correspond to the different orders of the expanded elastic coefficients - which again can be written as the derivatives of the energy with respect to the strains of the cell. Note the addition of the cummulative factor $N$, which accounts for the number of unit cells in the supercell.

The elastic energy contribution used in the model potentials will be usually considered up to a harmonic order, unless of course, anharmonic orders contribute substantially. It would also be necessary to add higher orders in the expansion if the RS would have an elastic instability, as then at least a fourth order polynomial would be required for the energy to have a minimum.

### The coupling between phonons and strains, $E_{\mathbf{sp}}$

As for any multivariate Taylor expansion it is relevant to define properly the coupling between all its variables. In this case the model contains two families of variables, the displacements and the strains. The strain-phonon coupling terms allow to fit the interplay between them, improving the ability of the model at reproducing the complete PES of the material.

The coupling between the phonons and the strains can be written as

$$E_{\mathrm{sp}}(\mathbf{u},\boldsymbol{\eta}) = \frac{1}{2!}\sum_{\substack{a\\ i\alpha}}\Delta^{(1,1)}_{ai\alpha}\eta_a u_{i\alpha} + \frac{1}{3!}\sum_{\substack{a\\ i\alpha j\beta}}\Delta^{(1,2)}_{ai\alpha j\beta}\eta_a u_{i\alpha}u_{j\beta} + \frac{1}{3!}\sum_{\substack{ab\\ i\alpha}}\Delta^{(2,1)}_{abi\alpha}\eta_a\eta_b u_{i\alpha}\ldots. \tag{2.2.16}$$

Here $\Delta^{(n,m)}$ define the coefficient of the term, and the superindex indicates the order of the expansion where $n$ refers to the order in the strains and $m$ refers to the order in the displacements. As it was the case of the $E_{\mathrm{p}}$, the expression can be adapted to follow the ASRs using exactly the same argument. In this case, the Taylor expansion transforms into

$$\begin{aligned} E_{\mathrm{sp}}(\mathbf{u},\boldsymbol{\eta}) = \frac{1}{2!}\sum_{\substack{a\\ ij\alpha}}\tilde{\Delta}^{(1,1)}_{aij\alpha}\eta_a(u_{i\alpha}-u_{j\alpha}) + \frac{1}{3!}\sum_{\substack{a\\ ij\alpha kh\beta}}\Delta^{(1,2)}_{aij\alpha kh\beta}\eta_a(u_{i\alpha}-u_{j\alpha})(u_{k\beta}-u_{h\beta}) + \\ \frac{1}{3!}\sum_{\substack{ab\\ ij\alpha}}\Delta^{(2,1)}_{abij\alpha}\eta_a\eta_b(u_{i\alpha}-u_{j\beta})\ldots. \end{aligned} \tag{2.2.17}$$

It is again clear that such formulation respects ASR explicitly. Also, it completes the physical picture. For example, it follows from Eq. 2.2.17 that now derivatives of the energy with respect

the displacements have explicit dependencies with the strain variables, and viceversa, providing the model with a description of how the elastic properties may change with the displacement of the atoms, or how the strain can induce in the atomic positions forces that favor particular distortions of the crystal.

### Symmetry adapted terms

The model potential is formulated as a polynomial in terms of displacements of the atoms in the crystal and the strains of the particular RS cell chosen. The RS will be chosen in the framework of the SCALE-UP model potentials as a structure with a particular symmetry associated. Due to the symmetry of the crystal there are terms representing symmetry invariants (with respect the symmetry of the RS). In practice, this means that due to symmetry terms can be identified as equivalent, and hence, have the same coefficients. This applies to all the types of terms described previously. For example, with a 3-axis, and for a cubic cell the diagonal terms of the strain tensor yield

$$\frac{N}{2}\left(C_{11}\eta_1^2 + C_{22}\eta_2^2 + C_{33}\eta_3^2\right) = \frac{NC_{11}}{2}\left(\eta_1^2 + \eta_2^2 + \eta_3^2\right), \tag{2.2.18}$$

since the symmetry operation translates into $C_{11} = C_{22} = C_{33}$. The *symmetry adapted term* (SAT) are defined as the grouped terms that have the same coefficient due to symmetry, and one selects any of the terms as the representative of the SAT. Then, for example, the term $C_{11}\eta_1^2$ is a representative of the SAT described in Eq. 2.2.18.

Symmetry considerations become relevant in practice, where one has a limited amount of resources to describe a polynomial entirely. They effectively reduce the amount of independent coefficients of the model, which are the parameters of it. Therefore, it follows that the higher the symmetry for the RS, the simpler the Taylor expansion will become.

### Models for insulators: the long-range electrostatic interaction

Electrostatics become very relevant when modeling specific materials like semi-conductors or insulators. In such cases it is sensible to describe the model in terms of short-range and long-range interactions - as Coulombic interactions are present and have an infinite range.

The Coulombic interactions have origin on the interaction between the dipoles that may appear in the material as a consequence of distortions of the ions in the crystal. By assigning charges to the ions by means of the Born effective-charges tensor $Z^*_{i\beta\alpha}$, one can write the dipoles as

$$d_{i\alpha} = \sum_{\beta} Z^*_{i\beta\alpha} u_{i\beta}. \tag{2.2.19}$$

In the framework of the `SCALE-UP` model potentials the contribution of the electrical dipoles is considered only at the harmonic order for the $E_p$ energy contribution. The approach by Gonze and Lee [56] allows for a correct description of the electrostatics of the material accounting for the so-called LO-TO splitting, the discontinuity of the phonon bands that appear at $\mathbf{q} = 0$. These couplings are described by

$$K^{(2),lr}_{i\alpha j\beta} = \sum_{\gamma\delta} Z^*_{i\alpha\gamma} Z^*_{j\alpha\delta} \left( \frac{(\epsilon_\infty^{-1})_{\gamma\delta}}{D^3} - \frac{3\Delta_\gamma \Delta_\delta}{D^5} \right) \det \epsilon_\infty{}^{-1/2} \tag{2.2.20}$$

where

$$\begin{aligned} \Delta_\alpha &= \sum_\beta (\epsilon_\infty^{-1})_{\alpha\beta} \Delta r_\beta, \\ D &= \sqrt{\boldsymbol{\Delta} \cdot \Delta r}, \\ \Delta \mathbf{r} &= \mathbf{R}_j + \boldsymbol{\tau}_j - \mathbf{R}_i - \boldsymbol{\tau}_i. \end{aligned} \tag{2.2.21}$$

Here, $\epsilon_\infty$ corresponds to the high-frequency dielectric permitivity tensor. This equation is equivalent to Eq. 2.1.10 in the formulation of the Effective Hamiltonians.

### Truncation of the model

Although the formulation above is general and the energy is presented as a Taylor series in practice the interactions are effectively truncated in three different ways. First, the model is spatially truncated by the choice of the interactions included and the size of the supercell. Second, the model is truncated in the number of *bodies* of the terms included. Bodies refer to the different atom labels included in a single term, and one can limit the complexity of the terms by choosing terms up to a certain number of bodies. Third, the models are truncated in the order of the expansion, as the Taylor expansion must be finite. Assuming that the RS is a critical point of the PES and is not a stable point, it is required to expand at least up to fourth-order for the model to have a well-defined absolute minimum of the energy, which physically represents the ground state of the material modeled.

### Models fitted to DFT

In Ref. [27] the authors devised a strategy to fit the model potentials to DFT calculations by using a set of three *Goal Functions*. Goal functions are functionals of the parameters for which the minimum with respect to the parameters is the set of fitted parameters of the model. They also performed several DFT calculations at critical points of the potential energy surface to use as the data to be fit.

The first Goal Function they considered was the mean-squared error in energy between the model and the DFT calculations. Once the energies are fitted, they proposed a second Goal Function based on the derivatives of the energy, aiming at altering as less as possible the result of the first Goal Function minimization. In this way, and since the authors were fitting the derivatives for structures for which $\nabla E = 0$, they ensured that the location of the critical points of the PES was the correct. Finally, they added a third Goal Function consisting on the error on the second derivatives of the energy. More precisely, they projected the DFT-calculated eigenvectors of the Hessian Matrix into the model's calculated Hessian Matrix. In the ideal case, this solves the eigenvalue problem and has as a result the product of the eigenvalue and the eigenvector. Hence, the Goal Function was built by mesuring the difference between this projection and the solution of the eigenvalue problem as computed with DFT.

This scheme is efficient and was sufficient for the authors to produce a model for $PbTiO_3$ and $SrTiO_3$ yielding a very good accuracy with respect to DFT. It is, however, not an automatic or flexible scheme, in the sense that it requires knowledge of the specific phases that one wants to fit the model to. In contrast, in Section 3 I present a more general approach to the construction of SCALE-UP model potentials.

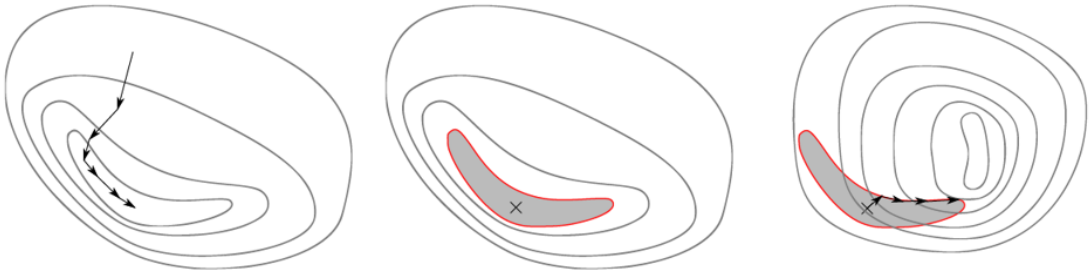

**Figure 2.6:** Sketch of the three Goal Function minimization scheme. First, the energy is minimized to be under a certain level curve (left). Then, the position of the extrema of the PES is located within the level curve (center). Finally, the correct curvature of the critical point is found (right), as described in the text. Figure courtesy of J. C. Wojdeł.

### 2.2.4 Calculation of forces and stresses

It is also convenient to comment in detail on the calculation of the lattice-dynamical quantities from the model. The forces on the atoms will be simply given by

$$f_i = -\left.\frac{\partial E}{\partial u_i}\right|_{(\mathbf{u},\boldsymbol{\eta})} \tag{2.2.22}$$

for a particular configuration of atomic displacements and strains $(\mathbf{u}, \boldsymbol{\eta})$. The expression for the stress calculation is more delicate: it requires to compute the derivative of the energy with respect the strains under the condition that the atoms *fractional* coordinates do not change.

Let $\mathbf{A}$ be the $3 \times 3$ matrix constructed by joining the vectors that define the elemental unit cell of the reference structure in columns; then, the relative position $\mathbf{r}'_{l\kappa}$ of an atom is defined by

$$\mathbf{r}'_{l\kappa} = [(\mathrm{Id}_3 + \boldsymbol{\eta})\mathbf{A}]^{-1}\mathbf{r}_{l\kappa}. \tag{2.2.23}$$

However, because of how the positions of the atoms in the formulation of the model potentials are defined (Eq. 2.2.6) the change in strain does not affect the displacement variable. It follows that if the displacements are not zero the derivative of the energy with respect the strains does not preserve the relative positions of the atoms, as the displacement of the atoms is independent of this calculation. In order to calculate properly the stress one has to take this into account and apply the adequate derivative chain rule. For now let us write the calculation of the stress as

$$\sigma_a = -\left.\frac{\partial' E}{\partial' \eta_a}\right|_{(\mathbf{u},\boldsymbol{\eta})} \tag{2.2.24}$$

The symbol $\partial'$ is used to indicate that this derivative occurs under the constraint that the relative positions $\mathbf{r}'_{l\kappa}$ of the (however *displaced*) atoms are kept constant. The constraint takes a form of a dependency of the displacements on the strains. I will develop this expression by using an appropriate chain rule over this dependency in the following paragraphs.
To compute the stress corresponding to a configuration defined by $(\{\mathbf{u}_{l\kappa}\}, \boldsymbol{\eta})$, one has to consider a perturbed structure $(\boldsymbol{\eta} + \delta\boldsymbol{\eta}, \{\mathbf{u}_{l\kappa} + \delta\mathbf{u}_{l\kappa}\})$ that is constructed by imposing an infinitessimal deformation $\delta\boldsymbol{\eta}$ and whose atoms are at the same relative positions as those of the state of interest. Hence, the displacements $\delta\mathbf{u}_{l\kappa}$ have to be chosen so that

$$\begin{aligned}[(\mathrm{Id}_3 + \boldsymbol{\eta})\,\mathbf{A})]^{-1}\,[(\mathrm{Id}_3 + \boldsymbol{\eta})\,(\mathbf{R}_l + \boldsymbol{\tau}_\kappa) + \mathbf{u}_{l\kappa}] = \\ [(\mathrm{Id}_3 + \boldsymbol{\eta} + \delta\boldsymbol{\eta})\,\mathbf{A}]^{-1}\,[(\mathrm{Id}_3 + \boldsymbol{\eta} + \delta\boldsymbol{\eta})\,(\mathbf{R}_l + \boldsymbol{\tau}_\kappa) + \mathbf{u}_{l\kappa} + \delta\mathbf{u}_{l\kappa}]\end{aligned} \tag{2.2.25}$$

which reduces to

$$\delta \mathbf{u}_{l\kappa} = \delta \boldsymbol{\eta} \left( \mathrm{Id}_3 + \boldsymbol{\eta} \right)^{-1} \mathbf{u}_{l\kappa}. \tag{2.2.26}$$

Hence, the stress can be obtained from the chain rule

$$\sigma_a = -\frac{\partial' E}{\partial' \eta_a} = -\frac{\partial E}{\partial \eta_a} - \sum_{l\kappa\alpha} \frac{\partial E}{\partial u_{l\kappa\alpha}} \frac{\partial u_{l\kappa\alpha}}{\partial \eta_a} \tag{2.2.27}$$

where $\frac{\partial u_{l\kappa\alpha}}{\partial \eta_a}$ is obtained from Eq. 2.2.26.

# Chapter 3

# Automatic model generation for SCALE-UP

In Chapter 2 I have introduced the formalism behind the second-principles model potentials within the framework of SCALE-UP. Here in Chapter 3 I describe a method to construct SCALE-UP model potentials. In Section 3.1 I formally describe the fitting process developed in my research for this particular case of model potentials. I present an application of the method in Section 3.2 for Strontium Titanate, for which I demonstrate the advantages of the fitting process and describe an example of research application for the study of the material's phase transition. In Annex A I briefly discuss some implementation details and include a sketch of the whole model construction process in the form of a structured summary. This Chapter is based on the article published on 2017 in Physical Review B [57].

## 3.1 Formalism

I adopt in the following mathematical development the formalism introduced in Chapter 2.2 for the SCALE-UP model potentials.

### 3.1.1 The fitting method

The procedure to calculate the parameters that fit a model to a particular set of data is a complex problem that can be approached in several ways [58], depending on the mathematical properties of the model. The method that will be described in this Section is based on a standard discrete mathematics solution to a general optimization problem. In this method one defines a positively defined function, called *Goal Function* (GF), that measures a particular quantity relevant in the fitting process that allows to compare the model with the data that is used to fit it. Then the parameters that fit the model to the data are found by minimizing the GF. The data intrinsically defines the upper limit of the model's accuracy, and is generically referred to as the *Training Set* (TS).

In the general mathematical approach the GF will be usally a multivariate function with non-linear dependency with respect to the parameters, and because of that, the minimization problem may turn into a hard task that can require advanced [59–61] and costly numerical methods to solve.

Nonetheless, the SCALE-UP model potentials are *linear* with respect to the parameters, and as I show in this Section, this property allows to find an analyitical solution to the optimization problem, turning the process of model fitting into a fast and easy calculation.

### The Goal Function

Let us first alleviate slightly the notation by revisiting the description of the model potential (Section 2.2) using a simpler parametric formulation. One can write

$$E[\Theta_p](\mathbf{u}, \boldsymbol{\eta}) = \sum_{\lambda} \theta_\lambda t_\lambda(\mathbf{u}, \boldsymbol{\eta}) + E^{\text{fixed}}(\mathbf{u}, \boldsymbol{\eta}) \tag{3.1.1}$$

where $\Theta_p := \{\theta_1, \ldots, \theta_p\}$ is the set of parameters of the model and $\mathcal{T}_p := \{t_1, \ldots, t_p\}$ is the set of the corresponding polynomial terms, which depend on the displacements $\mathbf{u} := \{\mathbf{u}_i\}$ and strains $\boldsymbol{\eta}$. The polynomial terms belong to the family of short-range interaction terms, both in the $E_\text{p}$ and $E_\text{sp}$ energy contributions in the model. The energy term $E^{\text{fixed}}$ contains all the interactions that are not involved in the fitting process: these can be terms for which the parameter is considered to be fixed, or other known energy contributions. For example, this energy contributions can be due to the elastic energy or long-range dipole-dipole interactions. The parameters of these contributions can be straight-forwardly calculated using DFT.

Now let us define the goal function. A GF is a functional that measures a meaningful quantity allowing to fit the model to the TS data. I have chosen the functional to represent the mean square error in forces and stresses between the model and the TS. The strength of the functional is that it is parametrized by the same parameters that the model has, so by optimizing the value of the parameters to reduce the error in forces and stresses one is effectively fitting the model. I chose to define the GF as

$$G[\Theta_p, \text{TS}] = \frac{1}{M_1} \sum_{s\tau} \left( f_\tau^{\text{TS}}(s) - f_\tau[\Theta_p](s) \right)^2 + \frac{1}{M_2} \sum_{sa} \Omega^2(s) \left( \sigma_a^{TS}(s) - \sigma_a[\Theta_p](s) \right)^2 . \tag{3.1.2}$$

In this expression $s \in \text{TS}$ labels the structures in the training set, and $f_\tau^{\text{TS}}(s), \sigma_a^{\text{TS}}(s)$ are the corresponding forces and stresses in the TS. I indicate the forces and stresses as computed using the model by $f_\tau[\theta_p]$ and $\sigma_a[\theta_p]$, where I make explicit their dependency with the parameters of the model. I have used the bijective mapping $i\alpha \leftrightarrow \tau$ to ease the notation. The values $M_1$ and $M_2$ are the normalization factors computed as the cardinal of the elements of the corresponding sums. Finally, $\Omega(s)$ is a factor that was proposed by Sheppard *et al.* [62] that allows to weight properly forces and stresses in the same expression - in their case, applied to the so-called Nudged Elastic Band method for the study of minimum energy paths using DFT. This factor is defined through

$$\Omega(s) = \left( V(s)\sqrt{N} \right)^{-1/3} , \tag{3.1.3}$$

where $N$ is the number of atoms in the simulation cell and $V(s)$ is the cell volume for configuration $s$. The forces and stresses from the model potentials are computed as described in the Section 2.2.4.

### The extrema of the GF

The equation 3.1.1 is a convenient way to study the extrema of the GF as formulated in 3.1.2. The reason is that it provides with a very compact expression to describe the dependency of the

model potential on the parameters. It is possible to see how the forces and stresses depend on those parameters, and ultimately, how the GF can be written explicitely in terms of them.

First, it is now quite simple to write the expressions for the contributions to the forces and stresses of each term in a general way. Let us define the SAT derivatives with respect to the atomic displacements and strains for a particular configuration of the training set $s$ by

$$\bar{f}_{\lambda\tau}(s) = -\left.\frac{\partial t_\lambda(\mathbf{u},\boldsymbol{\eta})}{\partial u_\tau}\right|_s \tag{3.1.4}$$

and

$$\bar{\sigma}_{\lambda a}(s) = -\left.\frac{\partial' t_\lambda(\mathbf{u},\boldsymbol{\eta})}{\partial' \eta_a}\right|_s . \tag{3.1.5}$$

The primed derivatives in equation 3.1.5 indicate that the chain rule discussed in Section 2.2.4 is applied. Using these definitions one can now compute the total force and stress for the $s$ configuration by summing over all terms as

$$f_\tau(s) = \sum_\lambda \theta_\lambda \bar{f}_{\lambda\tau}(s) + f_\tau^{\text{fixed}}(s) \tag{3.1.6}$$

and

$$\sigma_a(s) = \sum_\lambda \theta_\lambda \bar{\sigma}_{\lambda a}(s) + \sigma_a^{\text{fixed}}(s), \tag{3.1.7}$$

where

$$f_\tau^{\text{fixed}}(s) := \left.\frac{\partial E^{\text{fixed}}}{\partial u_\tau}\right|_s \quad ; \quad \sigma_a^{\text{fixed}}(s) := \left.\frac{\partial' E^{\text{fixed}}}{\partial' \eta_a}\right|_s . \tag{3.1.8}$$

It is possible now to rewrite the GF expression 3.1.2 into

$$\begin{aligned} G[\Theta_p, \text{TS}] = \frac{1}{M_1}\sum_{s\tau}\left(f_\tau^{\text{TS}}(s) - \sum_\lambda \theta_\lambda \bar{f}_{\lambda\tau}(s) - f_\tau^{\text{fixed}}(s)\right)^2 \\ + \frac{1}{M_2}\sum_{sa}\Omega^2(s)\left(\sigma_a^{\text{TS}}(s) - \sum_\lambda \theta_\lambda \bar{\sigma}_{\lambda a}(s) - \sigma_a^{\text{fixed}}(s)\right)^2 , \end{aligned} \tag{3.1.9}$$

where the dependency of the GF with the parameters is made explicit. This exercise now turns into a basic academic development in which one uses the properties of differential calculus to study the extrema of a function, where the variables of the problem are the parameters $\theta_\lambda \in \Theta_p$. The general equations to solve to find its critical points are

$$\frac{\partial G[\Theta_p, \text{TS}]}{\partial \theta_\mu} = 0 \;\forall\; \mu \in \{1, \ldots, p\}. \tag{3.1.10}$$

Then, using Eq. 2.2.4 one can write:

$$\begin{aligned} 0 = \frac{\partial G[\Theta_p, \text{TS}]}{\partial \theta_\mu} = \frac{2}{M_1}\sum_{s\tau}\left(f^{\text{TS}} - \sum_\lambda \theta_\lambda \bar{f}_{\lambda\tau}(s) - f_\tau^{\text{fixed}}(s)\right)\bar{f}_{\mu\tau}(s) + \\ \frac{2}{M_2}\sum_{sa}\Omega^2(s)\left(\sigma_a^{\text{TS}}(s) - \sum_\lambda \theta_\lambda \bar{\sigma}_{\lambda a}(s) - \sigma_a^{\text{fixed}}(s)\right)\bar{\sigma}_{\mu a}(s). \end{aligned} \tag{3.1.11}$$

It is possible to isolate the $\theta_\lambda$ factors by using the commutative property of finite sums, leading to

$$\sum_\lambda \left[ \sum_s \left( \frac{1}{M_1} \sum_\tau \bar{f}_{\mu\tau}(s)\bar{f}_{\lambda\tau}(s) + \frac{1}{M_2} \sum_a \Omega^2(s)\bar{\sigma}_{\mu a}(s)\bar{\sigma}_{\lambda a}(s) \right) \right] \theta_\lambda = \sum_s \left\{ \frac{1}{M_1} \sum_\tau \left[ f_\tau^{\mathrm{TS}}(s) - f_\tau^{\mathrm{fixed}}(s) \right] \bar{f}_{\mu\tau}(s) + \frac{1}{M_2} \sum_a \Omega^2(s) \left[ \sigma_a^{\mathrm{TS}}(s) - \sigma_a^{\mathrm{fixed}}(s) \right] \bar{\sigma}_{\mu a}(s) \right\}. \tag{3.1.12}$$

By defining now

$$\Delta_{\mu\lambda}(s) := \sum_s \left( \frac{1}{M_1} \sum_\tau \bar{f}_{\mu\tau}(s)\bar{f}_{\lambda\tau}(s) + \frac{1}{M_2} \sum_a \Omega^2(s)\bar{\sigma}_{\mu a}(s)\bar{\sigma}_{\lambda a}(s) \right) \tag{3.1.13}$$

and

$$\Gamma_\mu(s) := \sum_s \left\{ \frac{1}{M_1} \sum_\tau \left[ f_\tau^{\mathrm{TS}}(s) - f_\tau^{\mathrm{fixed}}(s) \right] \bar{f}_{\mu\tau}(s) + \frac{1}{M_2} \sum_a \Omega^2(s) \left[ \sigma_a^{\mathrm{TS}}(s) - \sigma_a^{\mathrm{fixed}}(s) \right] \bar{\sigma}_{\mu a}(s) \right\} \tag{3.1.14}$$

one can rewrite 3.1.12 into

$$\sum_\lambda \Delta_{\mu\lambda}(s)\theta_\lambda = \Gamma_\mu(s), \tag{3.1.15}$$

The form of this last equation is very well known to anyone familiar with linear algebra: it constitutes a system of linear equations with $\theta_\lambda$ as variables, to which the solution is the extrema of the function $G[\Theta_p, \mathrm{TS}]$. Additionally, the solution of the system in Eq. 3.1.15 is the set of parameter values that fit the model to the TS.

Now that the analytical extremum of the GF is found it is possible to study its stability and character. It is important to note that $G[\Theta_p, \mathrm{TS}] \geq 0$, since it is a sum of parabolas with the positive parameters $1/M1$ and $1/M2$. The lower bound ($G = 0$) represents a point in which the forces and stresses computed using the model match perfectly those of the training set.

A way to show that the solution of equation 3.1.15 is stable is to study the Hessian matrix of the GF at the extrema of the function. By taking second derivatives on equation 3.1.9 one may write

$$H_{\mu\lambda}(s) := \frac{\partial^2 G[\Theta_p, \mathrm{TS}]}{\partial\theta_\lambda \partial\theta_\mu} = \frac{2}{M_1} \sum_{s\tau} \bar{f}_{\lambda\tau}(s)\bar{f}_{\mu\tau}(s) + \frac{2}{M_2} \sum_{sa} \Omega^2(s)\bar{\sigma}_{\lambda a}(s)\bar{\sigma}_{\mu a}(s). \tag{3.1.16}$$

The eigenvalue problem associated to this equation is

$$H_{\lambda\mu} v_\lambda^i = c^i v_\lambda^i, \tag{3.1.17}$$

where $\mathbf{v}^i$ is the $i$th normalized eigenvector and $c^i$ the corresponding eigenvalue. This leads to

$$\begin{aligned}
c^i &= \sum_{\lambda\mu} v^i_\lambda H_{\lambda\nu} v^i_\nu \\
&= \sum_{\lambda\mu}\sum_s \left[\frac{2}{M_1}\sum_\tau v^i_\lambda \bar{f}_{\lambda\tau}(s)\bar{f}_{\mu\tau}(s)v^i_\mu + \frac{2}{M_2}\Omega^2(s)\sum_a v^i_\lambda \bar{\sigma}_{\lambda a}(s)\bar{\sigma}_{\mu a}(s)v^i_\mu\right] \\
&= \sum_s \left[\frac{2}{M_1}\sum_\tau\sum_\lambda\sum_\mu v^i_\lambda \bar{f}_{\lambda\tau}(s)\bar{f}_{\mu\tau}(s)v^i_\mu + \frac{2}{M_2}\Omega^2(s)\sum_a\sum_\lambda\sum_\mu v^i_\lambda \bar{\sigma}_{\lambda a}(s)\bar{\sigma}_{\mu a}(s)v^i_\mu\right] \\
&= \sum_s \left[\frac{2}{M_1}\sum_\tau \left(\sum_\lambda v^i_\lambda \bar{f}_{\lambda\tau}(s)\right)\left(\sum_\mu \bar{f}_{\mu\tau}(s)v^i_\mu\right) + \right. \\
&\qquad\qquad \left. \frac{2}{M_2}\Omega^2(s)\sum_a \left(\sum_\lambda v^i_\lambda \bar{\sigma}_{\lambda a}(s)\right)\left(\sum_\mu \bar{\sigma}_{\mu a}(s)v^i_\mu\right)\right] \\
&= \sum_s \left[\frac{2}{M_1}\sum_\tau \left(\sum_\lambda v^i_\lambda \bar{f}_{\lambda\tau}(s)\right)^2 + \frac{2}{M_2}\Omega^2(s)\sum_a \left(\sum_\lambda v^i_\lambda \bar{\sigma}_{\lambda a}(s)\right)^2\right] \geq 0.
\end{aligned} \tag{3.1.18}$$

This result contains all the information about the character of the extrema of the GF. First, the eigenvalues $c^i$ have to be non-negative. The consequence of this is that the point representing the extrema of the function is not a maximum (which would require $c^i < 0\ \forall i$) nor a saddle point (which would require positive and negative eigenvalues), and thus, it has to be a minimum.

The topology of the solution is however slightly more intrincate. On one hand, the eigenvalues of the matrix can be strictly positive. Then the solution is a minimum of the GF (more precisely the global minimum since it is a function with exactly one extrema), and is then the solution representing the parameters that fit the model to the data. On the other hand, if at least one of the eigenvalues $c^i$ *is zero*, then the solution is a collection of points, all of them describing equivalent minima. As for any linear system of equations, it follows that the solution is not unique and one can find a linear dependency between parameters leading to the equivalent solutions.

It is interesting to discuss about the origin of linear dependencies in this particular system of equations. If there is a subset of $\theta_\lambda$ which are linearly dependent it means that the associated terms $t_\lambda$ are in fact linearily dependent. But how can this be?

Let us first introduce a simplified notation that will be useful to discuss short-range interactions. In this Manuscript I will describe the displacement variables $u_{i\alpha}$ as $i_\alpha$. For example, for a second order interaction along the $x$ direction between the $A$ and O atoms I will write the interaction as

$$(A_x - O_x)^2. \tag{3.1.19}$$

Now, the distinct character of the terms depends on the completeness of the training set. One can write a simple example:

$$t_1 = (A_x - B_x)^2, \quad t_2 = (A_x - C_x)^2. \tag{3.1.20}$$

In this example $A, B$ and $C$ represent three fictitious atoms. Then, $t_1$ is the interaction associated to the atomic displacements of $A$ and $B$ along the $x$ direction, and $t_2$ represents the interaction between $A$ and $C$ atoms displacing along the $x$ direction. Let us imagine now that the TS contains

only information related to the displacement of the fictitious atom $A$. Then, under the process of fitting described previously, it is clear that $t_1$ and $t_2$ are indistinguishable, and so in appearence, linearily dependent due to the lack of completeness of the TS.

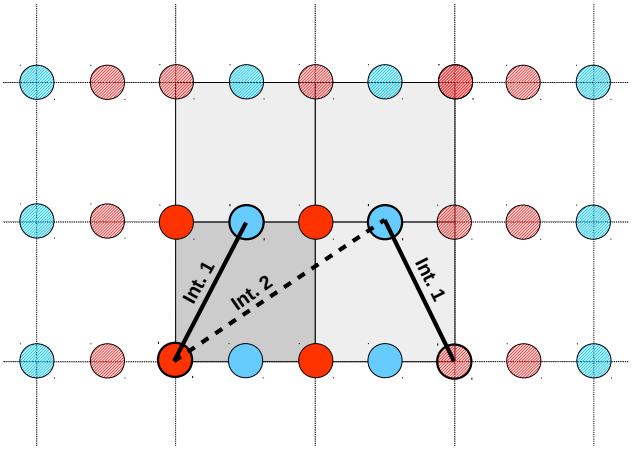


**Figure 3.1:** Sketch representation of a finite-size effect that could lead to an apparent linear dependency between terms that are actually independent, but the size of the cell does not allow to distinguish one from the other.

A second source for linear dependencies is related to the periodic boundary conditions used when modelling crystals, and can be illustrated in a very simple example as in Figure 3.1. Periodic boundary conditions define in practice a spatial cutoff distance for the interactions. In the 2D example, interactions are allowed up to a $2 \times 2$ repetition of the unit cell. However, due to the periodic boundary conditions, Interactions 1 and 2 in the sketch become equivalent, even though for an infinite crystal they would be different. Therefore, if one would attempt to evaluate the solution of Eq. 3.1.15 using a TS obtained for a $2 \times 2$ repetition of the unit cell the two interactions would appear as linearily dependent.

In practice, this are two situations that are easy to deal with. In the first case it is enough to increase the complexity of the TS by adding additional data. As for the second source of linear dependencies, since the terms are redundant it is enough to retain the shortest interaction term and disregard the long-distance one of the terms that become linearily dependent. From a technical point of view this is in fact easy to detect, as the matrix representing the left-hand-side of the system of equations in Eq. 3.1.15 becomes singular whenever linear dependencies exist.

### 3.1.2 Iterative model construction

The model fitting constitutes a critical but small part of model design itself. I discuss now an optimal way of automatically finding which are the most relevant interactions the model potentials have to have in order to reproduce optimally the training set.

The model potentials within the `SCALE-UP` framework are polynomials, written in a basis of differences of displacements instead of the usual Taylor expansion representation. The terms of the polynomial represent couplings between the atoms within the simulation box (which one can understand as a $N_x \times N_y \times N_z$ repetition of the unit cell, and I refer to as *supercell*). Therefore, the number of possible interactions that can occur depend on the size of the crystal cell that is used

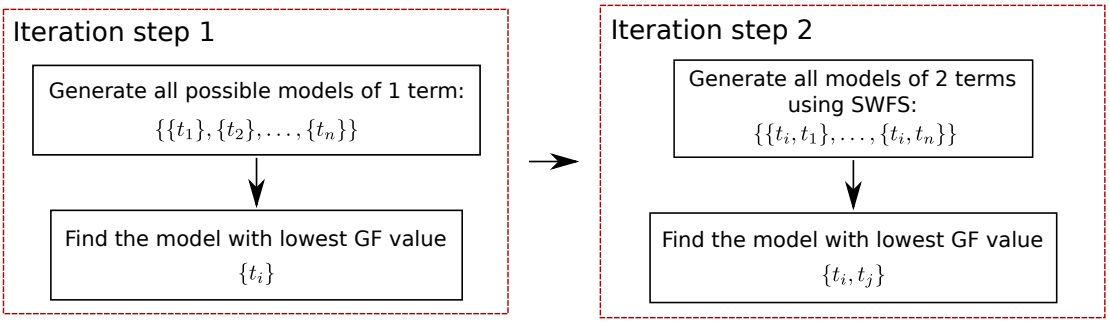


**Figure 3.2:** Iterative scheme of the Step-Wise Forward Selection method (SWFS in the flowchart). All steps for $i > 2$ are analogous to Step 2.

to model the material, and scales exponentially with it. Also, this number can be reduced by a variety of cutoffs that can be easily put in place (see 2.2.3 for a description of the different cutoffs of the model): the maximum order of the polynomial expansion, the maximum allowed spatial range of the interactions, and the maximum number of bodies allowed for a single interaction. It is not difficult to design an algorithm that generates the interactions according to these constraints. Nonetheless, even for small supercells the size of the set of occurring interactions is *large*.

The amount of possible atomic interactions existing even for small supercell (for example, the standard that I am going to use is a $2 \times 2 \times 2$ repetition of the 5-atom unit cell for perovskites, later in the application) challenges the model construction process in practice. I propose a simple example to show the complexity of attempting to build a model using a brute-force approach.

I call $p$-model a model of $p$ terms, where $\mathcal{T}_p \subset \mathcal{T}_P$ and $\Theta_p \subset \Theta_P$. Here, $\mathcal{T}_P$ represents the set of the $P$ possible interactions in the supercell, and $\Theta_P$ are their associated parameters. Usually for the applications and the cutoffs operating for SCALE-UP model potentials, $P \approx 500$. Let us assume that a model of $p = 20$ terms is being constructed, obtained amongst the $P$ terms. Of every $p$-model contained within $\mathcal{T}_P$, and provided a training set, one can compute using the algorithm presented in this chapter the value $\min_{\Theta_p} G[\Theta_p, TS]$ for each $\mathcal{T}_p \subset \mathcal{T}_P$. I define the set of the GF values for models of $p$ terms as

$$\mathcal{G}_p := \{\min_{\Theta_p} G[\Theta_p, \mathrm{TS}] \mid \forall\ \mathcal{T}_p \subset \mathcal{T}_P\}. \tag{3.1.21}$$

The objective is to find the $p$-model that leads to the minimum value of $\mathcal{G}_p$, which I can define as

$$\mathcal{T}_p^* := \{\mathcal{T}_p \subset \mathcal{T}_P \mid \min_{\Theta_p} G[\Theta_p, \mathrm{TS}] = \min\ \mathcal{G}_p\}. \tag{3.1.22}$$

Naturally, $\mathcal{T}_p^*$ has to be found in practice through inspection of all possible $\mathcal{T}_p$. It is then logical that a practical question arises: how many models have to be inspected (and hence, *fitted*) to know which model corresponds to $\mathcal{T}_p^*$? Using the values of the example and simple combinatory, one has

$$\binom{500}{20} = \frac{500!}{50!\,450!} \approx 10^{35} \tag{3.1.23}$$

possible candidates. Even though the scheme to fit models is *extremely* fast, it is in reality unfeasible to inspect all possibilities and find $\mathcal{T}_p^*$.

**Stepwise procedure with forward selection**

In order to overcome this difficulty I propose to use the method of the *Step-wise Forward Selection* [63] (SWFS). This method is a general mathematical procedure that *constructively* adds complexity to the model by attempting to rank the relevance of the terms when presented with the training set data at each step.

The algorithm is described as follows (see Figure 3.2). The first step is to *exactly* find $\mathcal{T}_1^*$, for which there are $P$ possibilities, and hence it is a feasible search. Let us call $t^{1*} \in \mathcal{T}_1^*$ the term constituting the best 1-model. Next, one fins $\mathcal{T}_2^*$ under the constraint that $t^{1*} \in \mathcal{T}_2^*$. This process can be iterated as many times as necessary, until a sufficiently small GF value is obtained.

The process is dramatically more efficient than the brute force method. At each step of the iteration process $(P-i)$ models are inspected, being $i$ the step of the SWFS procedure. Hence the number of steps to build a $p$-model is

$$\sum_{i=0}^{p}(P-i) = (p+1)P - \sum_{i=0}^{p} i = (p+1)\left[P - p/2\right] \ll \frac{P!}{p!(P-p)!}, \tag{3.1.24}$$

where the Newton binomial formula is the number of steps of the brute-force method.

The SWFS method by default is constructive and adds the next most important interaction, but of course, since the space of possible models is constrained one cannot be sure that it is providing the best possible model. I designed two experiments to inspect what was the impact of the constrained search.

In the first experiment, I search through all $p$-models. This is only doable in practice for $p < 5$, and the result of the experiment indicates that the forward selection method selects the best $p$-model in almost all cases.

In the second experiment I refine the SFWS algorithm. The idea behind is to see if there is a term substitution that would lead to a lower value of the GF. In order to do so, at each step the algorithm attempts to substitute any of the terms of the model by another term that is not in the model. By doing this substitution the restriction on the configurational space is effectively weakened. This allows to explore models that are not considered by the SWFS method, although the algorithm remains efficient. I observed that this strategy rarely finds a better choice of model, or if so, never leads to a meaningful change in the GF value.

### 3.1.3 Model validation

The concept of model validation refers to a critical aspect of model construction: how to correctly assess that an optimal model has been generated. In the framework of the presented scheme, for example, this means developing a criterium that would allow to decide what is the optimal amount of terms in the model. In order to talk about the optimal (or best approximative) model it is very useful to introduce two concepts that are the two faces of the same coin: underfitting and overfitting.

In statistics [64], an underfitted model is a model that lack relevant parameters that are needed to describe a particular sampled data. In the methodology presented in this Chapter this corresponds to the training set. Underfitted models tend to have poor description of the main properties

of the training set, which of course leads also to a lack of predicting power. Examples of underfitted models can be polynomial models that do not have enough order to reproduce data that *requires* higher order terms to be described. A good example in perovskties is the requirement of 8th or 12th order Landau potential models to describe monoclinic ferroelectric phases [65]; a model of this family with less order will fail at describing the property of interest.

Overfitting is the opposite to underfitting. An overfitted model will tend to include more parameters than are necessary to describe the training set data. Usually overfitted models have an extremely good accuracy towards the points of the sampled training set, but because it includes parameters that are almost not relevant towards the fit itself, additional features may appear that lead again to a lack of predicting power. An example of overfitting appears when one fits a model to a TS that includes some degree of noise. If the model complexity keeps increasing, there will be a point at which the model will begin to fit the noise, and thus include new parameters that are not relevant and decrease the predictive power of the model.

Model validation methods are designed to avoid the difficulties posed by overfitting and underfitting, i.e., detecting when one has more interactions than needed, or helping to realize that the complexity of the model has to be increased for it to reproduce the particular features that one wants to study.

### Cross-validation

A standard way of dealing with both overfitting and underfitting is through *cross-validation* [66]. It is a technique widely used in machine-learning, neural networks and statistics model fitting in general. The method is useful to estimate accurately when a model is beginning to overfit the data of the training set, although it is known that sometimes such procedure is difficult to apply [67].

Cross-validation is a general tool for model selection. Ideally it assumes that there are two sets of data available: the training set and the validation set (VS). The model is generated by fitting the data of the training set. Every time a new term is added the algorithm evaluates using the model the GF by using the structures contained in the validation set. In general, the training set and the validation set are slightly correlated (and thus the model can hold predictive power). Underfitted models tend to *improve* the agreement towards the validation set at each step, and overfitted models tend to *worsen* their goodnes at reproducing the validation set as the model complexity increases. An example of overfitting signature can be found in Fig. 3.3. The deviation between the curves indicate that the model fitted to the TS is no longer reproducing correctly the VS, and thus the optimal model can be chosen using this criterion.

There are several ways of applying this method. I chose to create a variety of validation sets in order to investigate the applicability of the cross-validation method for model selection purposes. In particular I focused on two main ways of analyzing cross-validation:

- Validation set strongly correlated to the training sets.
- Validation set weakly correlated to the training set.

The first family consists on validation sets for which the data is qualitatively similar to that of the training sets. Because of the strong correlation, it is a possibility that overfitting is not visible

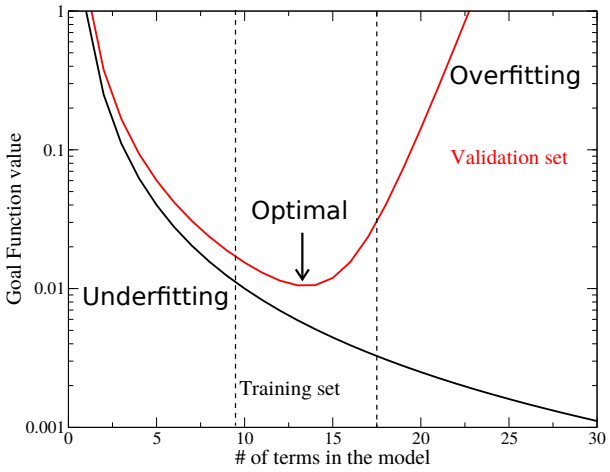


**Figure 3.3:** Sketch of the usual behavior of cross-validation studies when overfitting occurs. The black line represents GF value computed with the model for the configurations of the TS, and the red line, the GF value when the configurations are chosen from the VS. The arrow marks the point at which overfitting begins to occur.

through such sets, although it is still worth to investigate. I apply to this validation set the *leave-n-out method* [66], which consists in the following: let us assume that the training set contains $m$ data points and $n < m$. The training set is randomly split in two new sets: what will become the training set, with $m - n$ random points from the original training set; and what will become the validation set, with $n$ points. Then, and using the context of this Chapter, one fits the models to the training set and validate at each step using the validation set, which by default will be strongly correlated to the training set. The way of validating is through measuring the main estimator in use throughout all the process of model construction: the GF. It is the optimal estimator in this case, because it is a measure of the error towards the data itself.

The second family correspond to validation sets that are less correlated. The idea is that, if the model is presented with data to which the training set is qualitatively different, the validation process will become naturally much more sensitive to overfitting. In other words, overfitting will have stronger impact on data that lies way beyond the extrapolation point than close to it.

### 3.1.4 Boundedness

So far I have discussed in depth the formalism behind the model fitting and generation, and presented a scheme that is not only efficient but also reliable, solid and automatic. There is nonetheless a remarkable obstacle in the model generation process: the unboundedness-from-below.

In mathematics, a set is called unbounded if one *cannot* find a bounding value for it. For example, the model potentials within the `SCALE-UP` framework constitute a function of the type

$$E : \mathbb{R}^{3N} \times \mathbb{R}^6 \longrightarrow \mathbb{R} \tag{3.1.25}$$

$$(\mathbf{u}, \boldsymbol{\eta}) \longmapsto E = E(\mathbf{u}, \boldsymbol{\eta}) \tag{3.1.26}$$

where $\mathbf{u}$ is understood as the vector of displacement vectors, which can be written in the form of a succession of the type $\mathbf{u} := \{\mathbf{u}_i\}$. Since $E$ represents the potential energy of the system, it is physically motivated that $E$ *must* have a lower bound. This is equivalent to say that one can

find a value $b^- \in \mathbb{R}$ for which $b^- \leq E(\mathbf{u}, \boldsymbol{\eta})$ for any $(\mathbf{u}, \boldsymbol{\eta}) \in \mathbb{R}^{3N} \times \mathbb{R}^6$. The motivation for that bound to exist is simple: because of the minimum energy principle, the total energy of a system is minimized at the equilibrium. Hence if there is no minimum, there is no equilibrium.

Studying formally the stability of a multivariate polynomial can be a hard task. In the case of the models discussed here, the question is if $E(\mathbf{u}, \boldsymbol{\eta})$ is bounded from below, which is to say, has a global minimum. I propose a simple method to find the minimum of the energy and study the boundedness-from-below character of it: annealing through Metropolis Monte Carlo method. This algorithm is designed specifically to minimize functions. One of its main characteristics is the inclusion of a temperature parameter, that combined with an annealing factor provides an effective method to find the global minimum of a function. The annealing parameter represents a ratio of decrease in the temperature during the simulation.

For unbounded $E(\mathbf{u}, \boldsymbol{\eta})$, the simulated material will evolve to configurations for which the energy tends to $-\infty$. I call this *runaway solutions*. If it is the case, then one can also study which are the terms of the polynomial that are contributing the most to the runaway solution, usually providing hints on how to correct the model unboundedness.

**Confinement potential**

Applying an effective and fair bound to a model potential represented a difficult task in the development of the method. A frequent question that I asked myself is: given that $\mathcal{T}_p^*$ is unbounded, how can one know if it is a model complete enough to reproduce the key features of the material being modeled? Furthermore: can one find a function that would provide automatic and good boundedness for the models?

The answer is not immediate. In practice, unbounded models allow for atomic configurations that have no physical meaning. For example, a usual behavior of an unbounded model is to predict massive distortions of the atoms and cell parameters leading to very low energies. The distortions tend to be cooperative atomic movements that define a path in the potential energy surface that eventually leads to the runaway solution of the model.

A practical way of preventing these solutions to appear is to apply a sort of cutoff to the model by limiting how much the atoms can move, and how much the cell can be distorted. I propose

$$E^{\text{conf}}(\mathbf{u}, \boldsymbol{\eta}) = \sum_i \theta(||\mathbf{u}_i|| - u_i^c) \left[ k_1 \left( s \frac{||\mathbf{u}_i|| - u_i^c}{u_i^c} \right)^{\alpha} \right] + \theta(||\boldsymbol{\eta}|| - \eta^c) \left[ k_2 \left( s \frac{||\boldsymbol{\eta}|| - \eta^c}{\eta^c} \right)^{\beta} \right]. \tag{3.1.27}$$

where

$$\theta(x) = \begin{cases} 1 & x \geq 0 \\ 0 & x < 0 \end{cases} \tag{3.1.28}$$

is the Heaviside step function, $u_i^c$ is the defined as the maximum absolute distortion of atom $i$, $k_1$ controls the hardness of the potential, $\alpha$ defines the order of the cutoff and $s$ allows for fine tuning of the slope of the potential. Similarily, $\eta^c$ is the maximum absolute distortion of the strain

of the cell, $k_2$ controls the hardness of the potential, $\beta$ defines the order of the cutoff for the strains and $s$ is a fine tuning parameter.

This function imposes a smooth spherical confinement potential around each atom. The potential is activated when the atom displaces more than $u_i^c$ in norm. Then, by choosing $\alpha$ even and higher than the order of the terms contained in the original model this energy contribution is going to dominate in the highly distorted region, plus the different parameters allow to control the hardness of the potential. The confinement for the strains behave in the same way: a six-dimensional sphere is limiting the amount of distortion that the cell can undergo before the confinement becomes relevant enough to prevent further distortions. Moreover, by selecting $u_i^c$ and $\eta^c$ so that they are 5% bigger than the maximum observed in the training set it is ensured that the confinement potential do not affect the area of validity of the model. This kind of confinement potential allows to explore the potential usefulness of a model: for example, one can study if a model can reproduce potentially the ground state of the material.

This method is however not ideal to bound a model for lattice-dynamical simulations. There are two main reasons for this. The first is due to the perturbation they introduce in the points that are beyond the maximum distortion of the training set: the slope will be massively affected by the confinement, and thus the recovery forces lay much beyond what would be physically reasonable. A second, more important problem, is at the effect of this potential over the PES: in my experience it is somewhat frequent that additional secondary minima appear as a result. Secondary minima represent additional, unphysical phases of the material. Thus any sort of temperature-dependent simulation for such a model is automatically rendered useless: statistics will be biased due to both problems. In the following I discuss a more solid method to bound models in practice.

**A method to construct bounded models**

I present here a method for constructing models for which the energy is bound from below. For simplicity, let $p(x)$ be a polynomial of the ring of real polynomials, $\mathbb{R}[x]$. In the following paragraphs I will make an analogy and refer to this polynomial as if it was the energy functional $E(\mathbf{u}, \boldsymbol{\eta})$. It is possible to write

$$p(x) = a_0 + \sum_i a_i x_i + \sum_{ij} a_{ij} x_i x_j + \dots . \tag{3.1.29}$$

Let $m$ be the order of the polynomial $p(x)$. Let us define then a new polynomial $p'(x) = p(x) + q(x)$, where

$$q(x) = \sum_i c_i x_i^n \ , \ c_i \in \mathbb{R}^+ \tag{3.1.30}$$

being $n$ the smallest even integer such that $m < n$. Since for $||x|| \gg 1$ one has $|q(x)| \gg |p(x)|$, then $p'(x) \approx q(x) > -\infty$ and $p'(x)$ is bounded from below.

In the particular case of the SCALE-UP model potentials the displacements that are occurring in the modelled materials are usually relatively small. Hence, in the region of the PES at which the models are fitted the impact of adding higher order terms is minimal. I show this result in the applications of the methodology, as I studied the impact of applying this approach to produce bounded-from-below model potentials.

Note that, in principle, this recipe to apply boundedness to a model could generate additional spureous minima as I am introducing higher orders of the polynomial expansion. However, in my experience a key factor in avoiding this is precisely the fact that here one fits again all coefficients, making this procedure superior to the application of the confinement potential.

Unfortunately, this process is complex to apply in practice. The optimal way to do so would be the following: let us assume that, in the formulation that I have been using in this Section, $p(x)$ and $q(x)$ are known. That is to say: the model potential $p(x)$ has been generated, and one knows what terms to use to obtain a bounded-from-below model, $q(x)$. In my experience, however, there is no way to ensure that fitting such a model will have as results parameters for $q(x)$ that are strictly positive, and it is seldom the case. It depends heavily on the anharmonic character of the potential energy landscape that the training set is describing, on the completeness of the training set, and the terms included in $p(x)$ and their interaction with potential bounding terms in $q(x)$.

Because this approach may fail at first attempt, I have designed a strategy to succesfully produce a model with positive bounding parameters. I recover here the usual notation used previously in the Chapter. Let us propose the following situation: one has succesfully generated $\mathcal{T}_p^*$ that:

- It is not bounded.
- It is complete enough to reproduce correctly the training set, by observing the convergence of the GF value, for example.
- The necessary $q$ polynomial terms, represented by the set $\mathcal{Q}_q$, that would provide boundedness given they are accompanied by corresponding positive parameters.

One option to proceed to fitting the parameters associated to the terms in $\mathcal{Q}_p$ via what is known as constrained optimization problem, which consists in studying the extrema of a function (the GF) under a set of given constraints. Let $\Theta_p^*$ be the set of parameters associated to $\mathcal{T}_p^*$, and $\Theta_q^b$ the set of parameters $\theta_q^b$ associated to $\mathcal{Q}_q$. Then, the optimization problem can be written as

$$\begin{cases} \text{minimize} & G[\Theta_p \cup \Theta_q^b, TS] \\ \text{subject to} & \theta_q^b > 0 \end{cases} \tag{3.1.31}$$

I have shown in this Chapter that solving the problem without any constraint is equivalent to solving a linear system of equations, for which one can find an exact solution. In order to apply the constraint, however, one has to add an additional set of *inequalities* to the system. This is not a difficult task to tackle using a numerical minimization method for $G$, but unfortunately, makes the problem not analytically solvable anymore.

Instead, I propose to apply an algorithm for the search of the positive parameters that satisfy the constrained optimization problem in 3.1.31. In the first step, one fits the best model of $p$ terms found plus the bounding terms, $\mathcal{T}_p^* \cup \mathcal{Q}_p$. If the constraint is satisfied, then the solution is found. If not, the recipe I propose is:

1) Fix the value of the negative bounding parameters to 0.
2) Fit $\mathcal{T}_p^*$, assuming $\theta_q^b$ constant. If the resulting model is bounded, the solution is found.
3) Fit $\mathcal{Q}_p$, assuming $\theta_p^*$ constant. Iterate to Step 1).

This process can be repeated as much as necessary until the exit condition in Step 2 is satisfied. By doing so the core part of the model - which in this development I have referred to as $p(x)$ - is *always* properly fit to the training set, while the bounding parameters are self-consistently meeting the best compromise towards both the constraint and the training set at each iteration.

## 3.2 Application of the method: a model for $SrTiO_3$

In this Section I apply the model construction scheme to build a model for the chemical compound $SrTiO_3$. This material crystallizes in the form of a perovskite structure and has been widely used and studied for a variety of reasons by the scientific community. The delicate lattice-dynamical properties it exhibits make the material challenging to model, and so it is a perfect material to demonstrate the method.

### 3.2.1 What is $SrTiO_3$?

Strontium titanate crystallizes in the form of a perovskite. The system exhibits a perfect cubic phase (with space group associated $Pm\bar{3}m$) above $T_C \approx 110\ K$ [68], where the unit cell is a cube (with lattice parameters $a = b = c$), the oxygens are positioned in the centers of the faces of the cube, the strontium atoms are located at the vertices and the titaniums at the center of the cube. The structure corresponds to the sketch a) in Figure 3.4. This property at room temperature makes the material extensively used as a substrate for sample growth.

When the temperature drops below $T_C$ the material undergoes a phase transition to a tetragonal phase (for which the space group transits to $I4/mcm$), that in this particular case is also known as *antiferrodistortive* (AFD) structure. The distortion leading to this phase involves an anti-phase rotation of the oxygen octahedra, accompanied by a strain of the cell. In Glazer's notation [69], this corresponds to a $a^0a^0c^-$ phase. Experimentally, the angle of rotation is observed to be about 2.1° at 4.2 K [70]. The phase is depicted in the right panel of Figure 3.4.

One of the key aspects that make $SrTiO_3$ complicated to model is related to the stabilization at low temperature of the AFD phase. It has been shown both experimentally [71] and theoretically [72] that this material is prone to develop a polar instability additionally to the AFD one. This led to a long discussion in the scientific community about the possible polar behavior of the material at very low temperatures. It is widely accepted that *quantum fluctuations* are responsible for compensating this instability, ultimately favoring the AFD phase. Hence, strontium titanate is also known as a *quantum paraelectric* [72].

There are two main reasons for this. The first is related to the inherent competitivity between the AFD and the polar instabilities: favoring the AFD mode makes the polar distortion to disappear, and viceversa [73]. This experiment can be performed by applying external pressure or straining the material (for a more detailed discussion on this subject, see Chapter 5).

The second reason is focused on the quantum fluctuations. These essentially prevent the weaker instability, the polar, to condense. The presence of such quantum effects (which rely on the wavelike character of the relatively heavy atoms in strontium titanate) has been shown in the literature [71].

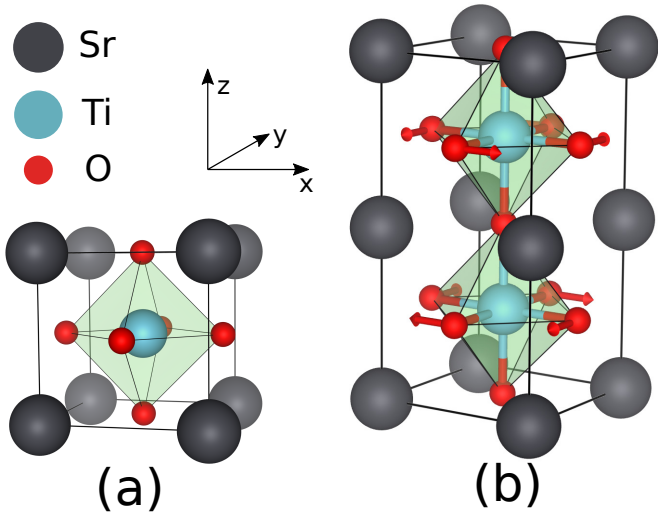


**Figure 3.4:** Atomic structure of Strontium Titanate. **(a)** Sketch of the the ideal cubic structure. **(b)** Displacement of the atoms leading to the ground state of the material, describing an anti-phase rotation of the oxygen octahedra along $z$.

Its signature is most visible in studies about the dielectric constant of the material at low temperatures, for which an anomalous behavior is found [74].

### 3.2.2 Details of the first-principles calculations

The data that I use to fit the models is generated using DFT. To do so I perform a series of simulations for $SrTiO_3$ using the Local Density Approximation (LDA) as implemented in the *Vienna Ab-initio Simulation Package* (`VASP`). While it is true that LDA predicts stronger interaction between atoms that lead to a volume that is usually between 1% and 2% smaller than the experimental results, it is an energy functional that has been widely used to study the material. Hence by using it one can better compare to previous results available in the literature, which is of most importance for assessing the quality of the model generation process.

For the simulations using DFT I use the projector-augmented wave method (PAW) for the ionic core treatment. I solve explicitly the calculation for electrons: Sr's $3s$, $3p$, and $4s$; Ti's $3s$, $3p$, $4s$, and $3d$; and O's $2s$ and $2p$. The `VASP` code uses a plane-wave basis to solve the Schrödinger equation, which I truncate at 500 eV. Also, the integrals in the Brillouin zone are computed in a grid of $6 \times 6 \times 6$ $k$ points for the 5-atom cubic unit cell of the perovskite, or equivalent meshes for bigger cells. I have checked that this is a sufficiently converged $k$ point mesh for the integrals. As for the minimizations of the energy to condense the phases of interest, the simulations are run until the residual force components are converged with an error of 0.01 eV/Å.

An important part of the training set is generated using molecular dynamics, so that one can explore and gather information of the potential energy surface in an automated way. The thermostat is chosen to be a Langevin thermostat implemented using the Parinello-Rahman approach to solve the equations of motion [75, 76]. This allows to simulate also the effect of temperature on the cell parameters, so that the PES for configurations involving both displacements and strains can be studied. The temperature-driven simulations are used to explore the PES rather than obtaining

statistically relevant results. It is for this reason that I focus on the precision of the forces computed rather than optimizing the Langevin thermostat parameters. I adjust these parameters to have a a fast relaxation of the system to the targeted temperature. The starting point of the simulation always corresponds to the RS, which I slightly distort in a random way so that the forces on the atoms are not zero. The time steps for the molecular dynamics simulations are of 2 fs.

In the following Sections I discuss exactly the data used from first-principles.

### Reference Structure

The starting point of the modelling is the definition of the Reference Structure, i.e., the point at which the Taylor expansion is performed (see Section 2.2.2 for a detailed description). It convenient to chose a structure that

- Is of high symmetry. The higher the symmetry, the less independent polynomial terms appear in the model, reducing the overall amount of parameters to be considered.
- Is a critical point of the potential energy surface. This means that $\nabla E = 0$, and as a consequence, the Taylor expansion first non-zero terms will appear at the harmonic order.

The structure selected is the high symmetry cubic perovskite structure $Pm\bar{3}m$. This structure is a saddle point of the potential energy surface, with its instabilities leading to the ground state and other low energy phases of the material. The choice of this RS is common in previous works in the literature as well for this and similar perovskite materials [8, 27, 48, 77, 78].

I use LDA to compute the relaxed lattice parameters of this structure for a unit cell of five atoms, by minimizing the stress of the cell and the forces on the atoms for the cubic cell. The results for the lattice vectors are (in Å):

$$\begin{aligned} a &= (3.865, 0.00, 0.00) \\ b &= (0.00, 3.865, 0.00) \\ c &= (0.00, 0.00, 3.865) \end{aligned} \tag{3.2.1}$$

In Table 3.1 there is a description of the resulting atomic positions, in fractional coordinates.

### Elastic tensor

As discussed in Section 2.2.3 one of the main energy contributions in the model is the elastic energy. This contribution can be computed using the elastic tensor of the material at the RS,

**Table 3.1:** Fractional atomic positions for the cubic structure of $SrTiO_3$.

| | | | |
|---|---|---|---|
| $\mathbf{r}'_{\mathrm{Sr}}$ | 0 | 0 | 0 |
| $\mathbf{r}'_{\mathrm{Ti}}$ | 1/2 | 1/2 | 1/2 |
| $\mathbf{r}'_{\mathrm{O}_1}$ | 0 | 1/2 | 1/2 |
| $\mathbf{r}'_{\mathrm{O}_2}$ | 1/2 | 0 | 1/2 |
| $\mathbf{r}'_{\mathrm{O}_3}$ | 1/2 | 1/2 | 0 |

as I only consider the elastic energy at the harmonic order. Although the parameters could have been fitted using the fitting scheme described previously in this Chapter, in this case it is much more convenient to compute the elastic tensor using DFT and use the computed parameters in the model. The results for this material, using LDA and for the reference structure, are described in Table 3.2.

**Table 3.2:** Elastic tensor components as calculated using LDA for the cubic phase of $SrTiO_3$. Results are in GPa.

| | xx | yy | zz | yz | zx | xy |
|---|---|---|---|---|---|---|
| xx | 388.3 | 111.4 | 111.4 | 0 | 0 | 0 |
| yy | 111.4 | 388.3 | 111.4 | 0 | 0 | 0 |
| zz | 111.4 | 111.4 | 388.3 | 0 | 0 | 0 |
| yz | 0 | 0 | 0 | 118.8 | 0 | 0 |
| zx | 0 | 0 | 0 | 0 | 118.8 | 0 |
| xy | 0 | 0 | 0 | 0 | 0 | 118.8 |

### Dielectric tensor and born effective charges

The `SCALE-UP` model potentials use an expression for the calculation of the long-range dipole-dipole interactions, as described in Chapter 2, which is up to harmonic order. This interaction is computed using the so-called Born effective charges, which are tensors that represent the effective charges accounting for the anisotropy that the atoms may have due to the electronic configurations, and the dielectric constant $\epsilon_\infty$ corresponding to the high frequency dielectric response of the material.

The calculations of both the Born effective charges and the $\epsilon_\infty$ are calculated using LDA for the phase $Pm\bar{3}m$. The values for the tensors are:

$$\mathbf{Z}^*_{\mathrm{Sr}} = \begin{pmatrix} 2.55 & 0 & 0 \\ 0 & 2.55 & 0 \\ 0 & 0 & 2.55 \end{pmatrix}, \quad \mathbf{Z}^*_{\mathrm{Ti}} = \begin{pmatrix} 7.33 & 0 & 0 \\ 0 & 7.33 & 0 \\ 0 & 0 & 7.33 \end{pmatrix}, \quad \mathbf{Z}^*_{\mathrm{O_1}} = \begin{pmatrix} -5.77 & 0 & 0 \\ 0 & -2.06 & 0 \\ 0 & 0 & -2.06 \end{pmatrix},$$
$$\mathbf{Z}^*_{\mathrm{O_2}} = \begin{pmatrix} -2.06 & 0 & 0 \\ 0 & -5.77 & 0 \\ 0 & 0 & -2.06 \end{pmatrix}, \quad \mathbf{Z}^*_{\mathrm{O_3}} = \begin{pmatrix} -2.06 & 0 & 0 \\ 0 & -2.06 & 0 \\ 0 & 0 & -5.77 \end{pmatrix}. \tag{3.2.2}$$

$$\epsilon_\infty = \epsilon_0 \begin{pmatrix} 6.35 & 0.00 & 0.00 \\ 0.00 & 6.35 & 0.00 \\ 0.00 & 0.00 & 6.35 \end{pmatrix} \tag{3.2.3}$$

## 3.2.3 Details of the model

Strontium titanate is a material for which the structure of the different phases do not differ too much in magnitude of distortions. For example, the maximum change in bond between the cubic phase and the tetragonal structure of the ground state as computed with first principles using LDA

is of about 0.16 Å for the Sr-O pairs. Also, the energy difference between the high symmetry phase and the ground state is of -0.012 eV/f.u., which means that the potential energy surface of the material in the area of interest is remarkably flat. Therefore, one conclusion is that one does not need to include an extensive anharmonic description. Since the harmonic order is unbounded due to the instabilities of the RS I decided to use fourth-order polynomials to build the model, which is the minimum anharmonic expansion that allows for a description of the ground state in these conditions.

Previous works in the literature show that the short-range interaction in this and similar materials decay quickly with distance [27, 79], and that a $2 \times 2 \times 2$ repetition of the 5-atom unit cell is enough for the short-range interactions to decay. I generated all the polynomial terms compatible the $2 \times 2 \times 2$ supercell of 40 atoms up to fourth order. Also, the harmonic terms and anharmonic terms have as much as 3-body and 4-body order respectively (i.e., the number of different atoms involved in the interaction). For the short-range interactions, then, I obtain: 45 symmetry-independent harmonic terms, 79 third-order terms and 275 fourth-order interactions. Also, for the strain-phonon coupling (i.e., $E_{sp}$) I obtain 161 terms. Note that the generation of these terms is not restricted to the material, but to the structure. Hence, the interaction terms can be used to generate models for any $ABO_3$ perovskite whose reference structure is the $Pm\bar{3}m$ phase.

### 3.2.4 Model generation

In this Section I describe the process of the model construction in detail. In order to provide a broad description of the process I generate a series of models to understand how different strategies for the model construction affect their performance. I consider two families of models. The first family, that I will call *exact harmonic models* (EHMs), have an exact description of the harmonic order of the Taylor expansion. Then I add the anharmonic interactions and fit them independently to different training sets. The second family, that I will refer to as *free models* (FMs), are models for which all the different orders of the Taylor expansion are fitted at the same time. This allows to explore minimalistic models that contain only the essential harmonic description of the PES.

After fitting the different families of models I analyze the cross-validation and select the best approximative models for $SrTiO_3$. Finally, I explain how to process the boundedness of the models, and study the material's phase transition using Monte Carlo simulations for the different models generated.

#### Fitting the harmonic terms of the EHMs

The harmonic terms of the model are the first non-zero order of the Taylor expansion. These terms are the responsible of the reproduction of the Hessian matrix at the RS. Because of the relationship between the Hessian matrix and the Dynamical matrix, this order of the energy expansion describes the phonons of the RS. In practice it is easy to independently fit the harmonic expansion of the energy. The reason is that the harmonic contribution is the only relevant contribution for very small distortions of the RS, and higher orders can be neglected.

There is a convenient way of obtaining training sets containing all the harmonic description. When one calculates with DFT the Hessian matrix of a crystal using finite-differences, the first-principles code finds the different distortions that are required by symmetry calculate the compo-

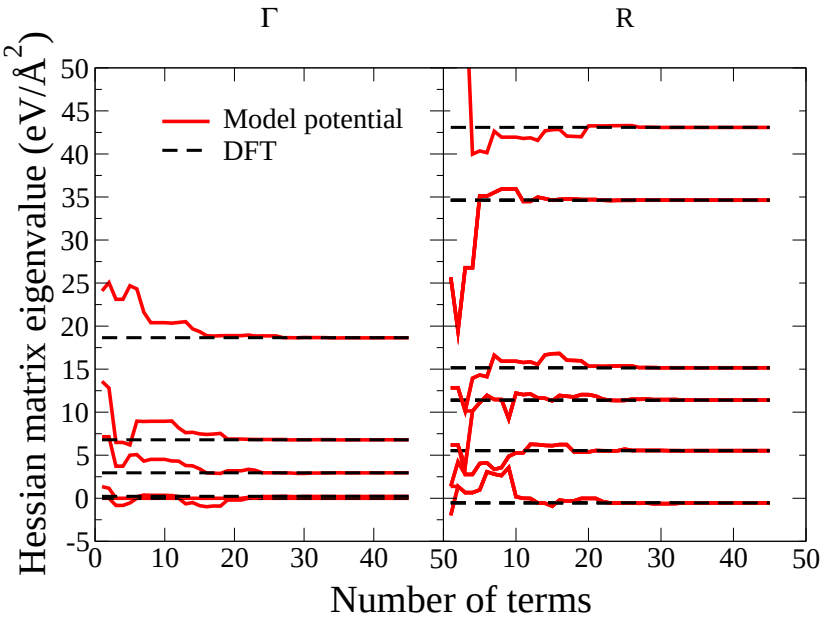


**Figure 3.5:** Eigenvalues obtained from the diagonalization of the Hessian matrix as computed using the harmonic part of the EHMs at two specific **q** points, Γ and $R$. The solid lines indicate how the eigenvalues evolve as the number of terms included in the harmonic part increases. The dashed lines correspond to the values as computed using exact DFT calculations.

nents of the force-constant matrix. By collecting these structures, and the forces on the atoms that the DFT code computes, it is possible to obtain the most appropriate training set for the fitting of the harmonic part. I compute the Hessian matrix using the `VASP` code for the RS, applying displacements of 0.015 Åfor the calculation of the force-constant matrix. I use this TS to fit the 45 independent harmonic terms. Since the method is constructive the terms are added by their relevance at describing the forces and the stresses of the TS.

I present the results of the fit in Figure 3.5. Here I show the eigenvalues of the Hessian matrix and how do they converge to the DFT results throughout the model construction, which is adding terms at each step to the model. The results are for two particular $q$-points that are relevant to this study: the Γ-point (corresponding to $\mathbf{q}_\Gamma = (0,0,0)$) and the R-point (for which $\mathbf{q}_R = 2\pi/a(1/2,1/2,1/2)$), where $a$ is the lattice constant of the cubic 5-atom cell. The main instability is the antiferrodistortive, represented by a negative eigenvalue, three-fold degenerated, belonging to the R-point. The ferroelectric mode, belonging to the Γ-point, has an eigenvalue that is very close to zero but still positive when computing phonons using LDA for $SrTiO_3$ (see Table 3.3). Note that the convergence of the values happens very fast, and the addition of new terms beyond 25-30 terms model does not affect much the result - this is again due to the method of fitting, which includes most important interactions first. The mean absolute error when comparing all the eigenvalues of the Hessian matrix for the $2 \times 2 \times 2$ supercell between the model potential and DFT is of 0.003 eV/Å$^2$. As a final remark, it is worth mentioning that the process of fitting the harmonic part of the EHMs takes less than one minute.

**Fitting the anharmonic terms: training sets**

For the anharmonic part of the models I use DFT molecular dynamics to produce the data of the training sets. This simulation method is well suited to explore the potential energy surface in an automatic way, and the temperature is the main property that one can use to select which region of the PES is being sampled.

The collection of data is a rather simple process. From a molecular dynamics trajectory I select steps in a random but evenly spaced way. Then I extract the atomic positions, strains of the cell, forces on atoms, stresses and energy from this colection of steps. Since I define the origin of the energy and the path is evenly spaced in the configurational space, by fitting the forces and stresses one effectively fits an interpolated path between the origin and the equillibrium state. With this strategy, even though the method does not explicitely fit the energies of the MD trajectory, the energetics of the model have good agreement with DFT. I typically extract 100 configurations (homogeneously distributed) from a molecular dynamics run.

A key aspect is to have a good description of the configurations in the path between the reference structure and the ground state of the material. Experimentally it is known that the phase transition occurs around 110 K. The first training set considered, then, is a MD trajectory at 10 K, from which I extract a training set that will be called TS@10 in the following. This training set is expected to provide information of the path connecting the RS and the ground state of the material. The reason is that the stabilization of the energy after the thermalization process has to be somewhat close to the ground state.

I am also interested by the impact of fitting higher energy regions of the PES for the model's performance. In order to study this I generated a similar training set as the one described, but with the MD simulation run at 300 K. I call the resulting training set TS@300. Through this data the fitting process has access to higher energy structures. The motivation to do so is that, even though this may have an impact in having worse description of the structure of the ground state itself, the information of the phonons that are activated at higher temperature may have an impact on how well the model potentials perform to simulate phase transitions or produce statistics for higher temperatures.

Additionally, I generate trajectories at 200 K and 500 K as validation sets (VS@200 and VS@500). Having this information is useful to study cross-validation for the models, because it is information that is not present in any of the training sets. Also, it allows to study how good the models can extrapolate.

In the Figure 3.6 I show an example of the trajectories that I obtain from the simulations performed with DFT, in this case, for the 10 K run. Typically these simulations are run for 1500 fs.

**Table 3.3:** Comparison between the eigenvalues of the Hessian matrix for the antiferrodistortive ($R$-point) and polar ($\Gamma$-point) modes predicted using EHMs and as computed using DFT. Values in eV/Å$^2$.

| | Model potential | DFT |
|---|---|---|
| R-point AFD mode eigenvalue | -0.54 | -0.54 |
| $\Gamma$-point polar mode eigenvalue | 0.22 | 0.23 |

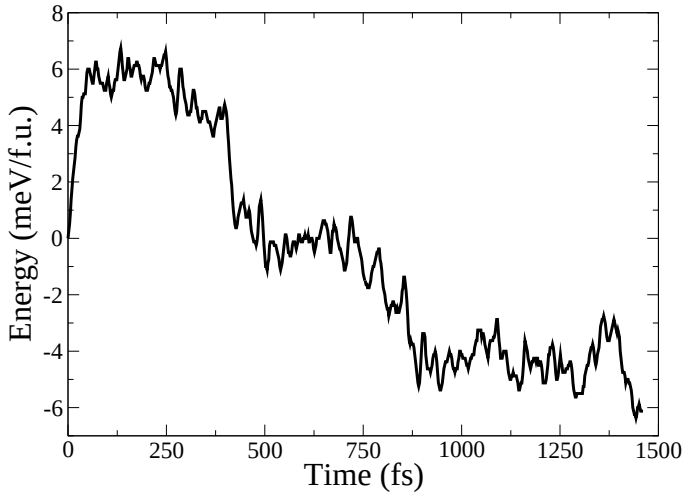


**Figure 3.6:** Energy as a function of time corresponding to a molecular dynamics simulation as performed with DFT to extract the training set data. In particular, this case corresponds to a TS@10 energy trajectory. The beginning of the run is at a point very close to the cubic structure, which is taken as zero energy in the plot. The end of the plot is at a region that has the caracteristic structure of the ground state, thus the trajectory is enough to provide with the required information of the path.

Initially the trajectory is observed to evolve around the cubic phase, and then the system's energy drops to energies close to the ground state.

### Fitting the anharmonic terms: the model construction

I define three types of models to study the impact of using different training sets for the model construction process, both in the FMs and the EHMs families (see Table 3.4 for a summary).

The first type is produced to have a good description of the ground state and is fitted to TS@10. The second model type is designed to study what happens when information that is far from the ground state is provided in the TS, and is fitted to the TS@300. Finally, I combine both training sets to fit a third type of model that includes the two training sets, hopefully capturing the features

**Table 3.4:** List of the models generated for Strontium Titanate. The last column indicates the amount of terms that each model contains. For the EHMs I also indicate that 45 harmonic couplings are retained, which define the complete fit of the harmonic part of the $E_{\mathrm{p}}$ energy.

| Number | Model type | TS | Terms retained |
|---|---|---|---|
| 1 | FM | TS@10 | 33 |
| 2 | EHM | TS@10 | 45+10 |
| 3 | FM | TS@300 | 37 |
| 4 | EHM | TS@300 | 45+17 |
| 5 | FM | TS@10+300 | 44 |
| 6 | EHM | TS@10+300 | 45+14 |

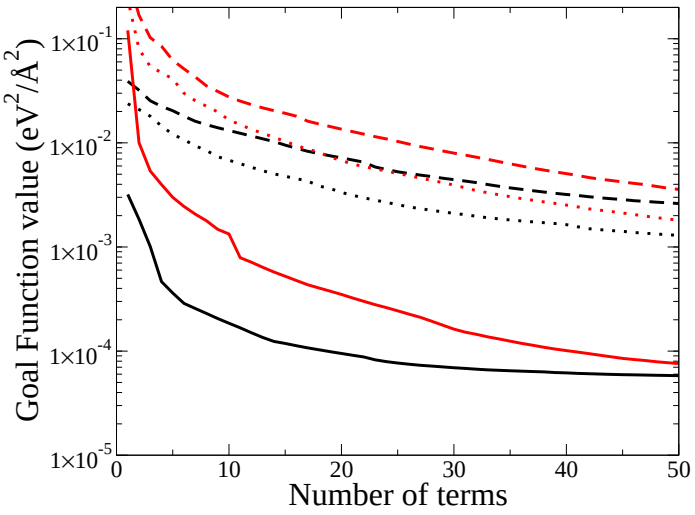


**Figure 3.7:** GF value as a result of the fit for every step of the model construction process for the models considered. Red and black lines correspond to FM and EHM models, respectively. Solid, dashed, and dotted lines correspond to the models fitted to the TS@10, TS@300 and TS@10+300, respectively.

that are relevant in both training sets into the same model through the best compromise. I call this training set TS@10+300.

Experience in the model construction process proved that even the TS@10 posed some problematics at fitting models that would have the correct ground state. Instead, my findings are that those models were prone to show sometimes another phase as the ground state, namely the $a^0a^0c^+$ phase in Glazer notation. This phase is structurally very similar to the ground state itself, which is $a^0a^0c^-$, but has an *in-phase* rotation instead in adjacent cells along the $z$ direction. In fact, the energies of both structures are surprisingly similar when computed using DFT. Because of this, I decided to provide the fitting process of the models with accurate information about the Hessian matrix of the $a^0a^0c^+$ phase. This shows a very important fact of the model generation process: sometimes the resulting model provides information of what data the TS may be lacking, and one can always refine the training set to improve the resulting model by adding new information.

At this point the only reliable value to track the progress of the model construction is the GF value. I observed that after 50 terms the GF value was not improving significantly, so I constructed all models to have as many as this amount of terms. An example of the evolution of the GF value can be found in Figure 3.7.

### Model validation

The application of the leave-$n$-out method described in the formalism section of this Chapter was adapted to be most suitable for the model potentials generated. In the Figure 3.7 I plot the value of the GF as a function of the number of terms in the model for all the models produced. It is a good example of how the process of fitting works in all cases: the drop of the GF is high at the beginning of the fitting because of the construction method, and converges to a sufficiently low error value. The error converges in all cases in values between $10^{-4}$ and $10^{-2}$ eV$^2$ Å$^{-2}$, which are the units of the GF itself. The difference in the convergence value is due to the magnitude of the

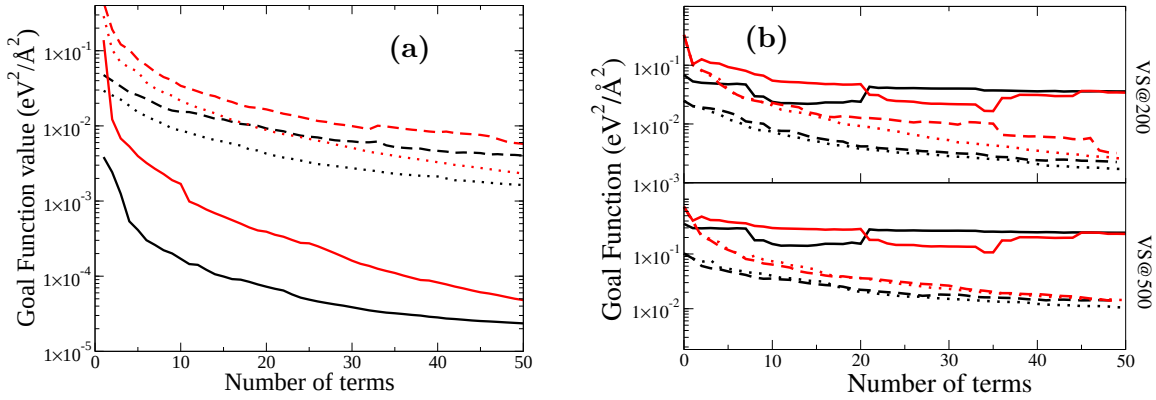


**Figure 3.8:** Application of different approaches of the leave-$n$-out cross-validation method to the FMs and EHMs. The code for color and line types is the same of Figure 3.7 **(a)** Goal function evaluated using qualitatively similar TS and VS. **(b)** Goal function evaluated using qualitatively different TS and VS.

forces that appear in the different training sets: naturally, forces are of higher magnitude in the TS@300 than the TS@10. Also, EHMs always outperform FMs regarding the GF value, which is to be expected. The reason is that the starting point of EHMs is already a perfect description of the harmonic part of the energy, which is an advantageous point with respect the case of the FMs.

It is relatively easy to apply the cross-validation method. Once all the intermediate models are known, it consists on using a particular validation set to *evaluate* the GF for the already fitted model. As has been described in the Formalism section, this usually produces a divergence between the evaluation using the TS and the VS indicating the point at which adding more terms to the model lead to overfitting.

First, I apply this strategy using validation sets that are qualitatively similar to the training sets used for the fit. For example, for EHM models fitted to TS@10, I use VS@10 that contains 50 configurations that were not used during the fitting process. The result is shown in panel (a) of Figure 3.8. The curves are very similar to those obtained in Figure 3.7, both qualitatively and quantitatively. The characteristic cross-validation feature of a minimum appearing in the curves is not present in the plot. This means that overfitting is not happening, or that the VS used to cross-validate is not providing enough information. In either case, the conclusion is that this way of cross-validation is not sufficient to define an appropriate stopping criterium for the model construction process.

Alternatively, I also used qualitatively different validation sets to check the cross-validation approach (namely VS@200 and VS@500). The result can be found in panel (b) of Figure 3.8. In this case the curves do behave very different to those of Figures 3.7 and panel (a) of Figure 3.8. In particular, the curves corresponding to the models fitted to TS@10 show the most disagreement at reproducing the VS. For these models the characteristic minimum indicating the point at which overfitting starts to appear is present. Nonetheles, it is not unique and the trend of the curves seems to indicate that still there is some improvement after that point, and hence the conclusion is unclear. For the models fitted to TS@10+300 and TS@300 the reproduction of the validation sets is good, without a minimum of the GF value, and thus as before the cross-validation method does

not provide a stopping criterium.

The results of the cross-validation process, both for quantitatively similar and different VS, shows to be not conclusive enough for the methodology and the models generated. Since it does not allow to select optimal models, I decided to design a different scheme.

**Best approximative models: a stopping criterium**

I choose to inspect the key aspects that I required the models to reproduce as a stopping criterium. First, models should predict a ground state for the material that is structurally correct with respect to the DFT prediction. Also, the models have to reproduce well the energetics of the material. The reason is that it has been shown in the literature that the depth of the energy minimum plays an important role for phase transition studies and for the amplitude of the distortions involved [80]. I use a Metropolis Monte Carlo simulation to study the ground state properties of the models through a simulated annealing. In this type of simulation the temperature is decreased at every step, so the simulated atoms relax into their ground state positions. I apply the confinement potential described in the Section 3.1.4 to avoid runaway solutions. This confinement potential is designed to not affect the energetics at the region in which the TS is valid, which includes the ground state.

These key properties of the models throughout the model construction process are summarized in Figure 3.9. First, I present the performance of the models at reproducing the order parameter of the phase transition, which is the rotation angle of the oxygen octahedra. I also plot the energy of the ground state. Both quantities are contrasted with the black dashed line, which is the DFT result. Then, I plot the energy predicted by the model for the configurations present in the training set - the same that was used to generate each model, respectively - and the validation sets VS@200 and VS@500.

The results provide information on the predictive power of the model potentials. First, it is clear that the EHM fitted to TS@10 clearly have the most disagreement towards the energies of the validation set obtained at 500 K. It is a result that could be expected, since the extrapolation range is wide - the same model performs much better at the range of energies of the VS@200. On the other hand, the rest of curves for the EHMs have a monotonic character, and thus do not allow for model selection - even though in general accuracy improves drastically after around 10 terms in most cases. FMs tend to have a more erratic character. The error with respect to the energies varies strongly throughout the process and is higher than in the EHMs. After around 10 terms the model potentials fitted to TS@10 tend to have a good agreement with the energy of the ground state. Note also that the red lines, which correspond to the models fitted to TS@10+300, have an overall good behavior at extrapolating the energies, suggesting that indeed using information from both high and low energy structures provides models with good predicting power.

Second, the information included in the analysis of the ground state properties provides more information than the study of the cross-validation. For the EHMs, it is clear that the model potential fitted to TS@10 performs very well at both describing the rotation angle predicted by LDA and the energy difference between the cubic phase and the ground state in around 10 terms. However, for the case of the EHMs fitted to TS@10+300 and TS@300 the convergence of the results to the correct ground state properties is much slower. Not only the stabilization of the rotation angle requires more terms, but the energy depth of the minima varies much more and converges to a

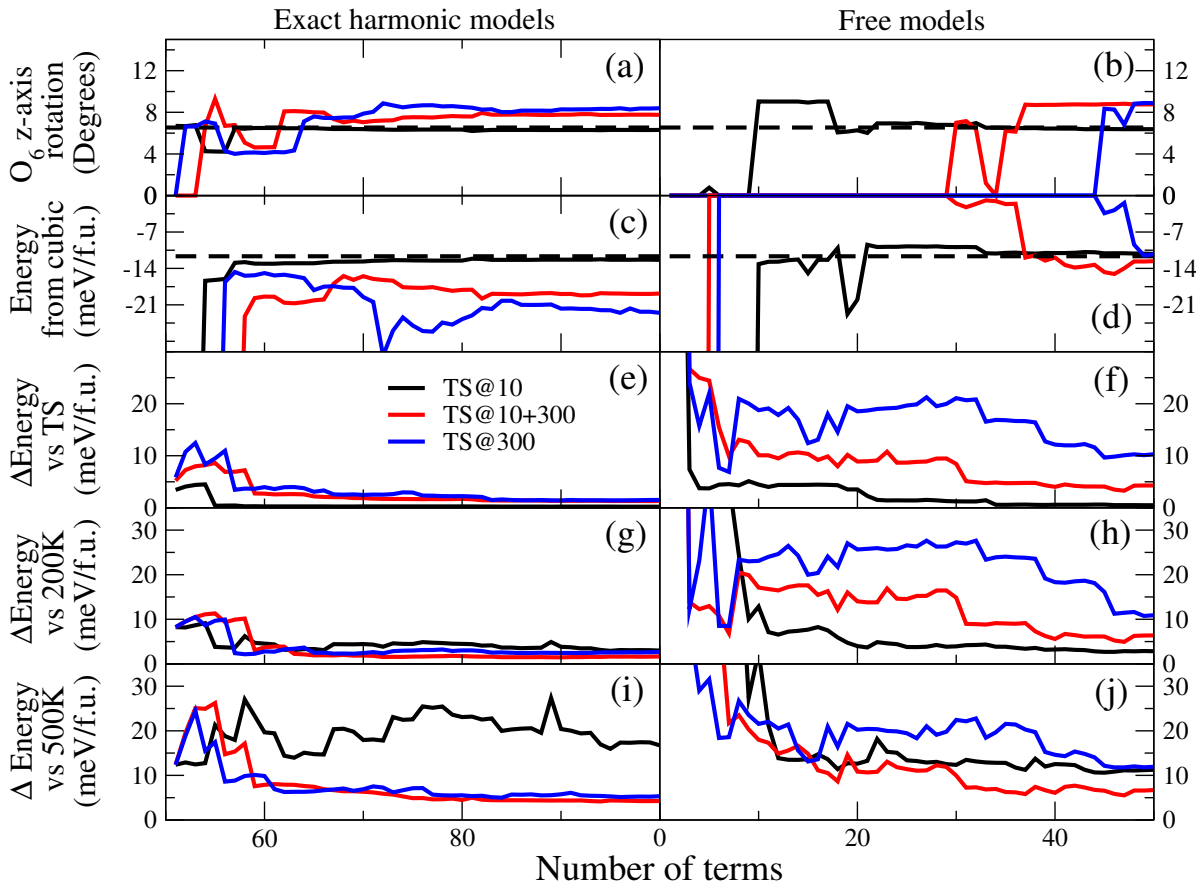


**Figure 3.9:** Reproduction of the six model potentials of both ground state [(a)-(d)] and MD [(e)-(j)] key quantities. The data for panels (e)-(j) was obtained by using the model potentials to compute the energy of the configurations visited during the several MD-DFT at the different temperatures discussed in the text. The average difference between the DFT calculation of the energy and the value obtained using the model is presented in these panels. Note that the exact harmonic models have already the 45 harmonic terms.

value that differs with the DFT result by the order of 10 to 20 meV/f.u., which is significant in comparison to the performance of the model fitted to TS@10. Also, the convergence happens even later for the model fitted to TS@300. I expected some inaccuracy in these models at describing the ground state due to the data included in the training sets, but this fact was not observable in the cross-validation Figure 3.7 and in the panels of Figure 3.8.

Finally, the FM case shows to be always somewhat more complicated than that of the EHMs. Again, the convergence is faster for models fitted to TS@10 although it is less stable and appears later than for EHMs fitted to the same TS. In the case of the models fitted to higher energies the convergence is even slower, the models requiring a large pool of terms to begin reproducing properly the ground state. It is not surprising, though; one has to take into account that still, these models need to find both the harmonic and the anharmonic relevant terms leading to the model able to reproduce the main features of the TS, and thus these are models with less terms than the case of the respective EHMs.

With this information at hand Figure 3.9 provides with enough information to use as stopping criterium for the model potential generation process. Through the analysis of it I have selected

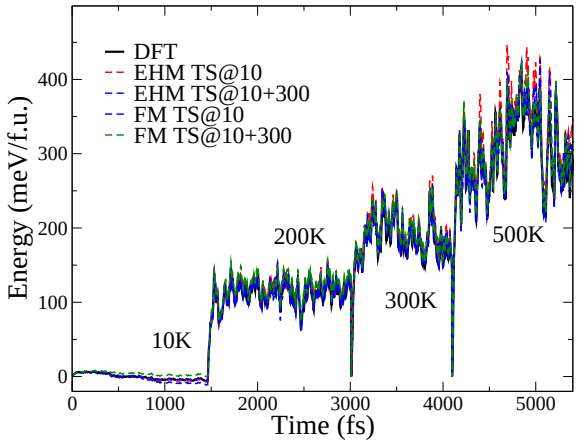


**Figure 3.10:** Evaluation of the various molecular dynamics trajectories computed using DFT by using the best approximative models generated

the number of terms that each model will retain in order to be minimalistic but still having good performance. This information can be found in Table 3.4.

### Applying boundedness

In the Formalism section of this Chapter I already discussed the two most relevant methods to bound models. Namely, one is based on defining a spherical confinement potential for the atoms, which is extremely useful to analyze which is the ground state that the model would have if it was bounded. This approach was used to produce the data of Figure 3.9. The second is based on identifying high-and-even order terms with positive parameters, ensuring the boundedness-from-below of the polynomial. It is the approach that I use to produce the final models.

I studied the runaway solutions to find which were the most appropriate sixth-order terms to use to bound the model. This can be depicted through an example. The model FM fitted to TS@10 is a case of an unbounded model at this point. Through annealed Monte Carlo simulations I found that the leading interaction to the runaway solution was driven by the third-order interaction pair $(\mathrm{Ti}_x - \mathrm{O}_{1x})^3$ (this simplified notation is explained in the example of Eq. 3.1.19). Since this interaction is of third-order character it will always be *unbounded*, regardless of the sign of the parameter associated. One can bound that interaction easily: by simply using $(\mathrm{Ti}_x - \mathrm{O}_{1x})^6$, with a positive associated parameter, it is ensured that the collective motion that this term represents is no longer

**Table 3.5:** Mean absolute error between the energies as predicted by the models and the DFT energy, for the configurations of the several MD trajectories of Figure 3.10. Units are meV/f.u.

| | EHM TS@10 | EHM TS@10+300 | FM TS@10 | FM TS@10+300 |
|---|---|---|---|---|
| $\lvert\overline{\Delta E}\rvert$ TS@10 | 0.4 | 2.1 | 0.7 | 4.4 |
| $\lvert\overline{\Delta E}\rvert$ VS@200 | 4.0 | 2.0 | 2.6 | 8.6 |
| $\lvert\overline{\Delta E}\rvert$ TS@300 | 10.4 | 1.1 | 5.6 | 8.3 |
| $\lvert\overline{\Delta E}\rvert$ VS@500 | 20.9 | 1.3 | 7.0 | 8.9 |

a runaway solution. Then, it is just a matter of refitting the rest of the terms of the model, by leaving this parameter unchanged, to obtain a model that cannot have that type of unboundedness. By iterating this process for all the runaway solutions it is a rather quick process to eliminate all the runaway solutions and obtain a model that is bounded.

This strategy eventually evolved into a slightly more automated, generic method to obtain bounded models. It is formally explained in Section 3.1.4.

### 3.2.5 Analysis of the best approximative models and their interactions

In this Section I will analyze the selected approximative models and their interactions to better understand their features and the physics behind the couplings that they contain.

#### Performance of the best approximative models

I study the performance of the bounded models from two different perspectives. I consider only models fitted to TS@10 and TS@10+300, because the models fitted to TS@300 have a poor description of the ground state and I decided that for the context of the example of the method they fall out of the scope.

The first performance test is a direct comparison with DFT regarding the molecular dynamics trajectories computed at the quantum mechanical level used to extract the TS and VS data. Figure 3.10 consists in a simple evaluation of all the configurations of the trajectories, so that one can have a direct comparison with respect the DFT energies. I would like to highlight the fact that in the training set related trajectories the best approximative models perform extremely well with respect to DFT. In fact, the energies lie so close to the DFT line that it becomes complicated distinguishing the difference.

In Table 3.5 I give the numerical error in the evaluation of the MD trajectories by the model. Note that the models fitted to TS@10 tend to have an almost perfect description of the energy of their training sets. On the other hand, models fitted to TS@10+300 have an overall good description of the energetics even for the trajectory of VS@500. This is due to the selection of the training set, which contains information of a wider range of energies and their associated structures. The reproduction of the energies of VS@200 is good for both the models fitted to TS@10 and TS@10+300. Note that in the first case this indicates a good predictive power. The biggest difference appears for the high temperature trajectory, for which one can see that the models fitted to TS@10 begin to fail to properly predict the energy. However, the result coming from the models

**Table 3.6:** Key features of the best approximative models selected for Strontium Titanate. The data is computed with the models after ensuring boundedness-from-below. The values for the original models (unbounded) are shown in parenthesis. In the last row, $\Delta E$ represents the average energy difference between the model's prediction and the DFT results.

| | FM TS@10 | EHM TS@10 | FM TS@10+300 | EHM TS@10+300 | LDA |
|---|---|---|---|---|---|
| $O_6$ rotation (degrees) | 6.5 (6.5) | 6.5 (6.5) | 9.9 (8.7) | 8.3 (8.1) | 6.5 |
| Ground state energy (meV/f.u.) | −11.1 (−11.1) | −13.2 (−13.1) | −13.2 (−11.9) | −22.9 (−20.5) | −11.7 |
| Goal function ($eV^2Å^{-2} \times 10^{-3}$) | 0.14 (0.14) | 0.18 (0.19) | 2.79 (2.81) | 4.94 (5.04) | |
| $\Delta E$ (meV/f.u.) | 0.6 (1.5) | 0.3 (0.3) | 4.7 (4.8) | 2.3 (2.6) | |

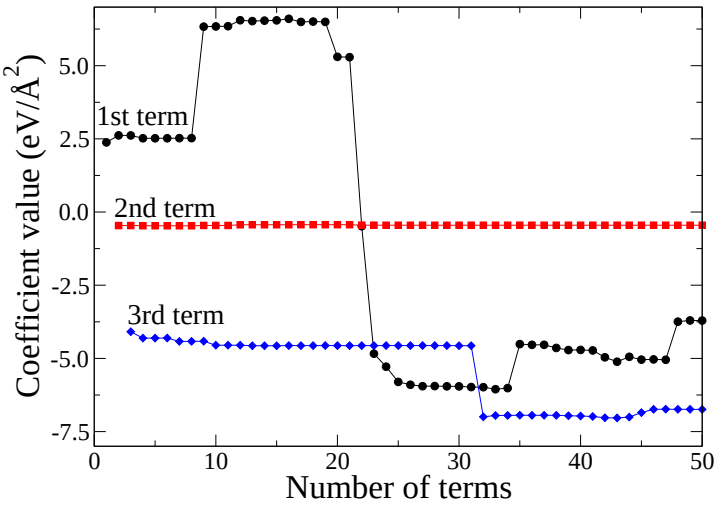


**Figure 3.11:** Values of the three parameters that the fitting procedure selects as most relevant to construct the EHM fitted to TS@10. The three terms are linear in strain and quadratic in the atomic distortions; hence, they all have the same units, as indicated in the figure.

fitted to TS@10+300 is indeed good. This is in agreement with the discussion related to Figure 3.9.

In the Table 3.6 I have summarized the main features of the different models that I use to study the phase transition temperature of $SrTiO_3$. As one can see, applying the boundedness condition to the models does not affect the overall accuracy of the models. The reasoning behind this is that, since the distortions of the material at the ground state are quantitatively small, adding higher polynomial orders does not have a big impact on the performance of the model. Also, it is clear from the table that the ground state properties are quantitatively very close to the LDA results for the models fitted to TS@10. The models fitted to TS@10+300 show an important deviation both in the energy depth of the minimum and the rotation of the oxygen octahedra. The GF value after the fitting process is quite low, and the average energy deviation with respect the TS structures is below 5 meV/f.u. in all cases. However, the FMs tend to perform slightly worse in this sense compared to the EHMs, with the exception of FM fitted to TS@10. The explanation that I find most suitable for this is that free models have less restrictions towards tuning slightly the harmonic part to fit better the overall derivatives of the energy in the trajectory.

### The physical picture of the interactions

The models that I have produced have, by construction, the most important interactions out of a pool that contains essentially all available couplings within the proposed 40-atom supercell. I retain about 10% of the original available terms in the final models, and because of this one can extract conclusions about which are the driving interactions in Strontium Titanate.

As the model construction process takes place, at every step all the couplings are refitted. This means that there can be couplings that cover relatively similar aspects of the dynamics of the system, and this has an impact in the value obtained for the parameters associated. I propose as an example the case of the values of the parameters related to the three most important anharmonic

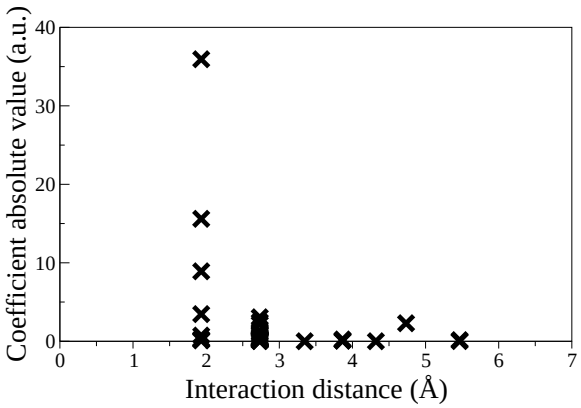


**Figure 3.12:** Values of the parameters obtained for the FM fitted to TS@10 and ordered as a function of the longest interatomic separation associated to the corresponding coupling. Note that this figure includes information about the parameters corresponding to different order of the Taylor series, which thus have different units; hence, I indicate arbitrary units (a.u.) and stress that this figure is to be taken only as a qualitative illustration of the spatial decay of the interactions.

interactions of the EHM fitted to TS@10. The evolution of the parameters is shown in Figure 3.11, and the associated couplings can be found in Table 3.7.

In this example, the second most important interaction remains somewhat constant throughout the process of the model construction. The case of the first and third most important interactions is different, as they show important variations in their parameter values. Notably for the first interaction, around the addition of the 9th and 22nd terms, the sign of the parameter changes. This coupling describes how the strains of the cell interact with the nearest-neighboring oxygens. The reason behind this changes can be understood by observing the interactions that are added in 9th and 22nd place, also displayed in Table 3.7. The couplings added at these steps correspond to interactions that resemble much to that of the most important interaction. The three terms represent relatively similar interatomic forces and cell stresses appearing in the TS data. Hence, the weight of the interaction is distributed amongst them, leading to the strong changes in the parameter value of the most important interaction of the model. In order to make explicit this resemblance I have also explicited the value of the GF when these three parameters are fitted separately, and one can observe that the GF value that they achieve is actually very similar. Thus the selection of one instead of the others is most likely due to particular details in the training sets.

**Table 3.7:** Each row corresponds to one of the three parameters identified to be the most relevant ones for the EHM model fitted to TS@10, indicated by #1, #2, and #3, respectively. I indicate the corresponding interaction and, in parenthesis, the value of the GF corresponding to the best models, respectively. Further, I indicate the terms that are related with these most important ones and whose inclusion in the model causes the discontinuities in their values shown in Fig. 3.11. Thus, for parameter #1, I also include parameters #9 and #22. In such cases, I give in parenthesis the value of the GF that corresponds to considering a best 1-model composed of parameter #9 or #22. All GF values are given in $\mathrm{eV}^2\mathrm{Å}^{-2}$.

| | | |
|---|---|---|
| #1: $\eta_2(\mathrm{O1}_x - \mathrm{O2}_x)(\mathrm{O1}_y - \mathrm{O2}_y)$ (0.00320) | #9: $\eta_1(\mathrm{Ti}_x - \mathrm{O3}_x)^2$ (0.00328) | #22: $\eta_3(\mathrm{O2}_y - \mathrm{O3}_y)^2$ (0.00324) |
| #2: $\eta_1(\mathrm{O2}_z - \mathrm{O3}_z)^2$ (0.00185) | | |
| #3: $\eta_4(\mathrm{Sr}_z - \mathrm{O1}_z)(\mathrm{Sr}_y - \mathrm{O1}_y)$ (0.00101) | #32: $\eta_4(\mathrm{O1}_y - \mathrm{O3}_y)(\mathrm{O1}_x - \mathrm{O3}_x)$ (0.00102) | |

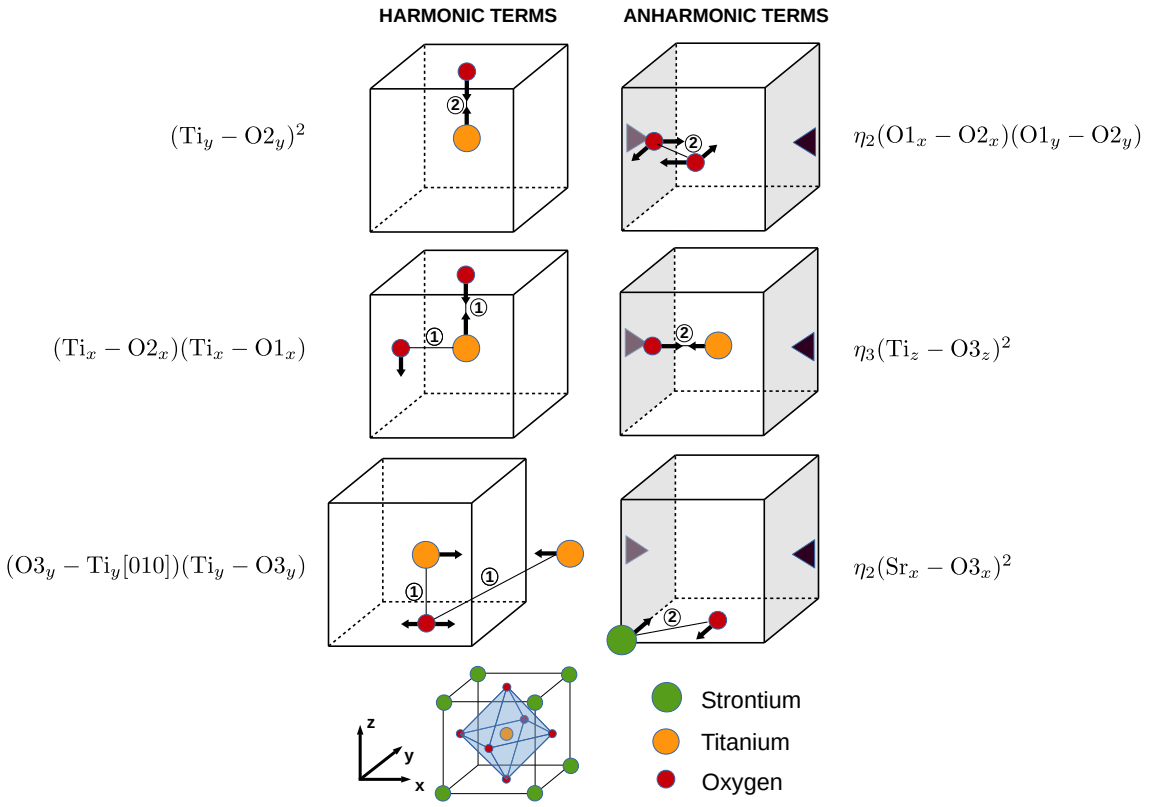


**Figure 3.13:** Sketch of the most important interactions identified by the automatic fitting procedure. Strains are indicated with dark triangles. A circled number indicates the exponent of a specific displacement-difference term.

At this point it is relevant to comment on the initial assumption of the decay of the important interactions with distance - i.e., the short-range character of the couplings. For this reason I show in Figure 3.12 the parameter value as a function of the distance between the atoms that are present in the coupling. The magnitude of the interactions strongly decrease in distance, and there are no interactions acting upon distances bigger than 5.5 Å for the FM model fitted to TS@10, which I took as example. This also confirms that the choice of a 40-atom supercell to produce the DFT data to fit the short-range part of the models was sufficient.

I have also identified by inspection the interactions that seem to be most relevant both at the harmonic and the anharmonic level, and sketched them in Figure 3.13. Also, in Table 3.8 I summarized the best ranked interactions of the different best approximative models generated.

According to these results, the most relevant interactions identified by the model construction process are not depending on the training set used to generate the model. Interestingly, the type of the harmonic part provided - exact or limited - seems not to have a big impact on the selection of the most important anharmonic terms. Also, the leading interactions tend to reflect the oxygen octahedra distortion that leads to the AFD ground state and the polar distortion (involving displacements of cations opposed to anions) that competes with it. The three most important interaction describe the motion of the titanium with respect the oxygens, which when displaced in

opposed motion leads to the creation of dipoles in the cell. From Table 3.8 it is clear the coupling between the strains and oxygens appear to be most relevant at the anharmonic level, allowing for the stabilization of the low energy phase in the material.

**Table 3.8:** List of most important interactions, as selected by the automatic fitting procedure, for the FM and EHM models fitted to TS@10 and TS@10+300. The harmonic part is common to both EHM models. The numbers indicate the order in which the interactions appeared in the corresponding automatic selection process. I tag using an asterisk the couplings sketched in Fig. 3.13.

| **Free models** | |
|---|---|
| **TS@10** | **TS@10+300** |
| Harmonic part of $E_{\rm p}$ | |
| #1*: $(\mathrm{Ti}_y - \mathrm{O2}_y)^2$ | #1*: $(\mathrm{Ti}_y - \mathrm{O2}_y)^2$ |
| #2*: $(\mathrm{O3}_y - \mathrm{Ti}_y[010])(\mathrm{Ti}_y - \mathrm{O3}_y)$ | #2*: $(\mathrm{O3}_y - \mathrm{Ti}_y[010])(\mathrm{Ti}_y - \mathrm{O3}_y)$ |
| #6: $(\mathrm{Sr}_x - \mathrm{O1}_x)(\mathrm{Sr}_z - \mathrm{O3}_z)$ | #4: $(\mathrm{Sr}_x - \mathrm{O1}_x)(\mathrm{Sr}_z - \mathrm{O3}_z)$ |
| Anharmonic part of $E_{\rm p}$ | |
| #13: $(\mathrm{Sr}_x - \mathrm{O2}_x)^2(\mathrm{Sr}_z - \mathrm{O3}_z)$ | #8: $(\mathrm{Ti}_y - \mathrm{O2}_y)^3$ |
| #14: $(\mathrm{Ti}_z[010] - \mathrm{O2}_z[010])(\mathrm{Ti}_z - \mathrm{O2}_z[010])(\mathrm{Ti}_y - \mathrm{O2}_y[010])$ | #14: $(\mathrm{Ti}_z[010] - \mathrm{O2}_z[010])(\mathrm{Ti}_z - \mathrm{O2}_z[010])(\mathrm{Ti}_y - \mathrm{O2}_y[010])$ |
| #18: $(\mathrm{Sr}_x - \mathrm{O2}_x)^2(\mathrm{O2}_x - \mathrm{Sr}_x[001])^2$ | #16: $(\mathrm{Sr}_z - \mathrm{O1}_z)(\mathrm{Sr}_y - \mathrm{O1}_y)^2$ |
| Strain-phonon coupling $E_{\rm sp}$ | |
| #3*: $\eta_2(\mathrm{O1}_x - \mathrm{O2}_x)(\mathrm{O1}_y - \mathrm{O2}_y)$ | #3*: $\eta_3(\mathrm{Ti}_z - \mathrm{O3}_z)^2$ |
| #4*: $\eta_2(\mathrm{Sr}_x - \mathrm{O3}_x)^2$ | #9*: $\eta_2(\mathrm{O1}_x - \mathrm{O2}_x)(\mathrm{O1}_y - \mathrm{O2}_y)$ |
| #5: $\eta_6(\mathrm{Sr}_y - \mathrm{O3}_y[001])(\mathrm{Sr}_x - \mathrm{O3}_x[001])$ | #10*: $\eta_2(\mathrm{Sr}_x - \mathrm{O3}_x)^2$ |
| **Exact harmonic models** | |
| Harmonic part of $E_{\rm p}$ | |
| #1*: $(\mathrm{Ti}_y - \mathrm{O2}_y)^2$ | |
| #2*: $(\mathrm{Ti}_x - \mathrm{O2}_x)(\mathrm{Ti}_x - \mathrm{O1}_x)$ | |
| #3*: $(\mathrm{O3}_y - \mathrm{Ti}_y[010])(\mathrm{Ti}_y - \mathrm{O3}_y)$ | |
| **TS@10** | **TS@10+300** |
| Anharmonic part of $E_{\rm p}$ | |
| #4: $(\mathrm{Ti}_x - \mathrm{O2}_x)^2(\mathrm{O1}_y - \mathrm{O3}_y)^2$ | #2: $(\mathrm{Ti}_y - \mathrm{O2}_y)^3$ |
| #5: $(\mathrm{Ti}_z[010] - \mathrm{O2}_z[010])(\mathrm{Ti}_z - \mathrm{O2}_z[010])(\mathrm{Ti}_y - \mathrm{O2}_y[010])$ | #5: $(\mathrm{Ti}_z - \mathrm{O1}_z)(\mathrm{Ti}_z - \mathrm{O3}_z[001])^2(\mathrm{Ti}_z - \mathrm{O3}_z)$ |
| #6: $(\mathrm{Sr}_x - \mathrm{O2}_x)^2(\mathrm{Sr}_z - \mathrm{O3}_z)$ | #7: $(\mathrm{Ti}_z[010] - \mathrm{O2}_z[010])(\mathrm{Ti}_z - \mathrm{O2}_z[010])(\mathrm{Ti}_y - \mathrm{O2}_y[010])$ |
| Strain-phonon coupling $E_{\rm sp}$ | |
| #1*: $\eta_2(\mathrm{O1}_x - \mathrm{O2}_x)(\mathrm{O1}_y - \mathrm{O2}_y)$ | #1*: $\eta_3(\mathrm{Ti}_z - \mathrm{O3}_z)^2$ |
| #2: $\eta_1(\mathrm{O2}_z - \mathrm{O3}_z[100])^2$ | #3*: $\eta_2(\mathrm{Sr}_x - \mathrm{O3}_x)^2$ |
| #3*: $\eta_4(\mathrm{Sr}_z - \mathrm{O1}_z)(\mathrm{Sr}_y - \mathrm{O1}_y)$ | #4: $\eta_1(\mathrm{O3}_y - \mathrm{O1}_y[010])^2$ |

This is also reflected in the sketch of Figure 3.13, showing also that important couplings involve usually both displacements and strains, i.e., the strain-phonon couplings. This is consistent with the known sensitivity of $SrTiO_3$ to strain deformations.

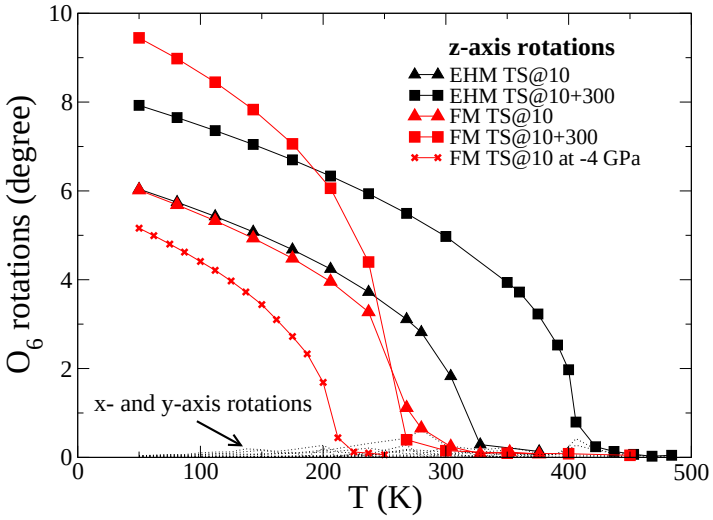


**Figure 3.14:** Computed evolution of the AFD order parameter, as a function of temperature, for the TS@10 and TS@10+300 models, and for the model fitted to TS@10 for which I applied an external negative pressure to correct LDA's overbinding character. Experimentally the transition is observed to occur at 105 K.

### 3.2.6 Simulation of $SrTiO_3$'s structural phase transition

One possible application of the models within the `SCALE-UP` framework is the study of the transition temperature of materials. In particular, since the models are fit to represent DFT data the results obtained are an approximation of the transition temperature that DFT would provide.

In this case I apply Metropolis Monte Carlo simulations to study in temperature a supercell of size $12 \times 12 \times 12$ containing 8640 atoms, with which one can produce good statistics for the analysis of the transition. Close to the transition I also increase the size of the cell to a repeated $16 \times 16 \times 16$ supercell containing 20480 atoms so that finite-size errors are reduced.

The MC simulations start from a quasi-thermalized configuration obtained through a 20 000 MC sweeps at a fixed temperature. Then, I add 40 000 MC sweeps to compute the statistical averages. I analyzed the results of the simulations to compute the expected value of the main order parameter, that in this case is the oxygen rotation angle. The results are shown in Figure 3.14.

The main feature indicating a phase transition is displayed in all the different models proposed, which coincides with the experimental observations. The rotation of the oxygen octahedra with respect one of the main axis of the cell decreases with temperature, reaching a zero angle at the transition point. After the transition, the order parameter is zero and the material's structure is that of the cubic cell (in average). The qualitative behavior of $SrTiO_3$ phase transition is well reproduced by all of the model potentials.

Discussing more in detail the results, one can connect the origin point of the curves to Table 3.6. This represents, at 0 K, the angle rotation predicted by the models, that as has been already discussed, is in almost perfect agreement for the case of models fitted to TS@10 with respect DFT.

The transition temperature varies greatly nonetheless amongst the different models. For example, for the models fitted to TS@10 the transition temperature is relatively low, in a range of temperatures between 260 K to 310 K, which is also the case for the FM model fitted to TS@10+300. It is however rather surprising to see that the EHM model fitted to TS10+300 displays a much higher phase transition temperature, close to 400 K. This is then a clear example that the amplitude of the distortions involved in the ground state does not necessarily lead to a particularly higher or lower phase transition temperature (as has been claimed in the past [81]). Instead, by inspecting the *depth* of the potential well, one finds that there may be a correlation between that energy difference and the transition. The deepest minimum appears for the EHM model fitted to TS@10+300, and the transition temperature is accordingly higher than in other cases. This rule has been claimed before in the literature [80] and is in agreement with the presented results.

Nevertheless, the predicted temperature for the structural transition of the material is considerably higher than the experimental result for all models presented. The lowest transition temperature predicted by the models (FM TS@10, 260 K) is much higher than the experimental result, which is about 110 K. Also, the rotation angle is highly overestimated (both from the models and from DFT) when compared to the experimental observation, which is around 2.1° at 4.2 K.

In order to see the impact of this, I used a common technique to prevent the problem of the overbinding character of LDA, which consists on defining a negative hydrostatic presure for the simulated cell that corrects, for the case of the cubic cell (i.e., the reference structure), the lattice parameters so that they match the experimental ones. In this case I applied -4.0 GPa, which is the highest negative pressure that I could apply mantaining the correct ground state of the material. By applying this negative pressure the angle in the ground state turned to be of 5.8° at 0 K, still considerably overestimating the experimental value. The computed phase transition temperature for this case is of 210 K, 50 K lower than that of the simulation without pressure. Hence applying this correction provides a better agreement towards the experimental observations.

This method is however not enough to reach the experimental values. It is natural then to conclude that there are further reasons for this to happen. An argument that is sound is that in the simulations performed I am not taking into account the lattice quantum effects. It is well accepted that such quantum fluctuations have a big impact in the phase transition temperature for materials like Strontium Titanate. The effect of including these usually result in a reduction of the transition temperatures *and* the distortion amplitudes [73, 82], because the material can accomodate the disorder in different ways. However, the estimated effects of quantum fluctuations are of about 15%, which would lead to a transition temperature of about 175 K, still quite above the experimental transition temperature.

### 3.2.7 Conclusions

Regarding the results presented the model FM fitted to TS@10 is the most reliable model, both at reproducing the DFT data and with respect the experimental results. The model EHM fitted to TS@10 has an almost equivalent behavior, with the addition of having better description of the phonons of the RS. Because of its completeness the EHM fitted to TS@10 is the model that I will use for STO studies later in the Manuscript.

Overall, the models comparison with experimental results is far from perfect. This could be improved by studying the addition of quantum fluctuations in the model. Also, exploring higher

order models could refine the reproduction of the PES, providing better performing models.

It is worth mentioning that, overall, the results obtained are clear: the models are reproducing well the DFT data. The error in the energies and the precision at the structure description are clear, particularily for the models fitted to TS@10. Thus it is possible that in order to obtain better models one would have to investigate different flavors of DFT potentials having better agreement with structures observed experimentally. An example would be to use of PBEsol within the Generalized Gradient Approximation (GGA) to produce the TS data, which is known to improve the overbinding occurring in LDA, to investigate the predicted transition temperature.

# Chapter 4

# Second-principles models of chemically-inhomogeneous materials

The formalism of SCALE-UP, summarized in Section 2.2, is a general theory applicable to any crystalline structure. So far in this Thesis I have explored the methodology behind model construction within this formalism, applied in practice to simple perovskite systems of the type $ABO_3$. The methodology is however general as well, and one can in principle apply it to generate a model for any kind of crystalline material provided two premises: i) one has the available training set data, and ii) the unit cell of the structural phase of the material used as reference structure is relatively small. The first constraint arises from the method itself, which uses DFT data to train and fit the model, and so one should be able to perform such simulations. As for the latter constraint, even though it is in principle possible to generate all possible terms of any order in any size of supercell, in practice the amount of terms scale with the size of the supercell in a way it quickly becomes computationally heavy to produce all terms of a big supercell. This strategy is condensed in panel (a) of Figure 4.1.

The generality of the formulation of SCALE-UP, combined with the model construction methodology developed in this Thesis, makes studying complex systems an enticing perspective. In particular I am interested in studying the applicability of the methods to chemically inhomogeneous perovskite compounds, in which either the $A$ or $B$ site may have different chemical elements throughout the supercell. I focus on the case of having chemical substitution at the crystallographic sites $A$. Hence, in general, I will refer to the system as $A'_{1-x}A''_xBO_3$ perovskite, indicating the composition variable $x$, or simply $A'A''BO_3$ to ease the notation.

This Chapter is organized as follows. First, in Section 4.1 I propose a general formalism that, in principle, allows to tackle the problematic of formulating a model for any type of chemically disordered perovskite. In particular, I present an approximative method to combine models of single perovskites into chemically inhomogeneous compounds. In Section 4.2 I present a general discussion on the method based on the application to different solid solutions of lead titanate and strontium titanate.

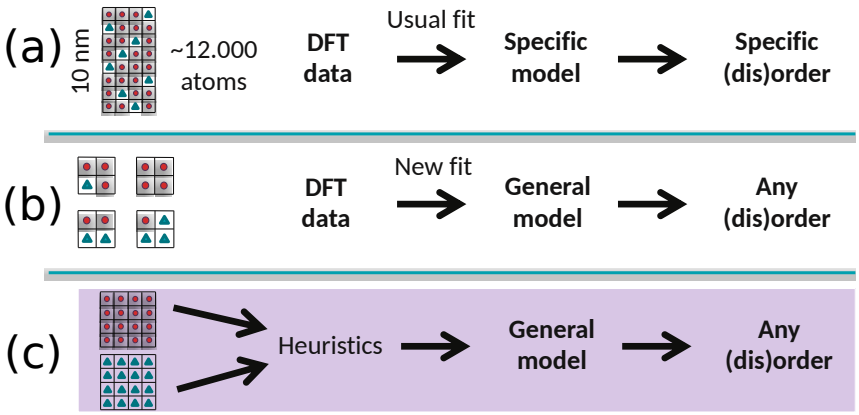


**Figure 4.1:** Sketch of different strategies to construct models for chemically inhomogeneous systems. **(a)** Apply the methodology described in Chapter 3 to fit a model of the chemically inhomogeneous compound. **(b)** Study different realizations of chemical disorder to construct a database of interactions depending on the chemical environment. **c)** Heuristically approximate the model of the chemically inhomogeneous system using models of the constituents as the starting point.

## 4.1 Formalism

### 4.1.1 Composition variables

Following the examples in the effective Hamiltonians literature [13] I will define a set of compositional variables that allows to describe a system with arbitrary chemical order. Also, I will elaborate on the formalism presented in Section 2.2.

In a cubic perovskite of the type $ABO_3$ the reference structure is chosen to be a cubic 5-atom cell, repeated periodically in space. For the atomic positions, $\boldsymbol{\tau}_\kappa$, the index $\kappa$ runs from 1 to the number of atoms in the unit cell, $N_{\text{cell}}$. In a chemically disordered system of the type $A'A''BO_3$ the $A$ sites of the lattice may be occupied either by $A'$ or $A''$ cations. The chemical order can be described using an Ising-like variable $\mu_{l_{\underline{\kappa}}}$, which defines which atom occupies the site $\mathbf{R}_l + \tau_{\underline{\kappa}}$. The index $\underline{\kappa}$ runs only in the sites at which chemical disordered may appear, thus in the example, it runs over the $A$ sites. The number of substitutional sites in the lattice will be referred to as $N_{\text{comp}}$ in the following development. Note that $\mu_{l_{\underline{\kappa}}} := 1$ if at site $\mathbf{R}_l + \tau_{\underline{\kappa}}$ there is an $A'$ atom; if the site is occupied by an $A''$ cation, then $\mu_{l_{\underline{\kappa}}} := 2$. The index notation will be simplified by using the bijective map $\underline{i} \leftrightarrow l_{\underline{\kappa}}$ in the following paragraphs.

### 4.1.2 General energy function

Compositional variables allow to distinguish the type of cation occupying the chemical disordered site. In particular, the Ising-like variable is a discrete function of the site and permits to rewrite the energy function as a functional of the sites.

The energy in SCALE-UP model potentials depends on the composition functionally:

$$E[\boldsymbol{\mu}](\mathbf{u}, \boldsymbol{\eta}) = E_{\text{RS}}[\boldsymbol{\mu}] + E_{\text{p}}[\boldsymbol{\mu}](\mathbf{u}) + E_{\text{s}}[\boldsymbol{\mu}](\boldsymbol{\eta}) + E_{\text{sp}}[\boldsymbol{\mu}](\mathbf{u}, \boldsymbol{\eta}). \tag{4.1.1}$$

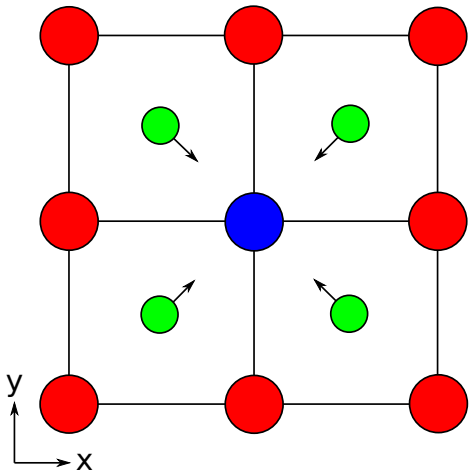


**Figure 4.2:** Depiction of four cells in the $xy$ plane. The red atoms are of $A'$ type and the blue central atom is of $A''$ type. The green atoms represent the oxygens coplanar to the $A$ sites. The arrows indicate the forces that may apply on the oxygens if they have more chemical affinity with $A''$ species than $A'$ species.

Here, the label of the energy contributions remains the same as in 2.2, and $\boldsymbol{\mu} = \{\mu_i\}$. The dependency is made explicit through the formulation of the different energy contributions, where the coefficients of the terms are rewritten to have a tensorial form. For $E_{\rm p}$ the energy is written as

$$E_{\rm p}[\boldsymbol{\mu}](\mathbf{u}) = \sum_{ij\alpha} \mathcal{K}^{(1)}_{ij\alpha}[\boldsymbol{\mu}](u_{i\alpha} - u_{j\alpha}) + \frac{1}{2} \sum_{ij\alpha kh\beta} \mathcal{K}^{(2)}_{ij\alpha kh\beta}[\boldsymbol{\mu}](u_{i\alpha} - u_{j\alpha})(u_{k\beta} - u_{h\beta}) + \dots \tag{4.1.2}$$

Note that $\mathcal{K}^{(n)}[\boldsymbol{\mu}]$ depends now on the chemical order. That is to say, the form of $\tilde{K}^{(n)}$ in 2.2.14 is now rewritten, so that it depends on the chemical species occupying the lattice, which are described in the equation above using latin the labels $i, j, ....$

The rest of the energy terms are similarily adapted. The elastic part of the energy is written as

$$E_{\rm s}[\boldsymbol{\mu}](\boldsymbol{\eta}) = N \sum_a C^{(1)}_a[\boldsymbol{\mu}]\eta_a + \frac{N}{2} \sum_{ab} C^{(2)}_{ab}[\boldsymbol{\mu}]\eta_a\eta_b + \dots \tag{4.1.3}$$

Finally, for the strain-phonon coupling terms one can write

$$E_{\rm sp}[\boldsymbol{\mu}](\mathbf{u}, \boldsymbol{\eta}) = \sum_a \sum_{ij\alpha} \mathcal{L}^{(1,1)}_{aij\alpha}[\boldsymbol{\mu}]\eta_a(u_{i\alpha} - u_{j\alpha}) + \frac{1}{2} \sum_a \sum_{ij\alpha kh\beta} \mathcal{L}^{(1,2)}_{aij\alpha kh\beta}[\boldsymbol{\mu}]\eta_a(u_{i\alpha} - u_{j\alpha})(u_{k\beta} - u_{h\beta}) + \dots \tag{4.1.4}$$

The most notorius difference between the original SCALE-UP formulation and its adaptation to chemically inhomogeneous systems is the appearence in the latter of linear terms. The reason is that, in contrast to the case of single $ABO_3$ perovskite systems, the cubic phase of the RS is no longer a critical point of the potential energy surface. The reason is that due to chemical disorder the reference structure may not be compliant with the cubic symmetry; an example is sketched in Figure 4.2.

In the sketch, the change in the chemistry induced by the substitution of the central cation of the layer induces a force in the oxygen atoms, which without loss of generality have been chosen to have more affinity towards the central atom. Similarily, the chemical order has an impact on the

strains of the cell, that may relax to provide a different volume of the cell. This indicates a residual stress, arising from linear terms in the elastic energy.

As well as with the short-range and elastic energy terms described above, the dipole-dipole interactions appearing in insulator or semiconductor materials may be adapted to chemically disordered systems. In general, the tensorial character arises in this case at the definition of the Born effective charges $Z^*_{i\alpha\beta}[\boldsymbol{\mu}]$ and the effect on the global dielectric tensor $\epsilon_\infty$. The treatment of this part of the energy will be described further in the text.

As a final remark, the formulation presented here suggests already a way to proceed in model creation. It would be in principle possible to create a database of tensors $\mathcal{K}^{(n)}[\boldsymbol{\mu}^{\boldsymbol{d}}], \mathcal{L}^{(n)}[\boldsymbol{\mu}^{\boldsymbol{d}}]$, where $d$ labels different realizations of chemical order (this is summarized in panel (b) of Figure 4.1).

### 4.1.3 Model mixing

Instead of tackling the problem as described in the paragraph above I present a much lighter, physically-motivated approach, in which I assume that the constituents of the chemically inhomogeneous perovskite ($A'BO_3$ and $A''BO_3$) exist separately [20, 21]. The premise of it is that one has the models of the systems $A'BO_3$ and $A''BO_3$, that I will refer to as pure models in the following paragraphs (see panel (c) of Figure 4.1). Using the information already available in the models, and assuming that the chemical properties of the atoms involved in both compounds are relatively similar, I propose an approximative method to heuristically obtain the interactions appearing in the $(A'A'')BO_3$ perovskite system. The recipe may be applied to an arbitrary realization of the chemical order $\boldsymbol{\mu}$.

The idea behind this approach is the perspective on materials design, which can range from the study of superlattices to the analysis of the behavior of clustered materials or nanocomposites. In these examples one investigates a superstructure of materials for which the constituents exist as pure materials, but allowing to tune its properties or engineer new applications for device design. It is observed that the lattice-dynamical properties of such complex structures depend essentially on the electric and elastic constraints that the constituents exert on each other, the details of the interface being secondary [83–85]. Since the technology developed in this Manuscript allows for the construction of pure models, it is then natural to attempt to study chemically disordered systems from this perspective.

#### The description of the chemical environment

The chemical order variable $\boldsymbol{\mu}$ describes the superlattice atomic arrangement of the system. In order to write specific forms of the $\mathcal{K}^{(n)}[\boldsymbol{\mu}], \mathcal{L}^{(n)}[\boldsymbol{\mu}]$ and $C^{(n)}[\boldsymbol{\mu}]$ tensors as a function of the original terms of the pure models one has to be able to describe the chemical environment of the atoms.

Let $\mathcal{N}_i$ denote the set of nearest neighbors of atom $i$ in the lattice. The chemical environment of the atom can be then quantified through

$$n_{i,c} = \sum_{\underline{i}\in\mathcal{N}_i} \delta_{\mu_{\underline{i}},c}. \tag{4.1.5}$$

Note that the sum runs only for the nearest-neighboring $A$ sites (in general, any neighboring site susceptible of chemical substitution). The label $c$ can take the same values as the compositional variables, thus either 1 or 2. Thus the value $n_{i,c}$ is the number of atoms of type $c$ neighboring the atom $i$. The total number of neighboring substitutional atoms to atom $i$ can then be straightforwardly computed by

$$n_i = \sum_c n_{i,c}, \tag{4.1.6}$$

which allows to define the chemical character of the environment of atom i through

$$p_{i,c} = \frac{n_{i,c}}{n_i}. \tag{4.1.7}$$

The values of $p_{i,c}$ indicate the $c$ character of the environment. For the case of the $A'A''BO_3$ perovskite, $p_{i,1}$ tells how similar is the local environment to that of $A'BO_3$, analogously for $c = 2$. Also, in this case

$$p_{i,1} = 1 - p_{i,2}. \tag{4.1.8}$$

The nearest neighboring atoms are the nearest neighbors up to the substitutional sites. The $B$ cations have as first neighbors the 6 oxygen octahedra, and as second neighbors the 8 $A$ cation sites. Hence, $n_{i,c}$ runs only up to the first neighboring $A$ cation sites, and thus this is the only contribution for the calculation of $p_{i,c}$. On the other hand, oxygens have 4 $A$ cation sites as first neighbors, which describe the chemical environment of each oxygen. As for the nearest neighbors of $A$ cations one can account for 8 cations of type $B$ and a cage of 12 oxygens, leaving $p_{\underline{i},c}$ ill defined. For this particular case I chose $p_{\underline{i},c} = \delta_{c,\mu_{\underline{i}}}$. In other words, in the approximation the cations $A'$ are understood to have a chemical environment of the pure $A'BO_3$ type.

### Approximations for $E_{\mathbf{p}}$

The chemical environmental variables allows to describe now an approximation for the values of the tensor $\mathcal{K}^{(n)}[\boldsymbol{\mu}]$. I will refer in the following to $\tilde{K}^{(n),c}$ as the parameters of the $E_{\mathrm{p}}$ energy part of the pure model type $c$.

Let us first consider the interactions between atoms not affected by chemical substitution (i.e., $B$ and O in the example). The coupling terms can then be written as

$$\mathcal{K}^{(n)}_{ij\alpha kh\beta\ldots} \approx \frac{1}{2n} \sum_c \tilde{K}^{(n),c}_{ij\alpha kh\beta\ldots}(p_{i,c} + p_{j,c} + p_{k,c} + p_{h,c} + \ldots), \tag{4.1.9}$$

where the normalization factor $(2n)^{-1}$ accounts for the number of bodies involved in the calculation of the parameter.

This approximation is particularily adequate to describe clustering in materials, as for locally homogeneous chemical compositions the pure model couplings are recovered. For regions with local inhomogeneity, the expression will in a way interpolate the interactions of the pure models. As in perovskites the short-range interactions do not depend strongly on the chemical environment [23] a simple weighted averaging method is justified.

It is possible that particular interactions appear in one of the pure models, but not in the other. In this case I have chosen to set the parameter of the model that does not have the interaction to zero, and so the interaction will still appear in the mixed system, however weakened.

The interactions involving $\underline{i}$ atoms have been chosen to retain the original coefficient of the pure models without any modification.

As a final remark, note that the formulation proposed is written in terms of differences of displacements. It is then also explicitely compliant with the acoustic sum rule, allowing to manage the averaging of the coefficients without requiring any correction. This is a major advantage of the formulation.

### Approximations for $E_{\mathbf{sp}}$

The approach for obtaining the tensors $\mathcal{L}^{(m,n)}$ is equivalent as the described in the paragraphs above. The information available in the pure models allows to write to write

$$\mathcal{L}^{(m,n)}_{ab\ldots ij\alpha kh\beta\ldots} \approx \frac{1}{2n}\sum_{c}\tilde{\Lambda}^{(m,n),c}_{ab\ldots ij\alpha kh\beta\ldots}(p_{i,c}+p_{j,c}+p_{k,c}+p_{h,c}+\ldots) \tag{4.1.10}$$

for interactions involving atoms not affected by chemical substitution.

Similarily to the approximations for $E_{\mathrm{p}}$ interactions involving $\underline{i}$ atoms retain their respective coefficients, and interactions $A'-A''$ are not considered.

### Approximations for $E_{\mathbf{s}}$

The macroscopic elastic constants $C^{(m)}[\boldsymbol{\mu}]$ depend on the chemical composition. For example, in a superlattice geometry, in general the stiffness along the stacking axis will depend on the softer compound, whereas the stiffness of the in-plane axes will be controlled by the harder compound. In contrast, in a solid solution the elastic constants will likely tend to the average of the elastic constants of the isolated compounds.

The elastic constants $E_s$ can be derived in principle from interatomic couplings in $E_p$ by inspecting the energetics of long wavelength acoustic modes. However, tests I performed using DFT reveal that the convergence is slow in space. In order to obtain accurate values for the elastic constants the DFT calculations suggest that one needs a good description of short-range interactions well beyond the interaction distance cutoff typically described in the SCALE-UP model potentials. As a consequence I will not implement this calculation here, but instead use the developed theory tackling the mecanical properties of alloys to introduce a simple but effective approximation [86, 87].

Let us define the chemical $c$-character of cell $l$ through

$$n_{l,c} = \sum_{\underline{\kappa}}\delta_{\mu_{l\kappa},c}. \tag{4.1.11}$$

Then, similarily to the definition of the chemical environmental fractional character, one can define

$$p_{l,c} = \frac{n_{l,c}}{N_{\mathrm{comp}}}. \tag{4.1.12}$$

The elastic constants of cell $l$ can be defined then as

$$C^{(m)}_{\alpha\beta\gamma\lambda\ldots}(l) = \sum_{c} p_{l,c}C^{(m),c}_{\alpha\beta\gamma\lambda\ldots}, \tag{4.1.13}$$

where $C^{(m),c}$ denote the elastic tensors of the constituent $c$ pure model. As a note, the notation of the elastic constants here described is in a Cartesian form, opposed to the usual Voigt notation used in this Manuscript.This will be convenient in the following paragraphs.

Let us begin the discussion on the calculation of the elastic tensor by focusing on $C^{(2)}_{\alpha\alpha\alpha\alpha}[\boldsymbol{\mu}]$. This coefficient describes the quadratic response of the strain applied in the $\alpha$ direction, $\eta_{\alpha\alpha}$. The cells of a given plane orthogonal to $\alpha$ are clamped, and thus have a shared response to any applied strain. It is then sound to assume that the elastic response of the layer will be that of the average of its constituent cells,

$$C^{(2)}_{\alpha\alpha\alpha\alpha}(l_\alpha) \approx \frac{N_\alpha}{N} \sum_{l/l_\alpha} C^{(2)}_{\alpha\alpha\alpha\alpha}(l). \tag{4.1.14}$$

The average elastic constants are then computed for all $\alpha$-planes, which are indexed by $l_\alpha$. The sum runs over $l$ cells within the $l_\alpha$-th $\alpha$-plane. Note that $N/N_\alpha$ is the number of cells contained in each $\alpha$-plane, i.e., the total number of cells divided by the total number of planes.

In order to calculate the the global $C^{(2)}_{\alpha\alpha\alpha\alpha}$ response one can imagine that the different planes discussed above are linked in series, each plane representing a string. Then, one can use the inverse sum rule to calculate the overall response,

$$\frac{1}{C^{(2)}_{\alpha\alpha\alpha\alpha}} \approx \frac{1}{N_\alpha} \sum_{l_\alpha} \frac{1}{C^{(2)}_{\alpha\alpha\alpha\alpha}(l_\alpha)}, \tag{4.1.15}$$

properly accounting for the number of planes $N_\alpha$. This expression gives importance to the potential difference of elasticity between layers, in which the overall response will be necessarily more dependent on the behavior of the softer planes.

Using an equivalent logic one can derive the rest of the elastic tensor coefficients approximations. I discuss here the cases of the coefficients that are independent and non-zero for the cubic reference structure symmetry. These coefficients, appart from the one discussed already above, are $C^{(2)}_{\alpha\alpha\beta\beta}$ and $C^{(2)}_{\alpha\beta\alpha\beta}$, for $\alpha \neq \beta$.

For $C^{(2)}_{\alpha\alpha\beta\beta}$ I consider the intersection between the $\alpha$ and $\beta$ planes and apply a similar approach to that of Eq. 4.1.14:

$$C^{(2)}_{\alpha\alpha\beta\beta}(l_\alpha, l_\beta) \approx \frac{N_\alpha N_\beta}{N} \sum_{l/(l_\alpha,l_\beta)} C^{(2)}_{\alpha\alpha\beta\beta}(l). \tag{4.1.16}$$

The inverse sum rule is then applied to the collection of values for the different intersections of $\alpha$ and $\beta$ planes,

$$\frac{1}{C^{(2)}_{\alpha\alpha\beta\beta}} \approx \frac{1}{N_\alpha N_\beta} \sum_{l_\alpha l_\beta} \frac{1}{C^{(2)}_{\alpha\alpha\beta\beta}(l_\alpha, l_\beta)}. \tag{4.1.17}$$

The shear elastic constants are computed similarily. First,

$$C^{(2)}_{\alpha\beta\alpha\beta}(l_\alpha, l_\beta) \approx \frac{N_\alpha N_\beta}{N} \sum_{l/(l_\alpha,l_\beta)} C^{(2)}_{\alpha\beta\alpha\beta}. \tag{4.1.18}$$

Then the inverse sum rule over the $\alpha$ and $\beta$ planes intersection provides the final form of the elastic components,

$$\frac{1}{C^{(2)}_{\alpha\beta\alpha\beta}} \approx \frac{1}{N_\alpha N_\beta} \sum_{l_\alpha l_\beta} \frac{1}{C^{(2)}_{\alpha\beta\alpha\beta}(l_\alpha l_\beta)}. \tag{4.1.19}$$

In the SCALE-UP model potentials typically the elastic energy is expanded up to harmonic order. The adaptations of the expressions above to higher orders is not trivial, but because of the choice of the expansion cutoff, this has no impact in the present work.

### Approximations for the electrostatic interaction

In the formulation of SCALE-UP model potentials the $E_{\mathrm{p}}$ energy contribution is divided into the short-range interaction contribution and the long-range electrostatic energy. The latter, which has a major role when describing the energetics of insulator or semiconductor materials, is in nature of infinite range. In the formulation of the models this interaction is described up to harmonic order, and I present in the following paragraphs a simple approach to obtain an approximative electrostatic interaction suitable for mixing models.

Let us first start by writing the equations in Section 2.2 using the compositional variables introduced at the beginning of this Chapter. The dipole-dipole harmonic interaction is written

$$E_{\mathrm{p}}^{\mathrm{lr}}[\boldsymbol{\mu}] = \frac{1}{2}\sum_{i\alpha j\beta} \mathcal{K}^{(2),\mathrm{lr}}_{i\alpha j\beta}[\boldsymbol{\mu}] u_{i\alpha} u_{j\beta} \tag{4.1.20}$$

where the dependence on the contribution is made explicit through the electrostatic harmonic interaction describing the couplings,

$$\mathcal{K}^{(2),\mathrm{lr}} = \sum_{\gamma\delta} Z^*_{i\alpha\gamma}[\boldsymbol{\mu}] Z^*_{j\beta\delta}[\boldsymbol{\mu}] \left( \frac{((\epsilon_\infty)^{-1})_{\gamma\delta}}{(D[\boldsymbol{\mu}])^3} - \frac{3\Delta_\gamma[\boldsymbol{\mu}]\Delta_\delta[\boldsymbol{\mu}]}{(D[\boldsymbol{\mu}])^5} \right) (\det \boldsymbol{\epsilon}_\infty[\boldsymbol{\mu}])^{-1/2}. \tag{4.1.21}$$

where the effective Born charges and the dielectric permittivity tensor, as well as the derived quantities $D$ and $\Delta$ (for which the definion can be found in Eqs. 2.2.21) depend now on the compositional variables of the material.

The task of approximating $\mathbf{Z}^*_i[\boldsymbol{\mu}]$ and $\boldsymbol{\epsilon}_\infty$ is very difficult, and likely, the origin of quantitative inaccuracy in the model mixing. One could attempt to approximate this interaction in a similar way as the one proposed for the approximation of the elastic energy, which would capture anisotropy in the atomic arrangement and related effects. However, the electrostatic problem is actually much more challenging, as ultimately the goal is to describe the screened interactions between dipoles in an inhomogeneous (or nanostructured) medium, where the atomic details can play a role.

For the moment, here I ignore these complexities, and I apply a scheme that has been applied in the literature in the study of $PbTiO_3/SrTiO_3$ superlattices, showing good reproduction of the basic electrostatic effects occurring in such materials, and which is also following the spirit of similar approximations in the effective Hamiltonians literature [13].

Let us begin by approximating the dielectric permitivitty tensor as the average quantity

$$\boldsymbol{\epsilon}_\infty \approx \sum_c p_c \boldsymbol{\epsilon}^c_\infty, \tag{4.1.22}$$

where $\boldsymbol{\epsilon}^c_\infty$ is the dielectric permitivity tensor associated with the compound $c$ and $p_c$ is the ratio of the compound $c$ in the mixture, with $\sum_c p_c = 1$. This expression for the dielectric permittivity tensor follows the assumption that the way in which distant dipoles interact in the compound

depends on the global composition and not on how the substitutional atoms are arranged in the cell.

Going back to Eq. 4.1.21, the role of locally describing the richness of the electrostatic interaction can be given to the effective charges. Let us assume that $\boldsymbol{\epsilon}_\infty$ is isotropic, which is the case in the cubic reference structures used for the pure models - then, the dielectric permittivity tensor can be described using one number, that I will refer to as $\varepsilon^c_\infty$. Since $\boldsymbol{\epsilon}^c_\infty$ is isotropic, so it will be $\boldsymbol{\epsilon}_\infty$; then one can write $\boldsymbol{\epsilon}_\infty = \varepsilon_\infty \mathbf{Id}_3$. I define

$$\mathbf{Z}^*_i \approx \sum_c p_{i,c} \sqrt{\frac{\varepsilon_\infty}{\varepsilon^c_\infty}} \mathbf{Z}^{*,c}_i, \tag{4.1.23}$$

where $\mathbf{Z}^{*,c}_i$ is the effective charge of atom $i$ of the pure compound $c$. By reintroducing this into Eq. 4.1.21 it is trivial to prove that the pure model electrostatic is recovered due to the factor $p_{i,c}$, which measures the chemical environment. Although it is true that this may affect the interaction of distant dipoles, in the studies performed using this approach this has not had a significant impact.

The chosen approximation for the effective charges is compliant with the neutrality of the cell and the acoustic sum rule, meaning that a rigid displacement does not create electrical dipoles. In the pure materials this rule can be written as

$$\sum_i Z^{*,c}_{i\alpha\beta} = \sum_l \sum_\kappa Z^{*,c}_{\kappa\alpha\beta} = 0 \quad \forall \alpha, \beta. \tag{4.1.24}$$

When using the average effective charges one can then write

$$\sum_i \mathbf{Z}^*_i = \sum_c \sqrt{\frac{\varepsilon_\infty}{\varepsilon^c_\infty}} \sum_i p_{i,c} \mathbf{Z}^{*,c}_i, \tag{4.1.25}$$

where

$$\sum_i p_{i,c} \mathbf{Z}^{*,c}_i = \sum_i \sum_{\underline{i} \in \mathcal{N}_i} \frac{\delta_{i,c}}{n_i} \mathbf{Z}^{*,c}_i = \sum_{\underline{i}} \delta_{\underline{i},c} \sum_{i \in \mathcal{N}_{\underline{i}}} \frac{1}{n_i} \mathbf{Z}^{*,c}_i. \tag{4.1.26}$$

Here, $\mathcal{N}_{\underline{i}}$ is the set of neighbors of atom $\underline{i}$ that are affected by its presence. One then has

$$\sum_{i \in \mathcal{N}_{\underline{i}}} \frac{1}{n_i} \mathbf{Z}^{*,c}_i = \sum_{l\kappa \in \mathcal{N}_{\underline{i}}} \frac{1}{n_\kappa} \mathbf{Z}^{*,c}_\kappa = \sum_\kappa \mathbf{Z}^{*,c}_\kappa = 0. \tag{4.1.27}$$

As an observation, every $\kappa$-atom appears exactly $n_\kappa$ times in the sum over $i \leftrightarrow l\kappa$, which leads to the final result.

### The approximative Reference Structure

The calculation of the dipole-dipole interactions in the SCALE-UP model potentials takes explicitly into account the definition not only of the atomic positions but also the lattice vectors, as can be seen from Equation 4.1.21. For this reason, it is necessary to provide an explicit form of the RS.

The RS of the mixed models is chosen to be a weighted average of the RS's of the models mixed. This correspond to a cubic homogeneous lattice, defined by a periodically-repeated cell of 5 atoms, and characterized by a single lattice parameter that we can compute as the weighted average of

the corresponding RS lattice constants of the constituent compounds. For example, for the case of a cubic lattice we can estimate an average elastic constant $a^{\text{avg}}$ by minimizing the energy

$$E = \frac{p_1 C_1}{2}\left(\frac{a^{\text{avg}} - a_1}{a_1}\right)^2 + \frac{p_2 C_2}{2}\left(\frac{a^{\text{avg}} - a_2}{a_2}\right)^2 \tag{4.1.28}$$

where $a_c$ and $C_s$ are the cell parameter of the cubic RS and the diagonal elastic constant ($C_{11} = C_{22} = C_{33}$ in Voigt notation) of the $c$-compound, respectively; also, $p_c$ is the ration of $c$-compound in the mixture. By solving for $a^{\text{avg}}$, one obtains

$$a^{\text{avg}} = a_1 a_2 \frac{m a_1 + a_2}{m a_1^2 + a_2^2} \tag{4.1.29}$$

with

$$m = \frac{p_2 C_2}{p_1 C_1}. \tag{4.1.30}$$

This way of averaging takes into account the stiffness of the materials. For example, for very stiff materials in which $C_2 \gg C_1$ it follows that $a^{\text{avg}} \approx a_2$.

Note also that, with my choices of reference structure and mixing of model parameters, I am effectively assuming that the RS of the mixed model somehow *includes* composition-dependant relaxations, so that it is a singular point of the PES. Indeed, the pure models do not have linear terms nor the mixed models. This may be an impactful approximation; in order to improve on this aspect one would need to develop a scheme of the type of panel (b) in Figure 4.1.

## 4.2 Example of application: mixtures of lead titanate and strontium titanate

In this Section I explore the impact of the approximations proposed in the formalism and the results that one can obtain with this simple approach. The models used for this application are the EHM@10 produced in Chapter 3 for strontium titanate and a model for lead titanate constructed in the same way. Both models are built using DFT data calculated using LDA.

I also examine the case of $(\text{PTO})_n/(\text{STO})_n$ superlattices. To improve the reproducibility of experimental and theoretical results in the literature I have chosen to generate also models using the Generalized Gradients Approximation (GGA), in particular using pseudopotentials generated using the theory of Perdew-Burke-Ernzerhof for solids (also known as PBEsol). This theory provides a better description of the lattice parameters, which for the particular materials STO and PTO matches remarkably the experimental observations.

Several choices of mixtures are proposed for the studies, sketched in Figure 4.3. In the different sketches only the $A$ cations are depicted, and the dashed lines are only a guideline for the eye. Each $A$ cation is in practice representing a 5-atom unit cell, although the oxygen and titanium atoms have been left out of the sketch for clarity.

The structures proposed vary in % of composition and the labels assigned are explicative of the way in which this happens. For example, I consider cases that are similar to the pure compounds except for one defect (7Pb1Sr, which is compositionally close to PTO, and 1Pb7Sr, which is close

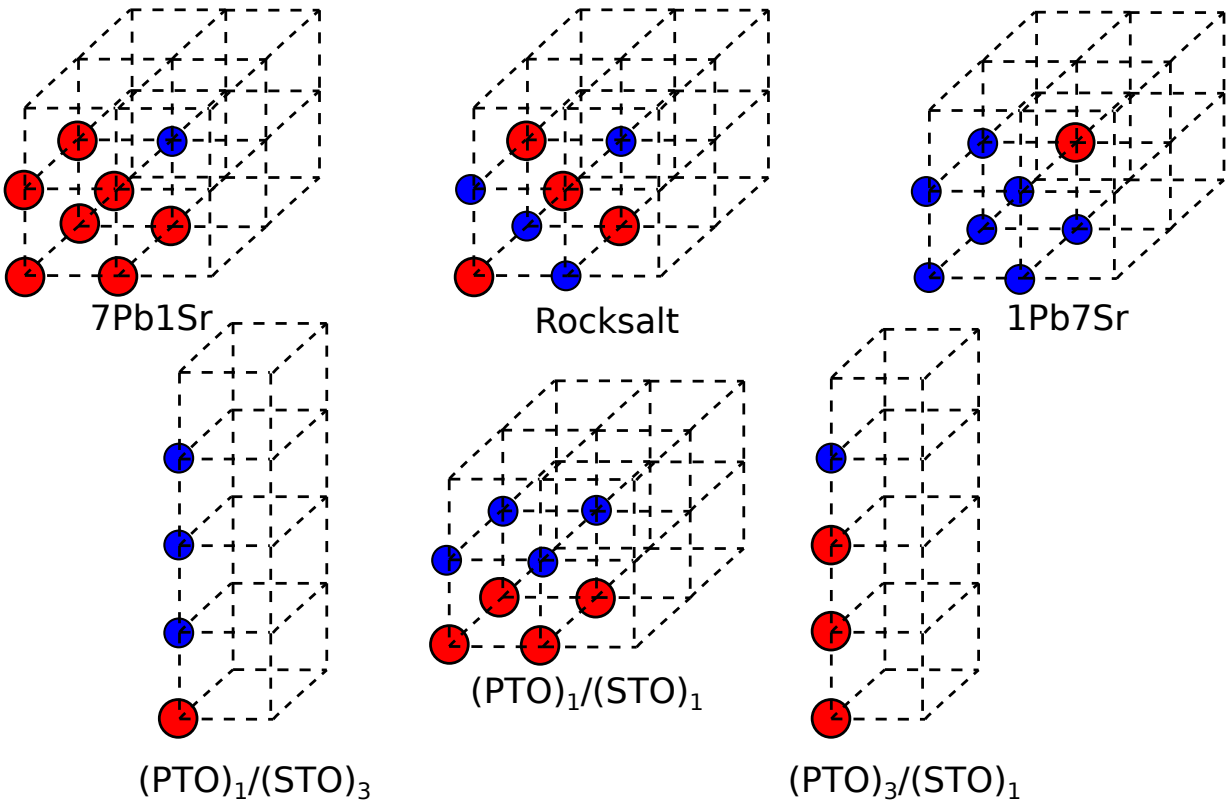


**Figure 4.3:** Depiction of the different mixtures considered of $SrTiO_3$ and $PbTiO_3$. In the sketches, red circles represent Pb atoms and blue circles refer to Sr cations (see text for further description of the cases).

to STO), and heavily mixed cases like the Rocksalt mix type. I also consider layered compositions of different kinds: the cases of $(PTO)_3/(STO)_1$ and $(PTO)_1/(STO)_3$ represent superlattices in which one of the pure materials is predominant, while the superlattices $(PTO)_1/(STO)_1$ and $(PTO)_2/(STO)_2$ are limit cases of a 50/50 mixture in which the chemistry is different at each layer. A different realization of the 50/50 mixture is the case of the Rocksalt, for which the atomic species is changed for every first neighbor of a cation $A$. Rocksalt and $(PTO)_1/(STO)_1$ represent the critical cases in which the approximation may have larger impact. The sketched cells represent the supercell simulated, and thus the structures are repeated by means of periodical boundary conditions throughout space.

### 4.2.1 Study of the force constant matrices

The first comparative study I perform on the samples is regarding the character of the eigenvalues and eigenvectors of the force-constant matrix at the RS of the different mixtures. This is equivalent (by a factor of the mass of the atoms) to a study of the phonons of the material, in this case, on the reference structure. By observing this one can study the main structural instabilities that the material may display. With this one can measure the quality of the approximations for the $E_{\text{p}}$ energy contribution up to the harmonic order.

The force-constant matrices are obtained using finite displacements for the second derivatives, both using the mixed models and DFT. For the DFT calculations I first calculate the relaxed atomic positions of the structures using the cubic-like perovskite structure as the starting configuration.

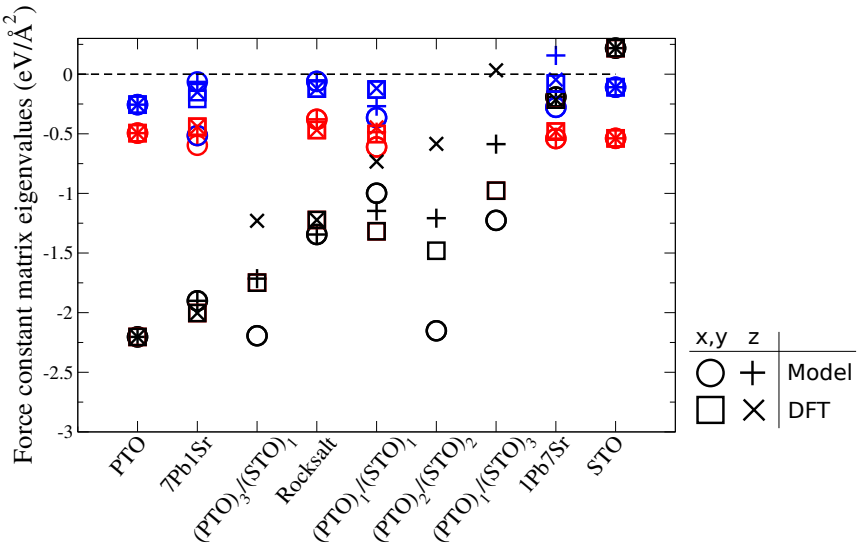


**Figure 4.4:** Eigenvalues of the force-constant matrices of the different mixtures considered (see Figure 4.3). Only the eigenvalues corresponding to the FE mode (black symbols) and oxygen octahedra rotation modes (AFD in anti-phase in red; AFD in-phase in blue) are displayed.

By doing so the linear terms of the energy arising from chemical symmetry breaking vanish. In the case of the mixed models I use the cubic-like structure, following the assumptions of Section 4.1.3.

The results are shown in Figure 4.4. At first glance, the reproduction of the eigenvalues corresponding to either anti-phase or in-phase rotation modes of the oxygen octahedra are overall both qualitatively and semi-quantitatively accurate. The impact of the averaging of the short-range interactions between the two pure models can be observed: the structures have been ordered from left to right from PTO-like to STO-like, and in a way, the mixed models interpolate the pure model results.

Both the AFD and polar distortions are overall well behaved, with some exceptions in the superlattice cases. For the cases of $(PTO)_3/(STO)_1$ and $(PTO)_1/(STO)_3$ are the ones that deviate the most with respect the DFT calculated values. For the $(PTO)_1/(STO)_1$ superlattice I observe as well that the character of the instabilities is not respected. Let us call $\lambda_{P_\alpha}$ the eigenvalue of the mode corresponding to a polar distortion in the $\alpha$ Cartesian direction. For the predicted force-constant matrix eigenvalues by the model one has $\lambda_{P_z} < \lambda_{P_x} = \lambda_{P_y}$, while the results from DFT are the opposite.

I have further researched the origin of this surprising result. First, I observe that when computing the eigenvalues of the force-constant matrics of larger superlattices, for example $(PTO)_2/(STO)_2$, the correct behavior is recovered, obtaining $\lambda_{P_x} = \lambda_{P_y} = -2.2$ eV/Å$^2$ and $\lambda_{P_z} = -1.2$ eV/Å$^2$ (see panel (a) of Figure 4.5). The main difference in this calculation is that within the layers the short-range interactions of the original models are recovered, as opposed to the cases presented before. Hence, the case of $(PTO)_1/(STO)_1$ is a more challenging case.

Also, when looking at the electrostatics there is a noticeable difference between the mixed models and the DFT calculations: for superlattice-like structures, the dielectric permittivity of the material is not isotropic, as a contrast with the dielectric permittivity used in the models which

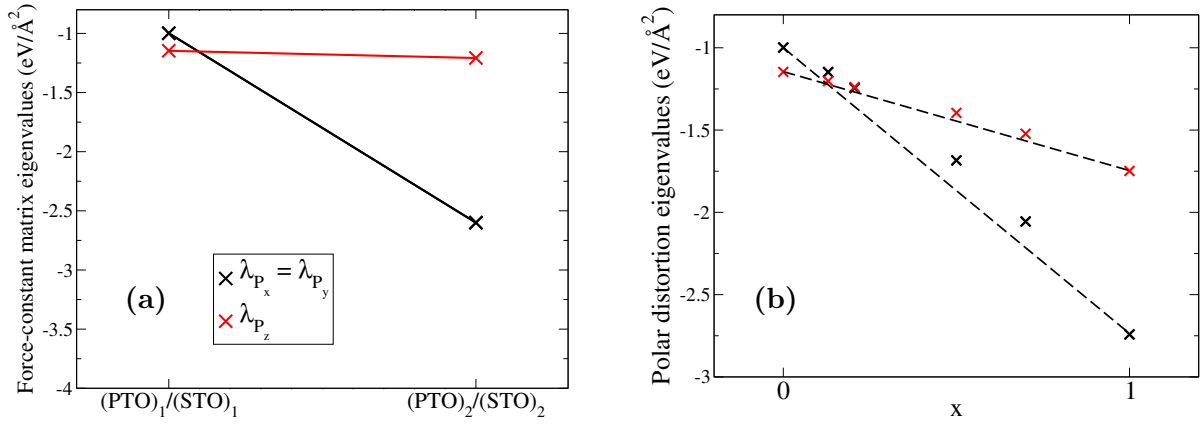


**Figure 4.5:** Study of the eigenvalues of the polar distortion of the $(PTO)_n/(STO)_n$ superlattices. **(a)** Eigenvalues of $(PTO)_1/(STO)_1$ and $(PTO)_2/(STO)_2$, showing that the correct behavior is recovered for thicker layers. **(b)** Study of the impact of the values of $\epsilon_\infty$ on the ferroelectric instabilities of $(PTO)_1/(STO)_1$. The legend for both panels is the same.

results from a simple averaging. Let us focus on the case of the $(PTO)_1/(STO)_1$ superlattice. The dielectric permittivities of the model and the calculation using DFT reads

$$\epsilon_\infty^{\text{model}} = \epsilon_0 \begin{pmatrix} 7.6 & 0 & 0 \\ 0 & 7.6 & 0 \\ 0 & 0 & 7.6 \end{pmatrix} \qquad \epsilon_\infty^{\text{DFT}} = \epsilon_0 \begin{pmatrix} 7.2 & 0 & 0 \\ 0 & 7.2 & 0 \\ 0 & 0 & 7.0 \end{pmatrix} \tag{4.2.1}$$

The anisotropy of the dielectric tensor as computed using DFT is a clear candidate of being responsible for the behavior observed in the study of the force-constant matrix eigenvalues. In order to investigate this, I have used the results of $\epsilon_\infty^{\text{DFT}}$ in the model, which leads to the correct (however exagerated) behavior of the eigenvalues.

In panel (b) of Figure 4.5 I show the evolution of the eigenvalues when varying the dielectric tensor using a standard interpolation of the kind

$$\epsilon_\infty = \epsilon_\infty^{\text{model}} + k(\epsilon_\infty^{\text{DFT}} - \epsilon_\infty^{\text{model}}), \tag{4.2.2}$$

to calculate the dielectric permittivity of the model. As can be seen, the character changes throughout the interpolation. The crossover occurs for $k \approx 0.206$.

This result supports the idea that further development in the electrostatic approximations could lead to a better agreement between the mixed models and DFT calculations.

### 4.2.2 Comparison of the elastic properties

The results of the approximation of the elastic constants is displayed in Table 4.1. The elastic constants of lead titanate and strontium titanate are relatively similar, and numerically one could not expect a major deviation in the calculation of the averages.

The introduction of potential anisotropies in the elastic coefficients by the approach described in the formulation appears in several of the cases studied, although the difference is tiny due to

the numerical proximity of values and in most cases is beyond the significative figures shown, with the exception of the superlattice $(PTO)_1/(STO)_1$ and $(PTO)_1/(STO)_3$. Notably, the coefficients predicted are both qualitative and quantitatively close to the DFT results.

Thus one can conclude that the approximation is a good choice in most cases, and up to the harmonic order, the proposed mixed models have a good description of the elastic properties of the mixtures.

### 4.2.3 Model ground state structures

The models for the different mixtures studied offer the possibility of inspecting the ground state structures. As with any SCALE-UP model potentials one can use Monte Carlo simulations through the Metropolis algorithm to minimize the energy with respect the atomic displacements and the strains of the cell.

In this Section I propose a comparison between the models and DFT. First, I obtain the ground-state structure predicted by SCALE-UP. Then, I relax this structure using DFT. By doing so one can study the reproduction of the energetics of low energy phases. However, it should be underlined that this is not necessarily leading to the global minimum of the energy in DFT, and rather to a low energy phase.

In Table 4.2 I have summarized the results of the ground state structures predicted by both the mixed models and DFT, and characterized the structure by observing which distortions are occuring in the cell.

Note that the relaxation process using DFT confirms that the phases found using the models are critical points of the PES and have a lower energy than the references considered, which in the case of DFT, is the relaxed cubic-like structure. Also, in many of the cases considered the agreement in terms of both energies and distortions is qualitatively and quasi-quantitatively good. However, there are obvious deviations that I discuss in the following.

**Table 4.1:** Comparative table of the elastic tensors as produced with DFT calculations and by using the approximative scheme proposed for averaging. The predicted values are given in parenthesis. The units of the elastic tensor are given in Hartree.

| Case | $C_{11} = C_{22}$ | $C_{33}$ | $C_{12}$ | $C_{13} = C_{23}$ | $C_{44} = C_{55}$ | $C_{66}$ |
|---|---|---|---|---|---|---|
| $PbTiO_3$ | 38.3 | 38.3 | 14.6 | 14.6 | 11.3 | 11.3 |
| 7Pb1Sr | 38.5 (38.6) | 38.5 (38.6) | 14.2 (14.2) | 14.2 (14.2) | 11.5 (11.5) | 11.5 (11.5) |
| $(PTO)_3/(STO)_1$ | 38.9 (39.0) | 38.9 (39.0) | 13.9 (13.9) | 13.9 (13.7) | 11.5 (11.6) | 11.7 (11.6) |
| Rocksalt | 39.4 (39.7) | 39.4 (39.7) | 13.3 (13.2) | 13.3 (13.2) | 12.0 (12.0) | 12.0 (12.0) |
| $(PTO)_1/(STO)_1$ | 39.6 (39.7) | 39.4 (39.7) | 13.2 (13.2) | 13.2 (13.0) | 11.9 (11.9) | 12.0 (12.0) |
| $(PTO)_2/(STO)_2$ | 39.6 (39.7) | 39.5 (39.7) | 13.1 (13.2) | 13.2 (13.0) | 11.9 (11.9) | 12.0 (12.0) |
| $(PTO)_1/(STO)_3$ | 40.3 (40.4) | 40.2 (40.4) | 12.4 (12.5) | 12.5 (12.4) | 12.2 (12.2) | 12.3 (12.3) |
| 1Pb7Sr | 40.7 (40.8) | 40.7 (40.8) | 12.1 (12.1) | 12.1 (12.1) | 12.4 (12.4) | 12.4 (12.4) |
| $SrTiO_3$ | 41.1 | 41.1 | 11.8 | 11.8 | 12.6 | 12.6 |

| Case | Mixed models | DFT | Order parameters (model) | Order parameters (DFT) |
|---|---|---|---|---|
| $PbTiO_3$ | -50 | -57 | $P_z$ | $P_z$ |
| 7Pb1Sr | -40 | -43 | $P_z$ | $P_z$ |
| $(PTO)_3/(STO)_1$ | -44 | -15 | $P_z$ | $P_z$ |
| Rocksalt | -17 | -12 | $P_z\phi_z^-\phi_y^-$ | $P_z\phi_z^-\phi_y^-$ |
| $(PTO)_1/(STO)_1$ | -22 | -16 | $P_z\phi_z^-\phi_y^-\phi_x^-$ | $P_y\phi_z^-\phi_y^-\phi_x^-$ |
| $(PTO)_2/(STO)_2$ | -38 | -11 | $P_z$ | $P_z$ |
| $(PTO)_1/(STO)_3$ | -13 | 0 | $P_z$ | $P_z \to 0$ |
| $(PTO)_1/(STO)_3$ | -8 | -5 | $P_y$ | $P_y$ |
| 1Pb7Sr | -13 | -10 | $\phi_z^-$ | $\phi_z^-$ |
| $SrTiO_3$ | -13 | -12 | $\phi_z^-$ | $\phi_z^-$ |

**Table 4.2:** Energies of the ground state structures as computed using the mixed models and DFT. The main distortions occurring in the cell are also displayed, with $P_\alpha$ symbolizing the polarization and $\phi_\alpha^-$ being an anti-phase rotation, where $\alpha$ labels the cartesian direction. The reference of the energy is set as zero for the RS in the mixed models, and the relaxed cubic-like structure of each case for the DFT calculations. Energies are given in meV per 5 atoms.

In the cases of $(PTO)_1/(STO)_1$ and $(PTO)_1/(STO)_3$ the relaxed structure using DFT has different distortions than the predicted by the models. In both cases it is clear that the models favor a polarization along the $z$ direction, while DFT shows that $P_y$ is preferred. In particular, the superlattice $(PTO)_1/(STO)_3$ has no stable phase with a polarization along $z$. The same kind of problem is visible in the cases $(PTO)_2/(STO)_2$ and $(PTO)_3/(STO)_1$, where the model predicts energies much lower than those of DFT.

Qualitatively, the models have notable disagreements in the energy prediction of the phases. The energy predicted for the phase with polarization $P_z$ in $(PTO)_3/(STO)_1$ is considerably lower when computed using the model. This occurs also for the $(PTO)_2/(STO)_2$ superlattice. The energies of the ground states predicted for the superlattices $(PTO)_1/(STO)_1$ and $(PTO)_1/(STO)_3$ is also strongly deviated from the energies calculated using DFT. This is consistent with the discussion in Section 4.2.1 where we see that, because of the choice of $\epsilon_\infty$, the models tend to exaggerate the tendency to develop a polar distortion along $z$.

### 4.2.4 Application: $(PTO)_n/(STO)_n$ superlattices and PTO nanowires in an STO matrix

I have chosen to apply first the method to study $(PTO)_n/(STO)_n$ superlattices, for which the results can be compared with available literature for both experimental and theoretical results [20, 21]. The interest of this type of superlattices is the observed chiral structures appearing in the PTO layer, resembling that of vortices of polarization (see Figure 1.8). For this particular example the models have been generated using PBEsol potentials.

The model for the superlattice is built using the approximative approach described in this Chapter. I use Monte Carlo simulations through the Metropolis algorithm to obtain the structure of the ground state predicted by the model, for which I calculate the electrical dipoles of the 5-atom cells

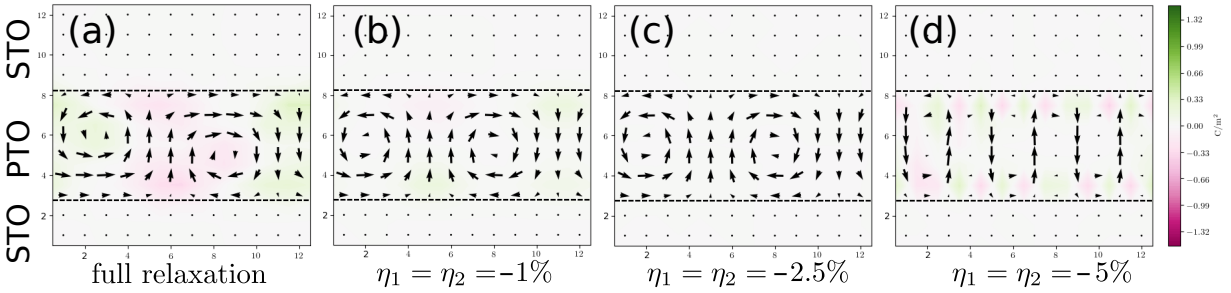


**Figure 4.6:** Study of the ground state of $(PTO)_6/(STO)_6$ superlattices, displaying the electric dipoles appearing in the PTO layer in the $yz$ plane. **(a)** Full relaxation of the superlattice. **(b)** Relaxation under fixed -1% strain in-plane. **(c)** Relaxation under fixed -2.5% strain in-plane. **(d)** Relaxation under fixed -5% strain in-plane.

of the composite at the center cation, in this case, the titanium atoms.

Figure 4.6 shows the result of this for relaxations under a fixed in-plane strain, where I apply also the constraint $\eta_1 = \eta_2$. The strain is applied directly on the RS of the mixed model, being the rest of the strain variables unconstrained. In panel (a) a full relaxation is performed, providing a structure that reminds of the experimental observed structure (see panel (a) of Figure 1.8). Nonetheless, the structure displays a strong polarization in the plane.

In panels (b), (c) and (d) I show the result of the relaxations for different applied in-plane negative strains (compressive character). The calculations provide a much better agreement with both the experimental and the theoretical results, as the applied strain leads to a reduced in-plane polarization. This leads to much better defined vortices of polarization (see panels (b) and (c)). With increasing compressive strain the polarization along the $x$ direction also diminishes, becoming absent for the case of $-2.5\%$ epitaxial strain. For even higher strains, the results suggest that within the PTO layer anti-phase 180º domain walls appear, with domains alternating polarization in the superlattice.

Additionally to the work performed on the (STO)/(PTO) superlattices, I have also looked into the ground state structure of a PTO nanowire in an STO matrix (analogous to the example available in the literature for the prediction of electrical skyrmions in barium titanate nanowires [88]). The structure is built in the following way: I define a chemical order of STO in an 8×8×1 supercell, and I inscribe in the 8×8 plane a $4 \times 4$ square PTO region. Due to the periodic boundary conditions, the system simulated is that of a nanowire within an STO matrix.

In Figure 4.7 I show the polarization of the ground state predicted by the model. As can be seen, the sample displays a polarization vortex-like structure in the plane at the PTO region. This is accompanied by an out-of-plane polarization display. The behavior observed is similar then to the result in Ref. [88].

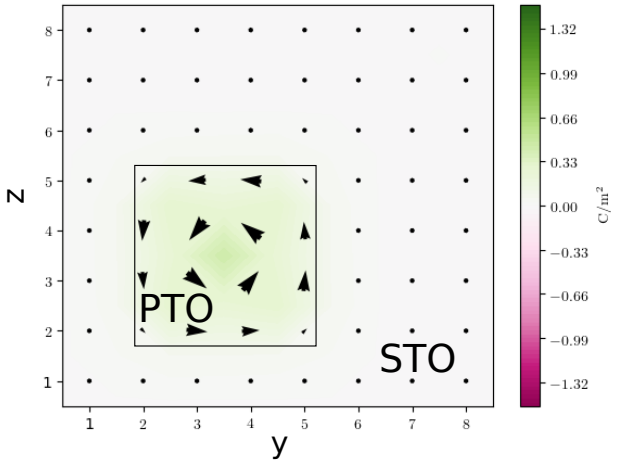


**Figure 4.7:** Polarization map of the ground state of a PTO nanowire within an STO matrix as predicted by the mixed model potentials. The arrows indicate the polarization in-plane, while the color scale indicates the polarization out-of-plane.

## 4.3 Outlook

The mixing models approximation presented in this Chapter has been shown to provide with a tool for obtaining models able to simulate chemically inhomogeneous compounds. The model generation itself occurs in matters of seconds in a computer, making the process an efficient way of studying this family of materials.

The overall behavior of the mixed models created show good agreement with DFT results. The different approximations discussed have been shown to be reasonable. Particularily for the $E_{\mathrm{p}}$ and $E_{\mathrm{s}}$ energy contributions, the results on the different compositions studied show that the method is qualitative and quantitative correct in most cases.

The discrepancies observed in the study of limit cases, such as $(\mathrm{PTO})_1/(\mathrm{STO})_1$, has shown that the approximation of the electrostatics has room for improvement. More precisely, a refinement in the calculation $\epsilon_\infty$ to account for the anisotropy induced by the chemical order is a clear perspective to improve the overall behavior of the models.

Due to the choice of the RS, and particularily for systems like superlattices, it is also reasonable to explore a correction of local strains. The reason is that the choice of RS has in practice no impact on the non-electrostatic short-range interactions, as these type of coupling only depends on the displacement of the atoms and not their absolute position. Hence, effectively in the layers these interactions are behaving as if locally the system was equivalent to the pure system, not accounting for the strain induced by the choice of the averaged new lattice parameters with respect the pure system.

Finally, it is also of future work to develop a model generation method as depicted in panel (b) of Figure 4.1. A strategy which involves studying the different realizations of chemical disorder, accompanied by the fact that non-electrostatic short-range interactions decay fast in distance, would provide better description of the chemically disordered system.

# Chapter 5

# Examples of application

In this Chapter I review some studies on perovskites performed during the Ph. D. using the presented model potentials. First, in Section 5.1 I present a discussion on the character of the 180º antiphase domain walls in $SrTiO_3$. I describe the state-of-the-art to contextualize the problem and explain the approach selected to study this characteristic large-scale phenomena using atomistic simulations. Then, in Section 5.2 I briefly present two collaborative works that have led to recent scientific publications: the study of thermal conductivity accross domain walls in $PbTiO_3$, and the novel finding of electric analog of magnetic skyrmions in homogeneous media.

## 5.1 Ferroelectricity in 180º antiphase domain walls of $SrTiO_3$

### 5.1.1 Motivation

As has been discussed already in this Thesis, the case of $SrTiO_3$ is complex even for bulk studies. The most intrincate aspect of the compound is the underlying competition between the AFD and FE distortions. It is nowadays accepted that the stabilization of the AFD ground-state at very low temperatures is due to the quantum fluctuations [71], but it still displays large anisotropic dielectric constants ($\epsilon_{xx} = \epsilon_{yy} = 40.000$, $\epsilon_{zz} = 10.000$) signaling a ferroelectric instability [74, 89–91].

In study the effect of negative pressure on STO in the following way. As a function of varying negative pressure I perform relaxations of the structure using Monte Carlo simulations (to see examples on the literature, see Ref. [73]; also, I use the EHM fitted to TS@10 in this work). The results are shown in Figure 5.1. First, I calculate the result of an unconstrained relaxation, corresponding to the ground state (black line of panel (a). Also, I perform constrained relaxations to calculate the energy of a phase with FE distortion and a phase with AFD distortion as a function of varying external pressure, as these are the two distortions that are competing (red and blue lines respectively). As can be seen, the ground state distortion shifts from AFD to FE for increasing negative pressure.

Panel (b) displays the order parameters ($P$ and $R$) values of the ground state at 0K. At zero applied external pressure the ground state is that of experimental $SrTiO_3$, with an anti-phase rotation pattern in which the rotation vector of the oxygen octahedra is parallel to the [001] crystallographic axis. Then, the model predicts a transition to a ferroelectric phase with the polarization parallel as well to the [001] axis. The transition occurs between -4.7 and -3.7 GPa, where the two distortions may coexist according to the prediction of the model. Negative external pressure on $SrTiO_3$ has

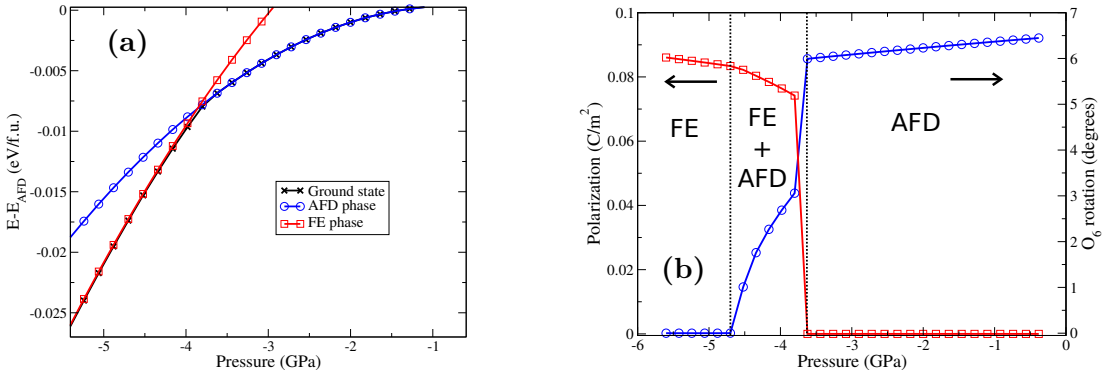


**Figure 5.1:** Study of the ground state of $SrTiO_3$ for varying hydrostatic pressure. **(a)** Energy of the relaxed phases with respect to the RS. The black line corresponds to the ground state. **(b)** Order parameter of the fully relaxed system under constant hydrostatic pressure. Blue line corresponds to the rotation of the oxygen octahedra, while the red line represents the total polarization of the unit cell.

two effects: first, it weakens the AFD distortion; second, it favors the FE distortion, which in presence of a weakened AFD distortion eventually becomes the only ground state distortion.

The scientific community has devoted a notable effort to attempt to exploit this competition and to find the fingerprints of a ferroelectric character in $SrTiO_3$. One of the aspects in which research has focused on are the so-called domain walls (DWs). A domain wall is the interface that occur between domains within the material. The domains are equivalent phases with different orientation. This idea can be illustrated with an example. Let us assume that a domain order parameter is the rotation $R_\alpha$, where $\alpha$ labels the cartesian direction. Now let us consider a second domain, adjacent to the first, with an order parameter $-R_\alpha$. The domain wall would then be the interface between the two domains, and it describes how $R_\alpha$ becomes $-R_\alpha$. For a depiction of this, see the $R_z$ curve in Figure 5.2.

In the specific case of the DWs I am investigating the rotations occur along one axis, $R||[001]$. Also, the DWs are oriented by having the normal vector of the domain wall orthogonal to the rotation axis. Since the rotation of Domain I is the opposite to that of Domain II the order parameter must vanish at the DW. It is precisely in this antiphase DW that the competition between FE and AFD distortions in $SrTiO_3$ gains relevance: if structurally the AFD distortion vanishes, would that mean that a FE distortion may occur as in the example with the hydrostatic pressure?

This type of domain walls have been object of study in the past [92], as well for the particular case of $SrTiO_3$ [93]. The work in Ref. [92] uses a Ginzburg-Landau potential to study the behavior of the order parameter. For $SrTiO_3$ let us consider the order parameters $R_z$ and $P_z$, referring to the rotation of the oxygen octahedra and the ferroelectric polar distortion respectively, both parallel to the [001] crystallographic axis. The Gibbs free energy is then written as

$$G = \frac{1}{2}\gamma_1(\nabla R_z)^2 + \frac{1}{2}\gamma_2(\nabla P_z)^2 + \frac{1}{2}A_1R_z^2 + \frac{1}{4}B_1R_z^4 + \frac{1}{2}A_2P_z^2 + \frac{1}{4}B_2P_z^4 + \lambda R^2P_z^2, \qquad (5.1.1)$$

where $\gamma$, $\gamma_i$, $A_i$ and $B_i$ are parameters (for $i = 1, 2$). This is the form of the fourth-order Landau potential for the two order parameters, but adding both a coupling between $R_z$ and $P_z$ and gradient-based terms required to model accurately the behavior of the order parameters in the

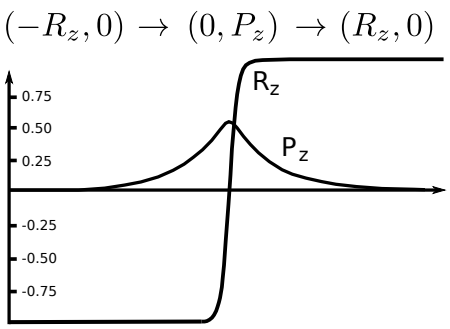


**Figure 5.2:** Evolution of the (normalized) order parameters across a domain wall at which the primary order parameter, $R_z$, vanishes. As $R_z$ goes to zero, the secondary order parameter $P_z$ arises and achieves its maximum at the center of the domain wall. The Figure has been extracted from Ref. [92].

domain wall.

The authors apply this model to study several types of domain walls and order parameters. In particular, the work presents a study of the transition $(-R_z, 0) \rightarrow (0, P_z) \rightarrow (R_z, 0)$ (see Figure 5.2), showing evidence that if there is a competition between the order parameters (for which $\lambda > 0$ in 5.1.1) then in the absence of the primary order parameter the secondary order parameter may arise in the domain wall.

In the specific case of this type of DWs occuring in $SrTiO_3$, Ref. [93] presents a study predicting the ferroelectric instability to occur. The result is obtained by using a more complex expression for the Gibbs free energy, which accounts for rotations occurring in all cartesian directions and takes into account the elastic part of the energy. Additionally, the model is completed by assuming the FE instability to be present and thus writing the corresponding $P_\alpha$-related terms. The description of the gradients of rotations is much more complete than in the previous work.

The calculations of Ref. [93] show two remarkable results. First, for DWs in which the rotation axis is perpendicular to that of the normal vector of the DW they predict that it is favorable for a secondary rotation to appear, with the rotation axis parallel to that of the normal vector of the DW. Second, their model shows that in these conditions there is an elongation of the cells within the DW parallel to that of the rotation vector in the domains, enhancing the ferroelectric instability of the material which then arises within the domain wall.

In the works discussed the authors use a continuum, heavily coarse-grained theory to study the DWs of $SrTiO_3$. Instead, SCALE-UP allows for atomistic simulations of this DW. One can then study the atomic structure of the material and observe how the predictions fit in the simulated system.

### 5.1.2 Atomistic simulations

The study I present in this Manuscript of the DW in $SrTiO_3$ is carried out using the EHM fitted to TS@10 presented in Chapter 3. The simulation box contains 1600 atoms. In particular I use an 80x2x2 repetition of the unit cell, and thus the elongated axis for this study is the $x$ cartesian direction. This corresponds to a length of 30.9 nm. The rotation axis is chosen to be along the $z$ direction.

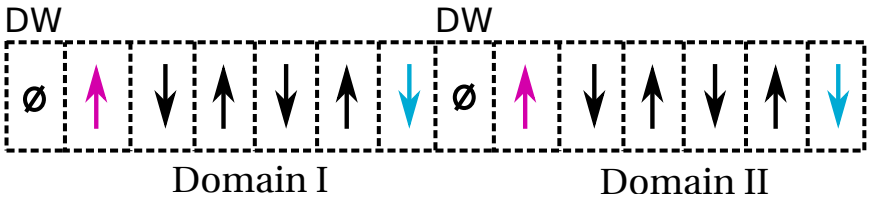


**Figure 5.3:** Sketch of the initial preparation of the DW simulated samples. The arrows represent the rotation axes, with each arrow representing the anti-phase rotation character of $2x2$ repetition of the perovskite unit cell in the $yz$ plane. Because of the perovskite structure adjacent arrows are necessarily opposed. The blue arrows are the last rotation vector of the domain and pink arrows are the first, showing the break of translational symmetry. The $\emptyset$ symbols represent the cells left undistorted for the domain wall to arise from an atomic relaxation simulation.

The DW simulated samples are prepared as follows (see the sketch in Figure 5.3). I divide the elongated axis in two. Domain I ($0 < x < 40$) is prepared with the AFD distortion pattern of the ground state of $SrTiO_3$. Domain II ($40 < x < 80$) is prepared exactly in the same way, but with the opposite rotations as those of domain I. Cells with $x = 40$ and $x = 0$ are then left undistorted; also, because of periodic boundary conditions, $x = 0$ and $x = 80$ are the same cell. The domain wall arises from relaxing the structure, as the domains have opposed orientations of the rotation order parameter.

The loswet-energy structure of the multidomain configuration is obtained through Monte Carlo simulations of the neutral sample described, for which I use an annealing parameter to relax the structure to 0 K. I apply 10.000 MC sweeps for the simulated annealing, starting typically at T=0.01 K. Similarily, to study the effect of applied external electric fields I apply an homogeneous field $E_z$ and relax the sample following the same procedure.

### Structure of the DW

In Figure 5.4 I describe graphically the structure of the domain wall. In the depicted plane, it is observable how the rotations along the $z$ axis vanish through the domain wall, and appear again afterwards. Within the domain wall a rotation along the $x$ axis appears. This rotation can be observed at the displacement of the oxygens along the $y$ direction in antiphase, which appear much clearer at the center of the domain wall.

The order parameters extracted from the whole sample are shown in Figure 5.5. I have calculated the rotations in the following way: I define the first cell as having a positive $R_\alpha$ rotation if it occurs anticlockwise (following the usual notion of positively-defined bases). Since the rotation is in antiphase, the rotation of the cell $l_x$, where $l_x$ is the integer labelling the cells in the $x$ direction, is given by

$$R_\alpha(l_x) = R_\alpha e^{i\pi l_x}. \tag{5.1.2}$$

This provides a uniform sign for the rotation within the domains. As can be seen in panel (a) of the Figure, the calculated $R_z$ rotations change sign throughout the domain wall. The rotation in the $x$ direction appears only within the domain wall, having its maximum at the center. The value of the rotation $R_x$ at this point is of 5.55 º, about 15% smaller than $R_z$ in the domains, of 6.5 º. As a first result, this shows that the rotation changes in a quasi-continuous way instead of a sharp change of sign. This supports the predictions in [92, 93] of this DW being of Néel type, with

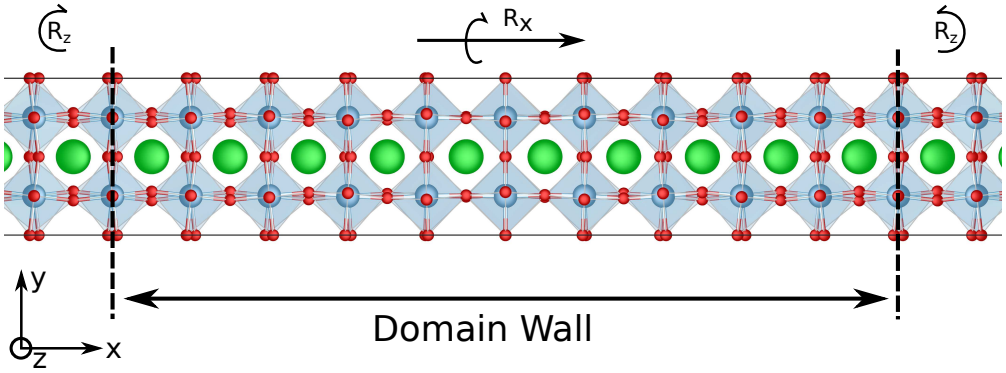


**Figure 5.4:** Graphical representation using `VESTA` of the relaxed DW structure. Here, green atoms represent Sr, blue atoms represent Ti and red atoms represent oxygen sites. I show the $xy$ plane, for which the two y planes appear superimposed.

a thickness of about 39 Åaccording to the simulations performed in this work.

In panel (b) I have calculated the polarization along $z$ of the cells in $x$, by computing the total electric dipole of the cell centered in the titanium atoms. The calculated polarization displays two maxima, being zero at the center of the DW, attaining a value of 0.044 $C/m^2$.

### Atomic relaxations under applied external electric field

The appearence of a polarization in the results shown in Figure 5.5 suggest the interest of studying the DW under applied external electric field. To do so, I have annealed the same structure presented in Figure 5.3 in the presence of external electric fields, $E_z$ and $-E_z$. The results are shown in Figure 5.6.

In panel (a) the field applied is positive, of $10^{-4}$ V/m. This leads to a polarization $P_z$ of positive character, aligned with the electric field. The rotation in $x$ is negative in this case. Oppositely, in panel (b) I reverse the electric field and the polarization becomes $-P_z$. Notably, the rotation within the DW along the $x$ axis also has the opposite sign. Thus the model predicts that, under a reversed electric field, the character of the DW rotations is also reversed.

The result is in this case two-fold. First, the model predicts that the domain wall is ferroelectric, as the polarization can be switched using an external electric field. Second, the change in the sign of the rotations suggests that there is a coupling between $P_z$ and $R_x$.

### Interpretation of the results

Recently A. Schiaffino and M. Stengel have proposed a Ginzburg-Landau model to study the character of 90º domain walls in $SrTiO_3$ [94]. In their study, they find that this DWs display as well a polar distortion and that they key aspect for it to develop is to consider couplings of the form

$$P_z R_z \frac{\partial R_x}{\partial x} \quad ; \quad P_z R_z \frac{\partial R_x}{\partial x}. \tag{5.1.3}$$

The first coupling describes the interplay between the rotation $R_z$ and the derivative of the rotation $R_x$. In panel (a) of Figure 5.7 I have represented the value of this coupling across the sample.

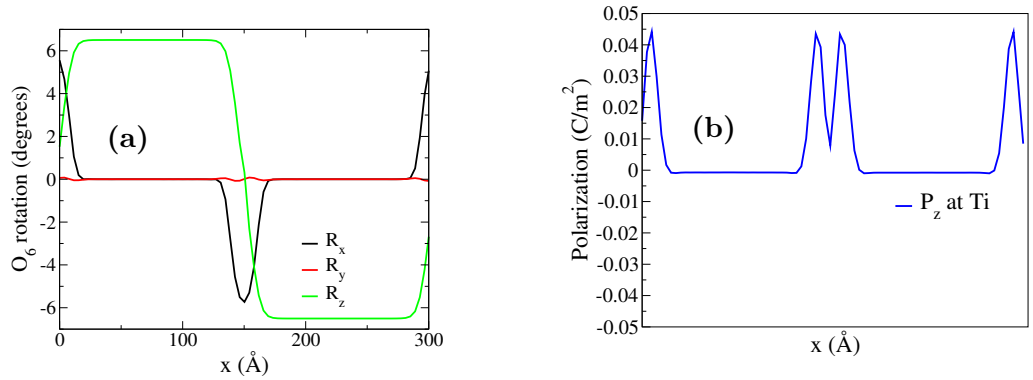


**Figure 5.5:** Calculated order parameters ($R$ and $P$) along the $x$ direction of the sample. **(a)** Rotation along the three cartesian directions. **(b)** Polarization along the $z$ axis.

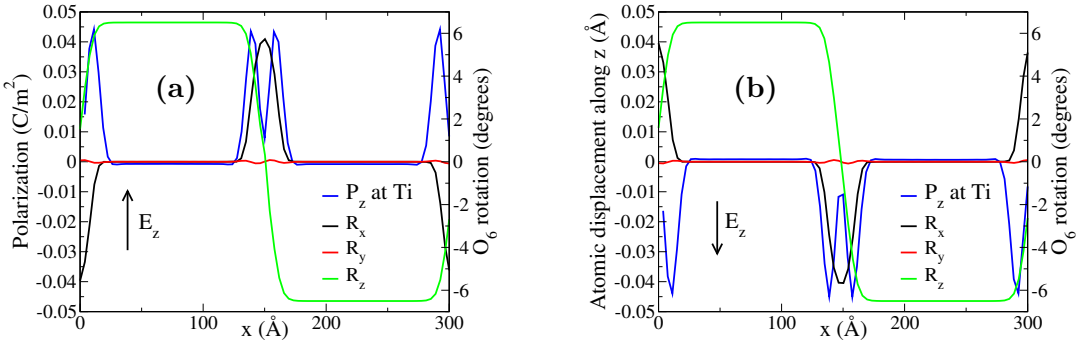


**Figure 5.6:** Study of the order parameters of the sample containing two DWs under an applied external electric field. **(a)** The applied electric field is positive along the $z$ direction, to which the polarization aligns. **(b)** In this case the electric field is reversed, leading to a polarization $-P_z$ within the DW.

Due to the simultaneous change of sign of $R_z$ and the derivative of $R_x$ the sign of the coupling is positive always, displaying two peaks. These two peaks coincide with the peaks of polarization in Figure 5.6, both in position and sign. This suggests that the polarization arises from the coupling term - and thus it is an *improper* order parameter.

The term also explains how switching $P_z$ has as a result the switching of $R_x$. Since the sign of the polarization changes, preserving the sign of $R_x$ would have an impact in the energetics of the system. In order for the two states to be equivalent in energy, since the gradient and the sign of $R_z$ is the same in both cases the gradient of the rotation $R_x$ has to change.

In panel (b) of Figure 5.7 I show the value of the second coupling term, which acquires an absolute maximum value at the center of the domain wall. The polarization is proportional to this coupling term as well, which describes the polarization at the center of the DW. Note that $P$ is not zero at the center of the DW, the bias being explained through this second coupling term.

The atomistic simulations I perform result in agreement with the previous theoretical studies of the antiphase DWs in $SrTiO_3$. The ferroelectric distortion is appearing at the domain wall, accompanied by the vanishing of the rotation order parameter of the domains as suggested in

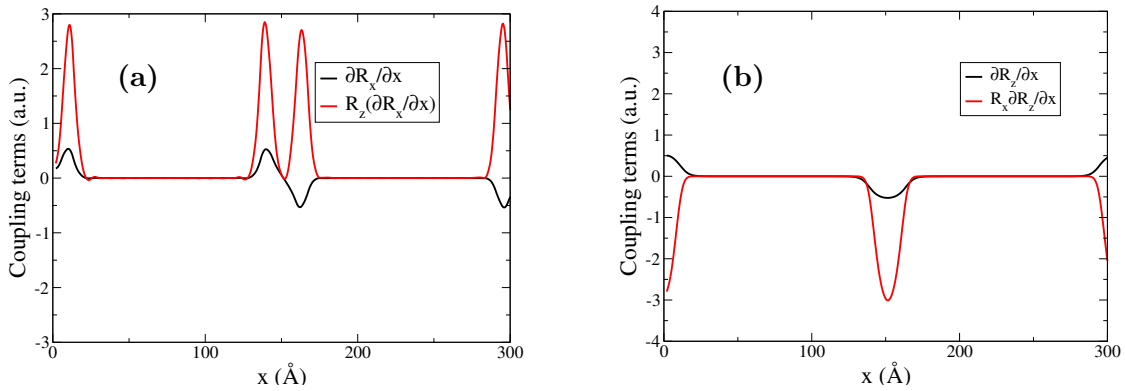


**Figure 5.7:** Calculation of the value of the gradients and the coupling terms.In order to reduce the noise due to discretization in the calculation of the derivative I have interpolated the curves for the rotations $R_x$ and $R_z$ from panel (a) in Figure 5.6, and I have used the interpolation to numerically differentiate the curves. **(a)** Value of $R_z \dfrac{\partial R_x}{\partial x}$ and $\dfrac{\partial R_x}{\partial x}$ across the sample. **(b)** Value of $R_x \dfrac{\partial R_z}{\partial z}$ and $\dfrac{\partial R_z}{\partial x}$ across the sample.

Ref. [92]. I want to remark that the model used in this study has in fact no FE instability, although it is a quite soft mode (see Figure 3.5).

The simulations show as well that a rotation appears within the domain wall as a proper. The thickness of the wall and the appearence of $R_x$ are in good agreement with the research presented in Ref. [93]. Also, the rotations and the polarization within the DW are well described by the formulation presented in Ref. [94].

### Future perspectives

In this research I have studied structurally the DW in $SrTiO_3$, although further investigations could provide more insight and understanding of its nature. In particular, an adaptation of the work presented in Ref. [94] in the form of a Ginzburg-Landau model adapted to the anti-phase DWs would be an adequate perspective to support the presented results, as the explicit description of the couplings involved is a direct way of understanding the energetics of the DW.

It is also enticing to observe this problem from a more complete theory perspective. For this, a collaboration with N. Bristowe (University of Kent, U.K.) is also engaged, in which he is studying these DWs using DFT simulations. This potentially provides support and validation to the research, confirming the fingerprints of the phenomena observed using the second-principles models.

I focused on studying the character of the order parameters in this work. However, there are interesting angles yet to be explored. The polarization observed in the DWs is accompanied by a displacement of the Ti and Sr cations, suggesting that the study local strains may provide further insight to the problem.

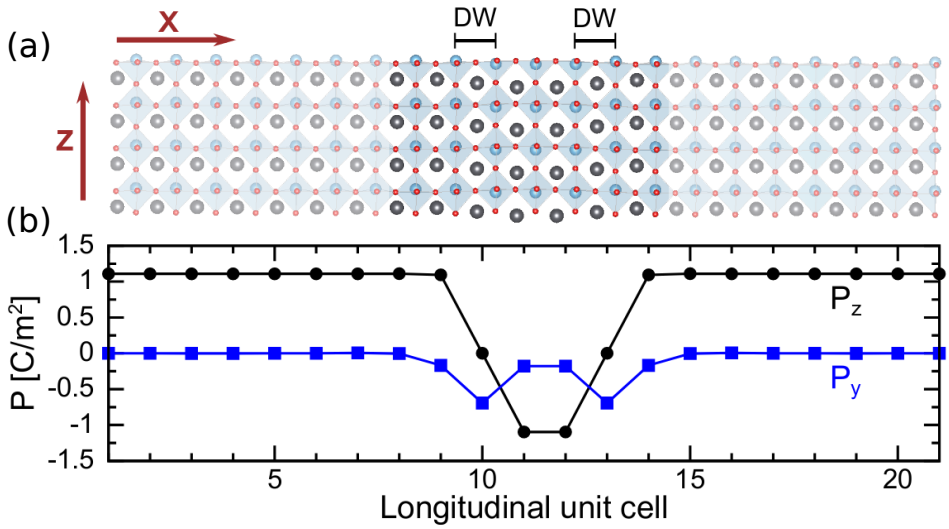


**Figure 5.8:** **(a)** Graphical representation of the 180º domain walls in $PbTiO_3$. The displayed plane is the $xz$, and the domains are polarized along the z direction. **(b)** Profile of the polarization across the sample. The DWs are characterized by displaying zero polarization along $z$ and non-zero polarization along $y$.

## 5.2 Examples of collaborative works

### 5.2.1 Control of thermal conductivity in $PbTiO_3$ using domain walls

We have collaborated with M. Royo, J. Íñiguez and R. Rurali [30] to develop a study on how thermal conductivity is affected by the existence of DWs in $PbTiO_3$.

Domain walls in Lead Titanate can be of different types. We focus here on the 180º DWs as described in panel (a) of Figure 5.8. The global order parameter describing the ground-state phase of $PbTiO_3$ is the polarization. The domains in this material are polar and are arranged in an antiparallel way. From the difference in orientation of the polarization arises the symmetry break that leads to the creation of the domain wall. One of the peculiarities of the domain walls in $PbTiO_3$ is the occurrence of a rotation of the polarization in the domain wall, with a component appearing orthogonal to that of the domains (for an example of this result, see Wojdeł and Íñiguez [28]). The domain wall itself is very thin, and the rotation of the polarization occur in the span of one unit cell.

In the work of studying the thermal transport M. Royo and R. Rurali used a method based on non-equillibrium Green functions to calculate the harmonic propagation of phonons throughout the material, which is the mechanism behind thermal transport in crystals. My role in the collaboration consisted on desigining the samples, with different sizes and different number of DWs, and providing the force-constant matrices associated to the systems. Then, M. Royo computed the probability of transmission of the phonons accross the sample.

The results show that the probability of the phonons to propagate through the DW depends on the character of the vibrations. Phonons that have transversal character propagate less than longitudinal ones. The explanation for this is that phonons that are sensitive to the symmetry break occuring within the DW are more prone to be affected, effectively blocking the vibrations. On the other hand, phonons that are compliant with the symmetry subset compatible with the domains *and* the domain wall, such as in this case the longitudinal phonons, can transmit without

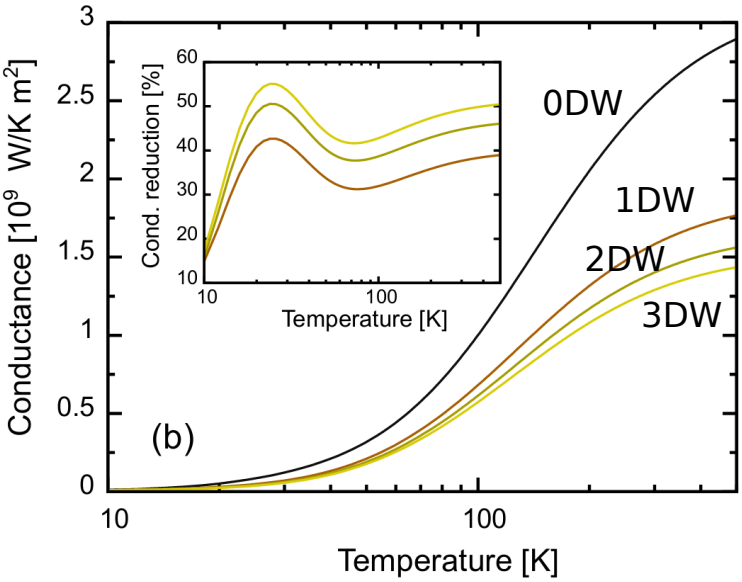


**Figure 5.9:** Conductance as a function of temperature for different number of domain walls in the sample. In the subplot, percentual conductance reduction as a function of temperature.

"seeing" the domain wall. This explains as well why the effect of increasing the amount of DWs is minimal. The results suggest that the domain wall may reduce approximately 40% the thermal conductivity at room temperature by including a single DW (see Figure 5.9).

### 5.2.2 Electric analog of magnetic skyrmions

In collaboration with M.A.P. Gonçalves, P. García-Fernández, J. Junquera and J. Íñiguez we have presented a study of electrical analog of magnetic skyrmions in an homogeneous material [31].

This study arises from the recent effort by researchers to find an analog of magnetic skyrmions using dipolar electric moments. In the study we use nanostructured domain walls of $PbTiO_3$ composed in a closed circuit to create the skyrmion.

The way we proceed is as follows. Two domains are defined with antiparallel polarization, inside and outside the closed-circuit DW, as depicted in Figure 5.10. Because of the in-plane polarization arising at 180º DWs in $PbTiO_3$ this leads to a chiral dipolar arrangement (see panel (a) of Figure 5.10). In the study we prove that the topological charge of this structure is 1, which indicates that it is a skyrmion. The total size of the sample simulated is of $2.3^2$ nm$^2$.

We analyze the stability of the structure from different perspectives. First, by applying external electric fields we observe a transition from the nanodomain-skyrmion (ND-ESK) to a nano domain wall which is polar (NDW-polar, panel (b) in Figure 5.10). This can be observed in the transition of Figure 5.10. Interestingly, we observe that the center of the skyrmion is displaced by the applied electric field in a perpendicular fashion. After the transition, the domain wall displays a metastable state with a net polarization aligned with the electric field.

Then we study the effects of strain on the sample. As a function of strain the ND-ESK evolves from high symmetry to a low symmetry configuration. Then, for $a_{sub} > 3.98$ Åthe ground sate

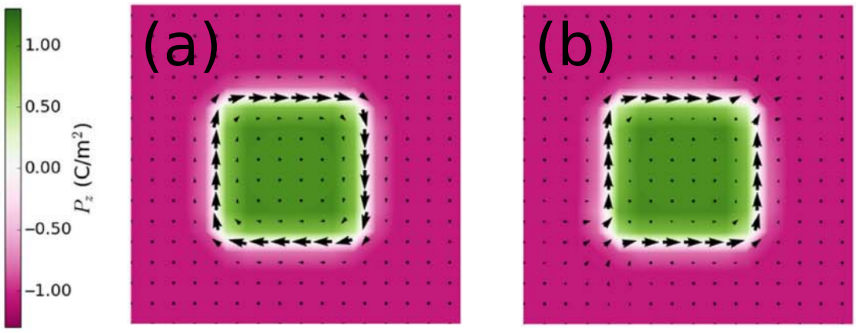


**Figure 5.10:** Polarization of a closed-circuit domain wall in PTO. The domains are constructed as follows: in the plots, pink corresponds to out-of-plane negative polarization, while green is out-of-plane positive polarization. The DW thus arises between the domains, with a polarization in-plane. **(a)** ND-ESK state. The polarization outside and inside the DW are antiparallel along $z$. **(b)** Stabilization of the NDW-polar state by means of applied external electric field of sufficient magnitude.

becomes the NDW-polar state. Hence, the stabilization of the polar state can be achieved both by applying external electric field or by applying epitaxial strain.

# Chapter 6

# Conclusions

The first result presented in this Thesis is a novel method to construct second-principles model potentials, which I apply to construct a model for strontium titanate

On one hand, the fitting of the models is extremely efficient. The reason is that the fitting procedure is analytical, which is both faster than any numerical method and exact. Due to this, the fitting itself is a very fast process that allows to design a method to construct models which is both systematically improvable and automatic. It is worth mentioning that the implementation of this method allows the user to build a model in a regular desktop computer in some hours. The most heavy computational work lies in the DFT calculations necessary to produce the training sets, which typically takes two to three days to produce in a cluster.

On the other hand, the models produced are of high accuracy when compared with the DFT data used to generate them. The accuracy is shown in different aspects. First, I have shown that the models generated for STO have an essentially perfect description of the phonon modes of the Reference Structure. This proves that the fitting procedure is solid. Second, I have also shown that the energetics of the training set data are correctly reproduced. Finally, the structural features of the modeled material are also well described, as the models discussed show an overall qualitatively and quantitatively good description of the structure of the ground state.

I have also proved the applicability of the methodology. Using the generated models of STO I have studied two different problems. First, I have studied the transition temperature of STO, for which the result is qualitatively good although, as discussed in the text, the $T_c$ found is notably higher than the experimental result. This bias originates partially from the simulation technique, in which I do not take into account quantum fluctuations, and party in the limitations that DFT can have at reproducing experimental results, which limits the accuracy that the models can have. Second, I have investigated the properties of the STO 180º anti-phase domain walls. The results obtained show a ferroelectric domain wall occurring. I have contrasted the findings with previous scientific results, showing that our models predict both a gradient of rotations from which the polarization can be explained and an additional rotation occurring in the center of the domain wall, parallel to the DW plane vector, both in agreement with previous literature.

As an important remark, the process of model generation is still not fully automatic. It is still a complicated task to obtain a model which is bounded from below, as there are no mathematical guidelines to ensure this property of the models. The complexity lies in the multivariate character

of the Taylor expansion, which makes the models prone to be unbounded from below. Nonetheless, the manual scheme proposed in this Manuscript provides a good strategy to overcome this difficulty.

The second result that I presented in this Thesis is the adaptation of the SCALE-UP model potentials formulation to describe chemically inhomogeneous systems. Here, I take advantage of compositional variables and redefine the coefficients of the models to include a dependency on the chemical environment. Then, I describe an heuristic procedure to obtain a model for a chemically inhomogeneous system from previously built models of the constituents of the system.

The heuristics procedure consists on a set of approximations: an averaged calculation of short-range interactions based on the local chemical environment; an averaged calculation of the elastic properties of the material by applying approximations typically used in engineering; and an averaged calculation of the dielectric properties and effective charges.

I applied the method to study chemical mixtures of STO and PTO, with which I could measure the impact of the approximations performed. In the Manuscript I have shown that the approximation of short-range interactions is sound. The reproduction of the phonon modes of the different compounds studied is overall qualitatively good, and in most cases, also quantitatively good. Because of the relative similarity of the studied compounds the treatment of the elastic properties is also a success, with minimal errors when compared to DFT calculations; however, I believe that it would be sound to study this approximation for more challenging mixtures. The calculation of the dielectric properties of the material is shown to be the most impactful approximation. As a consequence some of the deviations observed in the calculation of the phonons arise from an inaccurate description of the dipole-dipole long-range interaction, as the approximation does not take into account the anisotropy arising from the chemical order in the calculation of the dielectric tensor. Also, possible inhomogeneities in the electronic screening are not considered in the present scheme.

Nonetheless, one of the key aspects of the heuristics presented is that they preserve locally the description of the original models when the material is chemically clustered or consists of big homogeneous regions, like in the case of superlattices. Because of this I was able to reproduce correctly the vortex-like polarization structures observed in previous works for the $(\mathrm{PTO})_n/(\mathrm{STO})_n$ superlattices. Also, I show that nanowires of PTO in STO matrices are predicted by the model to have a similar behavior than that of previously studied BTO nanowires in STO matrices.

The design of materials was projected originally to be explored within the chemically inhomogeneous system modelization. The idea was to apply the method of Inverse Monte Carlo simulations to optimize the material's properties as a function of the composition and atomic arrangement, if time allowed to do so, following previous demonstrations in the literature [32, 33]. However, the development of the methodologies presented in this Thesis turned into a very time demanding research and we decided to leave this for a future work. Additionally, I decided to spend some time working in collaborative projects where my methods for pure systems could be applied. As a result of this, I have collaborated in the study of thermal transport accross the $180^{\mathrm{o}}$ ferroelectric domain wall of PTO and the characterization of the first observed electric skyrmion in an homogeneous material.

## 6.1 Future perspectives

I would like to discuss here potential developments and future work regarding the methodologies presented.

First, there are two aspects of the model fitting procedure that I believe is worth investigating. One is regarding the expansion order used. In this work I have fitted models up to fourth-order in the displacements. I have observed, however, that the more distorted is the GS with respect the RS, the less accurate is the energy description. In order to overcome this, I think it is worth exploring higher order models; because of the exponential growth of number of terms as the order of the polynomial increases, a strategy would need to be developed in order to obtain efficiently high-order model potentials. Also, the only reason the process is not fully automatic is that the boundedness-from-below cannot be ensured currently. I believe that further development in this direction would lead to a more solid method, facilitating the model construction process. A method like this would allow to construct a database of high-performance models for large-scale materials simulations.

Second, the heuristic scheme presented for the construction of chemically inhomogeneous systems is sound but improvable. On one hand, I think that it would be worth exploring the idea of creating models by defining libraries of interactions as a function of the chemical environment. This would provide a better description of the short-range interactions. On the other hand, there is room for improvement in the approximation of the long-range interactions. A key limiting factor here is that the available theory used typically in DFT and within the formulation of SCALE-UP model potentials assumes that the dielectric tensor $\epsilon_\infty$ is homogeneous throughout the material. A local description of the electronic screening in a way that allows to describe long-range interactions would be a better way of approaching the problem. This is however a challenging task. Also, I found that the regular averaging of the dielectric tensor I apply in the approximation lacks the anisotropy inherent to the chemically inhomogeneous systems. Hence, studying a similar approach than that of the elastic properties of the material could be potentially helpful.

Finally, I believe that the Reference Structure of the model for the chemically inhomogeneous systems could be also improved. The reason is that in the formulation development I am not taking into account explicitely the impact of one material applying locally a strain difference to the other. In other words: the RS is averaged from the original pure systems, but the models used are not strain-corrected and are included as if their respective RS conditions were that of the original model (with the exception of the long-range interactions, for which the size of the cell accounts in the calculation). I believe that a sound correction for the method would be to add a description of local strain deformations with respect the ideal RS. I think that this correction may have a strong impact, particularily for materials in which the phonon soft modes are substantially impacted by strain conditions, as in the case of STO.

# Appendices

# Appendix A

# Implementation and procedural scheme

The mathematical treatment of the method described in Section 3.1 was implemented in the form of a package with name `ModelMaker_Lattice` for `SCALE-UP`. The implementation of `SCALE-UP` model potentials is written in `FORTRAN 90`. The package includes an extension to `Python 2` that allows to interactively initialize the models and perform calculations and manipulations. We took advantage of this feature and developed an interface, also written in `Python 2`, that allows for the treatment of the models and the manipulation of the parameters to perform the fitting of the model potentials with the proposed scheme. We also developed a variety of tools written in the same language that allow us to extract the training set data in an automatic way from the `VASP` calculations, the different structural parameters of the RS, dielectric properties and elastic properties. Finally, we took advantadge of the flexibility of the platform to write scripts that ease the process of analyzing the eigenvectors and eigenvalues of the Hessian matrix of the system, prepare the standard set of calculations needed from DFT to begin the fitting process, and so on.

## A.1 Implementation details

The base code of the `ModelMaker_Lattice` consists in two main libraries that interact during the process of fitting a model. First, we developed a library that handles the process of fitting a given model. In the notation of Section 3.1, given a $\mathcal{T}_p$ set of couplings with $\Theta_p$ associated parameter space, a TS collection of data and the structural, dielectric and elastic properties of the RS, this library allows the user to create a simple script to fit any desired subset $\mathcal{T}_{p'} \subseteq \mathcal{T}_p$ with parameters $\Theta_{p'} \subseteq \Theta_p$.

In order to do so, the code constructs all the elements of the linear system of equations represented in 3.1.15. Then, we solve the system using the `NumPy` package, which provides us with an analytical solver for linear systems of equations. After the fitting is performed, the code automatically evaluates several key quantities such as the Goal Function value, the energy of the configurations within the training set, the average energy deviations and outputs as well a comprehensive description of the couplings fitted. Of course, the output also contains the set of fitted parameters, so that the user can readily use them to perform any sort of analysis on the fitted model.

The second library included in the package is the responsible for the handling of the stepwise forward selection method described in Section 3.1.2. Technically, this library uses the fitting library

described above to fit in an automatic way all the models that are necessary to follow with the stepwise forward selection method. We coded also a simple way of analyzing the Hessian matrix during the model construction process, so that figures like Figure 3.5 can be readily produced to observe the performance of the model towards known data (which we consider a useful tool when building the harmonic part of the models). It also outputs information on the evolution of the Goal Function throughout the process, a detailed comprehensive list of the terms that are being added at each step of the procedure and performs an analysis of the energetics behavior. It is important to note that this library takes advantage on the fact that, given a particular set $\mathcal{T}_p$ and a TS, one can construct the elements of the matrix in 3.1.15 and fitting different flavors of models is then but a simple re-selection of the rows and columns of the matrix, so that the calculation of the matrix is dramatically eased. Also, the implementation automatically handles the different contributions of the system of equations, which means that automatically detects and asigns the contributions of $E^{\text{fixed}}$ and retains in the LHS the actual representation of the terms that have to be fit.

Finally, we also wrote a script that uses the model generation library to inspect a proposed set of terms, $\mathcal{Q}_q$, that the user may want to use to attempt to bound the models using the scheme presented in Section 3.1.4.

## A.2 Flowcharts

In the following we present the flowcharts of the fitting and model construction libraries.

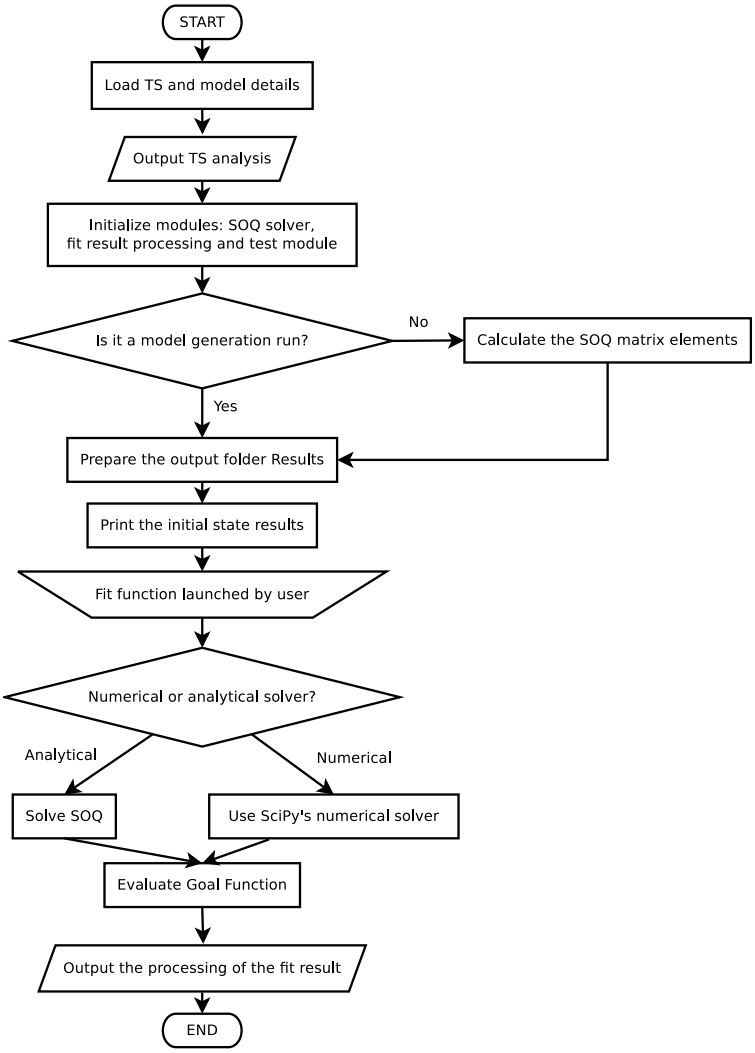


**Figure A.1:** Flowchart of the library responsible for the fitting of a given set of $p$ terms $\mathcal{T}_p$.

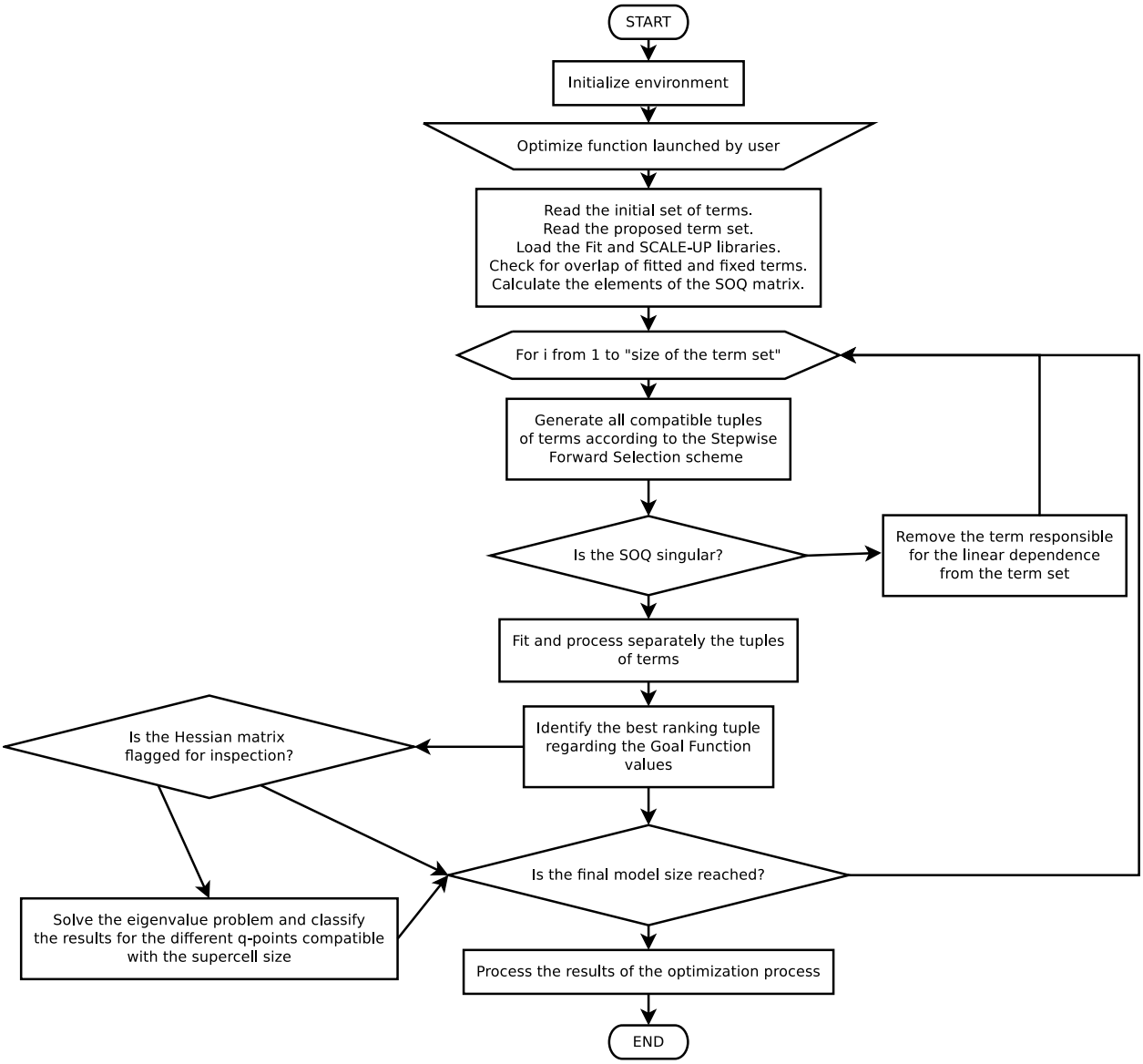


**Figure A.2:** Flowchart of the library responsible for the model generation process of a given set of $p$ terms $\mathcal{T}_p$.

## A.3 Schematics of the method

We conclude this Chapter by giving a short summary of the method of the overall model construction process, as we believe that such practical information will help the reader to understand the overall process and, potentially, any future user of the package could benefit from it.

The overall model construction process can be regarded as a tree schematics.

1) **Gathering the training set data**. In the example, using Density Functional Theory to produce it. It is recommended to have some knowledge on the material, such as the decay length of short-range interactions, the metallic/insulator character, etc. The knowledge of the ground state unit cell may provide critical information about the cell size requirements, also.

   a) Calculation of the Reference Structure parameters, which we recommend to be a high-

symmetry phase.

b) Calculation of the harmonic TS, for example, by computing the Hessian matrix of the Reference Structure.

c) Calculation of the Dielectric tensor and Born effective charges (if the material is an insulator) and the elastic properties of the Reference Structure.

d) Performing Molecular Dynamics simulations at target temperatures that allows for the inspection of the PES at the region of interest.

2) **Prepare the model construction process**.

a) Extraction of the data generated in Step 1). It is sensible also to devote some time into generating the various training sets that can be of use. We recommend to have, at least, two training sets available: the TS responsible for the harmonic fit (described in 3.2.4), and the TS@, that can be built from a Molecular Dynamics trajectory, for example. Also, for materials similar to the application explained in this Chapter we recommend training sets containing between 50 and 100 different configurations. The amount of configurations has an impact in the efficiency of the code.

b) Definition and generation of the target term set $\mathcal{T}_p$, that contains ideally all interactions used for in the stepwise forward selection procedure. The symmetry of the Reference Structure is of crucial knowledge to generate all the available SATs. For this, we recommend:

- Identify the harmonic couplings that can occur in the supercell that is being used for the model generation. In the application for $SrTiO_3$ this corresponded to a $2 \times 2 \times 2$ 40-atom supercell, for example.
- Selecting the level of anharmonicity that the material may require. This can be corrected later in the process.
- Defining the minimal term set, $\mathcal{Q}_q$, that is going to be used to apply boundedness-from-below. In order to do so, we recommend to consider terms describing simple two-body interactions and strain-phonon couplings enabling the user to cap all possible directions in the configurational space. However, using as few interactions as possible is important, as the automatic inspection tool developed for this purpose searches for *all* combinations of the proposed terms, and this number scales incredibly fast with $|\mathcal{Q}_q|$.

3) **Generate the model**. We propose the following basic scheme, that can be adapted if necessary.

   a) Fit through stepwise forward selection the harmonic part of the model. Then, *observe* the convergence of the different modes occuring within the supercell by comparing the Hessian matrix analysis of the model potential and the source of data obtained in Step 1). This is usually providing useful information, both about the system and about problems or bad approaches that the user may be putting in place.

   b) Fit through stepwise forward selection the anharmonic part of the model. Note that the 50 models that result of this process will most likely be still *unbounded-from-below*. For materials similar to the application presented in this Chapter, we recommend that the user produces models with as many as 50 terms.

   c) Define and apply a stopping criterium such as the one described in Section 3.2.4. For example, the user can attempt to apply a confinement potential to study the properties of the ground state that the model is predicting.

   d) Apply the ensuring boundedness approach. This is the less automatic, and potentially most difficult part of the process. We implemented a tool that eases the process through inspecting the proposed $\mathcal{Q}_q$, but sometimes this process requires:

      - Manually applying a self-consistent cycle to obtain positive parameters for the terms in $\mathcal{Q}_q$ (see Section 3.1.4).
      - Adding new data to the Training Set, i.e., revisiting Step 1.d) or calculating 1.b) for particular problematic or polymorph structures. As an example: for the generation of a good $SrTiO_3$ model we required to have information of an unrelated structure. Another example can be the case of Lead Titanate. This material exhibits in the ground state a phase that is polarized along one of the main axis ($P||[100]$), but in order to properly construct a model we found that it is relevant to add information of phases with $P||[110]$ and $P||[111]$.
      - Run Monte Carlo annealed simulations to find runaway solutions in unbounded models. Sometimes through inspection of the different contributions to the energy in such structures one can realize how apply an adequate bound.
      - Consider re-visiting Step 2.b). We find that, in some cases, it is useful to redefine the order of anharmonicity that the model has.
      - Reconsider that, maybe, $\mathcal{Q}_q$ is not complete enough. Since it is a very restricted set of terms it is possible that we added a particular choice of a term that, because of the details of the dynamics of the system, is not covering properly the unboundedness. We find that sometimes modifying this set can help find out a better solution.

   e) As the final test to perform on the model, we strongly suggest to run high temperature annealings for large supercells. Sometimes finite-size effects cover runaway directions in the configurational space, but they become easier to access as we increase the dimension of $\Omega$.

# Appendix B

# List of publications

In the following there is the list of publications produced during this Thesis:

- C. Escorihuela-Sayalero, J. C. Wojde l, and J. Íñiguez
  *Efficient systematic scheme to construct second-principles lattice dynamical models*
  Phys. Rev. B, vol. 95, p. 094115, March 2017

- J. A. Seijas-Bellido, C. Escorihuela-Sayalero, M. Royo, M. P. Ljungberg, J. C. Wojdeł, J. Íñiguez, and R. Rurali
  *A phononic switch based on ferroelectric domain walls*
  Phys. Rev. B, vol. 96, p. 140101, October 2017

- M. Royo, C. Escorihuela-Sayalero, J. Íñiguez, and R. Rurali
  *Ferroelectric domain wall phonon polarizer*
  Phys. Rev. Materials, vol. 1, p. 051402, October 2017

- Hong Jian Zhao, A. Filippetti, C. Escorihuela-Sayalero, P. Delugas, E. Canadell, L. Bellaiche, V. Fiorentini, and J. Íñiguez
  *Meta-screening and permanence of polar distortion in metallized ferroelectrics*
  Pys. Rev. B, vol. 97, p. 054107, 2018

- M. A. Pereira Gonçalves, C. Escorihuela-Sayalero, P. Garca-Fernández, J. Junquera, and J. Íñiguez
  *Theoretical guidelines to create and tune electric skyrmion bubbles*
  Science Advances, vol. 5, no. 2, 2019

- P. Torres, J. A. Seijas-Bellido, C. Escorihuela-Sayalero, J. Íñiguez, and R. Rurali
  *Theoretical investigation of lattice thermal conductivity and electrophononic effects in* $SrTiO_3$
  Phys. Rev. Materials, vol. 3, March 2019)

- C. Escorihuela-Sayalero, P. García-Fernández, J. Junquera and J. Íñiguez
  *Second-principles lattice-dynamical models of chemically-inhomogeneous crystals*
  (In preparation)

# Bibliography


1. Kittel, C. *Introduction to Solid State Physics* 8th (John Wiley & Sons, Inc., New York, 1986).
2. Haun, M. J., Furman, E., Jang, S. J., McKinstry, H. A. & Cross, L. E. Thermodynamic theory of PbTiO3. *Journal of Applied Physics* **62,** 3331–3338 (1987).
3. Wang, Z., Zhu, W., Zhao, C. & Tan, O. K. Dense PZT thick films derived from sol-gel based nanocomposite process. en. *Materials Science and Engineering: B* **99,** 56–62. ISSN: 09215107 (May 2003).
4. Okazaki, A. & Kawaminami, M. Lattice constant of strontium titanate at low temperatures. en. *Materials Research Bulletin* **8,** 545–550. ISSN: 00255408 (May 1973).
5. Ashcroft, N. & Mermin, N. *Solid State Physics* (Saunders College, Philadelphia, 1976).
6. Chen, P. *et al.* Energetics of oxygen-octahedra rotations in perovskite oxides from first principles. *Physical Review B* **97,** 024113 (2 Jan. 2018).
7. Goldschmidt, V. M. Die Gesetze der Krystallochemie. *Die Naturwissenschaften* **14,** 477–485. ISSN: 0028-1042, 1432-1904 (May 1926).
8. Zhong, W., Vanderbilt, D. & Rabe, K. M. Phase Transitions in $BaTiO_3$ from First Principles. *Physical Review Letters* **73,** 1861 (1994).
9. Bell, A. J. Factors influencing the piezoelectric behaviour of PZT and other "morphotropic phase boundary" ferroelectrics. en. *Journal of Materials Science* **41,** 13–25. ISSN: 0022-2461, 1573-4803 (Jan. 2006).
10. Damjanovic, D., Budimir, M., Davis, M. & Setter, N. Piezoelectric anisotropy: Enhanced piezoelectric response along nonpolar directions in perovskite crystals. en. *Journal of Materials Science* **41,** 65–76. ISSN: 0022-2461, 1573-4803 (Jan. 2006).
11. Oh, S. H. & Jang, H. M. Ferroelectric phase transitions and three-dimensional phase diagrams of a Pb(Zr, Ti)O3 system under a hydrostatic pressure. en. *Journal of Applied Physics* **85,** 2815–2820. ISSN: 0021-8979, 1089-7550 (Mar. 1999).
12. Noheda, B. *et al.* A monoclinic ferroelectric phase in the Pb(Zr1xTix)O3 solid solution. en. *Applied Physics Letters* **74,** 2059–2061. ISSN: 0003-6951, 1077-3118 (Apr. 1999).
13. Bellaiche, L., García, A. & Vanderbilt, D. Finite-temperature properties of Pb (Zr 1- x Ti x) O 3 alloys from first principles. *Physical Review Letters* **84,** 5427 (2000).
14. Nair, N. N., Schreiner, E. & Marx, D. Glycine at the PyriteWater Interface: The Role of Surface Defects. *Journal of the American Chemical Society* **128,** 13815–13826. ISSN: 0002-7863, 1520-5126 (Oct. 2006).
15. Kalikka, J., Akola, J., Larrucea, J. & Jones, R. O. Nucleus-driven crystallization of amorphous $Ge_2Sb_2Te_5$: A density functional study. *Physical Review B* **86,** 144113 (14 Oct. 2012).

16. Reitz, D. W. A Review of: "Continuum Scale Simulation of Engineering Materials, Fundamentals – Microstructures – Process Applications". *Materials and Manufacturing Processes* **21,** 331–331 (2006).

17. Zhong, W., King-Smith, R. D. & Vanderbilt, D. Giant LO-TO splittings in perovskite ferroelectrics. *Physical Review Letters* **72,** 3618–3621 (22 May 1994).

18. Capelle, K. A bird's-eye view of density-functional theory. *arXiv:cond-mat/0211443.* http://arxiv.org/abs/cond-mat/0211443 (2012) (Nov. 20, 2002).

19. Hohenberg, P. & Kohn, W. Inhomogeneous Electron Gas. *Physical Review* **136,** B864 (1964).

20. Aguado-Puente, P. & Junquera, J. Structural and energetic properties of domains in $PbTiO_3$ /$SrTiO_3$ superlattices from first principles. en. *Physical Review B* **85.** ISSN: 1098-0121, 1550-235X. https://link.aps.org/doi/10.1103/PhysRevB.85.184105 (2019) (May 2012).

21. Yadav, A. K. *et al.* Observation of polar vortices in oxide superlattices. en. *Nature* **530,** 198–201. ISSN: 0028-0836, 1476-4687 (Feb. 2016).

22. Kohn, W. & Sham, L. J. Self-Consistent Equations Including Exchange and Correlation Effects. *Physical Review* **140,** A1133 (1965).

23. Ghosez, P., Cockayne, E., Waghmare, U. V. & Rabe, K. M. Lattice dynamics of BaTiO 3 , PbTiO 3 , and PbZrO 3 : A comparative first-principles study. en. *Physical Review B* **60,** 836–843. ISSN: 0163-1829, 1095-3795 (July 1999).

24. Junquera, J. & Ghosez, P. Critical thickness for ferroelectricity in perovskite ultrathin films. *Nature* **422,** 506 (Apr. 3, 2003).

25. Wang, J. *et al.* Epitaxial BiFeO3 Multiferroic Thin Film Heterostructures. *Science* **299,** 1719–1722. ISSN: 0036-8075 (2003).

26. Harrison, J. A. *et al.* Review of force fields and intermolecular potentials used in atomistic computational materials research. *Applied Physics Reviews* **5,** 031104. ISSN: 1931-9401 (Sept. 2018).

27. Wojdeł, J. C., Hermet, P., Ljungberg, M. P., Ghosez, P. & Íñiguez, J. First-principles model potentials for lattice-dynamical studies: general methodology and example of application to ferroic perovskite oxides. *Journal of Physics: Condensed Matter* **25,** 305401 (2013).

28. Wojdeł, J. C. & Íñiguez, J. Ferroelectric transitions at ferroelectric domain walls found from first principles. *Physical Review Letters* **112,** 247603 (2014).

29. Seijas-Bellido, J. A. *et al.* A phononic switch based on ferroelectric domain walls. *Physical Review B* **96,** 140101 (14 Oct. 2017).

30. Royo, M., Escorihuela-Sayalero, C., Íñiguez, J. & Rurali, R. Ferroelectric domain wall phonon polarizer. *Physical Review Materials* **1,** 051402 (5 Oct. 2017).

31. Pereira Gonçalves, M. A., Escorihuela-Sayalero, C., Garca-Fernández, P., Junquera, J. & Íñiguez, J. Theoretical guidelines to create and tune electric skyrmion bubbles. *Science Advances* **5.** eprint: http://advances.sciencemag.org/content/5/2/eaau7023.full.pdf. http://advances.sciencemag.org/content/5/2/eaau7023 (2019).

32. George, A. M., Íñiguez, J. & Bellaiche, L. Anomalous properties in ferroelectrics induced by atomic ordering. *Nature* **413,** 54–57. ISSN: 0028-0836, 1476-4687 (Sept. 2001).

33. Íñiguez, J. & Bellaiche, L. Ab Initio Design of Perovskite Alloys with Predetermined Properties: The Case of Pb ( Sc 0.5 Nb 0.5 ) O 3. *Physical Review Letters* **87.** ISSN: 0031-9007, 1079-7114. https://link.aps.org/doi/10.1103/PhysRevLett.87.095503 (2019) (Aug. 9, 2001).

34. Jones, J. E. On the Determination of Molecular Fields. II. From the Equation of State of a Gas. *Proceedings of the Royal Society A: Mathematical, Physical and Engineering Sciences* **106,** 463–477. ISSN: 1364-5021, 1471-2946 (Oct. 1, 1924).

35. Zhen, S. & Davies, G. J. Calculation of the Lennard-Jones n–m potential energy parameters for metals. *Physica Status Solidi (a)* **78,** 595–605. ISSN: 00318965, 1521396X (Aug. 16, 1983).

36. Smit, B. Phase diagrams of Lennard-Jones fluids. *The Journal of Chemical Physics* **96,** 8639–8640. ISSN: 0021-9606, 1089-7690 (June 1992).

37. Van Duin, A. C. T., Dasgupta, S., Lorant, F. & Goddard, W. A. ReaxFF: A Reactive Force Field for Hydrocarbons. *The Journal of Physical Chemistry A* **105,** 9396–9409. ISSN: 1089-5639, 1520-5215 (Oct. 2001).

38. Lii, J.-H. & Allinger, N. L. Molecular Mechanics. The MM3 Force Field for Hydrocarbons. 3. The van der Waals' Potentials and Crystal Data for Aliphatic and Aromatic Hydrocarbonsf, 7 (Mar. 1989).

39. Allinger, N. L., Li, F. & Yan, L. Molecular mechanics. The MM3 force field for alkenes. *Journal of Computational Chemistry* **11,** 848–867. ISSN: 0192-8651, 1096-987X (Aug. 1990).

40. Mayo, S. L., Olafson, B. D. & Goddard, W. A. DREIDING: a generic force field for molecular simulations. *The Journal of Physical Chemistry* **94,** 8897–8909. ISSN: 0022-3654, 1541-5740 (Dec. 1990).

41. Islam, M. M., Zou, C., van Duin, A. C. T. & Raman, S. Interactions of hydrogen with the iron and iron carbide interfaces: a ReaxFF molecular dynamics study. *Physical Chemistry Chemical Physics* **18,** 761–771. ISSN: 1463-9076, 1463-9084 (2016).

42. Goddard, W. A. *The ReaxFF Polarizable Reactive Force Fields for Molecular Dynamics Simulation of Ferroelectrics* in *AIP Conference Proceedings* FUNDAMENTAL PHYSICS OF FERROELECTRICS 2002. **626** (AIP, Washington, DC (USA), 2002), 45–55. doi:10.1063/1.1499551. http://aip.scitation.org/doi/abs/10.1063/1.1499551 (2019).

43. Van Duin, A. C. T., Merinov, B. V., Han, S. S., Dorso, C. O. & Goddard, W. A. ReaxFF Reactive Force Field for the Y-Doped BaZrO $_3$ Proton Conductor with Applications to Diffusion Rates for Multigranular Systems. *The Journal of Physical Chemistry A* **112,** 11414–11422. ISSN: 1089-5639, 1520-5215 (Nov. 13, 2008).

44. Hjertenæs, E., Nguyen, A. Q. & Koch, H. A ReaxFF force field for sodium intrusion in graphitic cathodes. *Physical Chemistry Chemical Physics* **18,** 31431–31440. ISSN: 1463-9076, 1463-9084 (2016).

45. Castro-Marcano, F., Kamat, A. M., Russo, M. F., van Duin, A. C. & Mathews, J. P. Combustion of an Illinois No. 6 coal char simulated using an atomistic char representation and the ReaxFF reactive force field. *Combustion and Flame* **159,** 1272–1285. ISSN: 00102180 (Mar. 2012).

46. Zhang, W. & van Duin, A. C. T. Second-Generation ReaxFF Water Force Field: Improvements in the Description of Water Density and OH-Anion Diffusion. *The Journal of Physical Chemistry B* **121.** PMID: 28570806, 6021–6032 (2017).

47. Kleffner, R. *et al.* Foldit Standalone: a video game-derived protein structure manipulation interface using Rosetta. *Bioinformatics* **33,** 2765–2767. ISSN: 1367-4803 (May 2017).
48. Zhong, W., Vanderbilt, D. & Rabe, K. M. First-principles theory of ferroelectric phase transitions for perovskites: The case of $BaTiO_3$. *Physical Review B* **52,** 6301 (1995).
49. Marathe, M., Ederer, C. & Grünebohm, A. The Impact of Hysteresis on the Electrocaloric Effect at First-Order Phase Transitions. *physica status solidi (b)* **255,** 1700308 (2018).
50. Marathe, M. *et al.* Electrocaloric effect in BaTiO3 at all three ferroelectric transitions: Anisotropy and inverse caloric effects. *Physical Review B* **96,** 014102 (2017).
51. Gruenebohm, A., Marathe, M. & Ederer, C. Tuning the caloric response of BaTiO3 by tensile epitaxial strain. *Europhysics Letters* **115,** 47002 (2016).
52. Kornev, I. A., Lisenkov, S., Haumont, R., Dkhil, B. & Bellaiche, L. Finite-Temperature Properties of Multiferroic $BiFeO_3$. *Physical Review Letters* **99,** 227602 (22 Nov. 2007).
53. Prosandeev, S., Xu, B. & Bellaiche, L. Polarization switching in the $PbMg_{1/3}Nb_{2/3}O_3$ relaxor ferroelectric: An atomistic effective Hamiltonian study. *Physical Review B* **98,** 024105 (2 July 2018).
54. Al-Barakaty, A., Prosandeev, S., Wang, D., Dkhil, B. & Bellaiche, L. Finite-temperature properties of the relaxor $PbMg_{1/3}Nb_{2/3}O_3$ from atomistic simulations. *Physical Review B* **91,** 214117 (21 June 2015).
55. Yang, Y., Xu, B., Xu, C., Ren, W. & Bellaiche, L. Understanding and revisiting the most complex perovskite system via atomistic simulations. *Physical Review B* **97,** 174106 (17 May 2018).
56. Gonze, X. & Lee, C. Dynamical matrices, born effective charges, dielectric permittivity tensors, and interatomic force constants from density-functional perturbation theory. *Physical Review B* **55,** 10355 (1997).
57. Escorihuela-Sayalero, C., Wojdeł, J. C. & Íñiguez, J. Efficient systematic scheme to construct second-principles lattice dynamical models. *Physical Review B* **95,** 094115 (9 Mar. 2017).
58. Arlinghaus, S. L. *Practical handbook of curve fitting* (CRC Press, 1994).
59. Rockafellar, R. T. Lagrange Multipliers and Optimality. *SIAM Review* **35,** 183–238 (1993).
60. Bland, R. G. New Finite Pivoting Rules for the Simplex Method. en. *Mathematics of Operations Research* **2,** 103–107 (1977).
61. Guest, P. G. *Numerical Methods of Curve Fitting* (Cambridge University Press, 1961).
62. Sheppard, D., Xiao, P., Chemelewski, W., Johnson, D. D. & Henkelman, G. A generalized solid-state nudged elastic band method. *The Journal of Chemical Physics* **136,** 074103 (2012).
63. Xu, L. & Zhang, W. Comparison of different methods for variable selection. *Analytica Chimica Acta* **446,** 475–481 (2001).
64. Burnham, K. P. & Anderson, D. R. *Model selection and multimodel inference: a practical information-theoretic approach* (Springer Science & Business Media, 2003).
65. Vanderbilt, D. & Cohen, M. H. Monoclinic and triclinic phases in higher-order Devonshire theory. en. *Physical Review B* **63.** ISSN: 0163-1829, 1095-3795. http://link.aps.org/doi/10.1103/PhysRevB.63.094108 (2001).
66. Celisse, A. & Robin, S. Nonparametric density estimation by exact leave–out cross-validation. *Computational Statistics & Data Analysis* **52,** 2350–2368 (2008).

67. Prechelt, L. Automatic early stopping using cross validation: quantifying the criteria. *Neural Networks* **11,** 761–767 (1998).

68. Fleury, P. A., Scott, J. F. & Worlock, J. M. Soft phonon modes and the 110° K phase transition in $SrTiO_3$. *Physical Review Letters* **21,** 16–19 (1968).

69. Glazer, A. M. The classification of tilted octahedra in perovskites. *Acta Crystallographica Section B* **28,** 3384–3392 (1972).

70. Lytle, F. *Journal of Applied Physics* **35,** 2212 (1964).

71. Zhong, W. & Vanderbilt, D. Effect of quantum fluctuations on structural phase transitions in $SrTiO_3$ and $BaTiO_3$. *Physical Review B* **53,** 5047 (1996).

72. Müller, K. A. & Burkard, H. $SrTiO_3$: An intrinsic quantum paraelectric below 4 K. *Physical Review B* **19,** 3593–3602 (1979).

73. Zhong, W. & Vanderbilt, D. Competing Structural Instabilities in Cubic Perovskites. *Physical Review Letters* **74,** 2587 (1995).

74. Müller, K. A. & Burkard, H. SrTi O 3 : An intrinsic quantum paraelectric below 4 K. en. *Physical Review B* **19,** 3593–3602. ISSN: 0163-1829 (Apr. 1979).

75. Allen, P. & Tildesley, D. J. *Computer Simulation of Liquids* ISBN: 9780198556459 (Clarendon Press, 1989).

76. Parrinello, M. & Rahman, A. Polymorphic transitions in single crystals: A new molecular dynamics method. *Journal of Applied Physics* **52,** 7182 (1981).

77. Bellaiche, L., Garcıa, A. & Vanderbilt, D. Finite-Temperature Properties of $Pb(Zr_{1-x}Ti_x)O_3$ Alloys from First Principles. *Physical Review Letters* **84,** 5427 (2000).

78. Kornev, I. A., Lisenkov, S., Haumont, R., Dkhil, B. & Bellaiche, L. Finite-Temperature Properties of Multiferroic $BiFeO_3$. *Physical Review Letters* **99,** 227602–4 (2007).

79. Ghosez, P., Cockayne, E., Waghmare, U. V. & Rabe, K. M. Lattice dynamics of BaTiO3, PbTiO3, and PbZrO3: A comparative first-principles study. *Physical Review B* **60,** 836 (1999).

80. Wojdeł, J. C. & Íñiguez, J. Testing simple predictors for the temperature of a structural phase transition. *Physical Review B* **90,** 014105 (2014).

81. Abrahams, S. C., Kurtz, S. K. & Jamieson, P. B. Atomic Displacement Relationship to Curie Temperature and Spontaneous Polarization in Displacive Ferroelectrics. *Physical Review* **172,** 551 (1968).

82. Wahl, R., Vogtenhuber, D. & Kresse, G. $SrTiO_3$ and $BaTiO_3$ revisited using the projector augmented wave method: Performance of hybrid and semilocal functionals. *Physical Review B* **78,** 104116 (2008).

83. Rabe, K. M. & Ghosez, P. in *Physics of Ferroelectric: A modern perspective* 117–174 (Springer-Verlag Berlin, 2007).

84. Neaton, J. B. & Rabe, K. M. Theory of polarization enhancement in epitaxial BaTiO3/SrTiO3 superlattices. *Applied Physics Letters* **82,** 1586–1588. ISSN: 0003-6951, 1077-3118 (Mar. 10, 2003).

85. Wu, X., Stengel, M., Rabe, K. M. & Vanderbilt, D. Predicting Polarization and Nonlinear Dielectric Response of Arbitrary Perovskite Superlattice Sequences. *Physical Review Letters* **101.** ISSN: 0031-9007, 1079-7114. https://link.aps.org/doi/10.1103/PhysRevLett.101.087601 (2019) (Aug. 18, 2008).

86. Pindera, M.-J., Khatam, H., Drago, A. S. & Bansal, Y. Micromechanics of spatially uniform heterogeneous media: A critical review and emerging approaches. *Composites Part B: Engineering* **40,** 349–378. ISSN: 13598368 (July 2009).

87. Raju, B., Hiremath, S. & Roy Mahapatra, D. A review of micromechanics based models for effective elastic properties of reinforced polymer matrix composites. *Composite Structures* **204,** 607–619. ISSN: 02638223 (Nov. 2018).

88. Nahas, Y. *et al.* Discovery of stable skyrmionic state in ferroelectric nanocomposites. *Nature Communications* **6.** ISSN: 2041-1723. http://www.nature.com/articles/ncomms9542 (2019) (Dec. 2015).

89. Yamanaka, A. *et al.* Evidence for competing orderings in strontium titanate from hyper-Raman scattering spectroscopy. en. *Europhysics Letters (EPL)* **50,** 688–694. ISSN: 0295-5075, 1286-4854 (June 2000).

90. Sakudo, T. Dielectric Properties of SrTi03 at Low Temperatures. en. *Physical Review Letters* **26,** 3 (1971).

91. Uwe, H. & Sakudo, T. Stress-induced ferroelectricity and soft phonon modes in SrTi O 3. en. *Physical Review B* **13,** 271–286. ISSN: 0556-2805 (Jan. 1976).

92. Houchmandzadeh, B., Lajzerowicz, J. & Salje, E. Order parameter coupling and chirality of domain walls. *Journal of Physics: Condensed Matter* **3,** 5163 (1991).

93. Tagantsev, A. K., Courtens, E. & Arzel, L. Prediction of a low-temperature ferroelectric instability in antiphase domain boundaries of strontium titanate. *Physical Review B* **64,** 224107 (2001).

94. Schiaffino, A. & Stengel, M. Macroscopic Polarization from Antiferrodistortive Cycloids in Ferroelastic $SrTiO_3$. *Physical Review Letters* **119,** 137601 (13 Sept. 2017).

**Abstract**

The application of Condensed Matter theory via simulation has been over the last decades a solid approach to research in Materials Science. In particular for the case of Perovskite materials the research has been extensive, and customarily (but not only) performed using Density Functional Theory. The collective effort to develop lighter simulation techniques and exploring different theoretical approaches to computationally study materials has provided the scientific community with the possibility to strengthen the interaction between experimental and theoretical research. However, the access to large-scale simulations is still nowadays limited due to the high computational cost of such simulations. In 2013 J. C. Wojdeł et al. presented a theory of modelization of crystals known as second-principles models, and which are the central point of the development of my work.

In this Thesis I develop in depth a novel methodology to produce second-principles models efficiently and in a quasi-automatic way from Density Functional Theory data. The scheme presented here identifies, given a set of reliable data to be fit, the most relevant atomic couplings of a system. The fitting process that I present is also analytical, which translates into a fast and accurate model production. I also explore the modelization of chemically inhomogeneous or nanostructured systems using second-principles models. Moreover, I present a heuristic procedure to produce models of the inhomogeneous material which is efficient and sound. Finally, I also show examples of complex problems that can be tackled thanks to the second-principles models, such as the character of $180^o$ anti-phase domain walls in $SrTiO_3$, thermodynamical studies of heat transport accross $180^o$ domain walls in $PbTiO_3$ and the reproduction of experimentally-observed polarization vortices in $(PbTiO_3)_n/(SrTiO_3)_n$ superlattices.